Numerical simulations of blood flow in the left side of the heart

Sigrid Kaarstad Dahl

Norwegian University of Science and Technology
Faculty of Engineering Science and Technology
Department of Structural Engineering
Trondheim, Norway

Preface

This doctoral thesis is submitted to the Norwegian University of Science and Technology (NTNU) for the degree Philosophiae Doctor. The work has been carried out at the Department of Structural Engineering, NTNU. My supervisors have been Professor Bjørn Skallerud and Professor Leif Rune Hellevik (Department of Structural Engineering, NTNU), Professor Jan Vierendeels (Department of Flow, Heat and Combustion Mechanics, Ghent University, Belgium) and Kent-Andre Mardal (Simula Research Laboratory, Oslo). The work has been supported by Simula School of Research and Innovation AS.

Acknowledgements

There are many people I would like to thank and that should be acknowledged for their contribution during my project work.

I would like to express my gratitude to my supervisors Professor Bjørn Skallerud and Professor Leif Rune Hellevik at the Department of structural Engineering for their motivation, support and constructive comments. They have been supportive of my ideas and given me appreciated freedom during my work. I am greatful to Bjørn Skallerud who initially introduced me to the interesting field of cardiac blood flow. I also wish to thank Professor Tor Ytrehus at the Fluid dynamics group, NTNU, for interesting and valuable discussions on fluid dynamics.

I would like to thank my co-supervisor Professor Jan Vierendeels at the University of Ghent in Belgium, for showing great interest in my work, for valuable comments and for patiently supervising me through the field of fluid structure interaction. I also want to thank Professor Patrick Segers and all the colleguas at the University of Ghent for their great hospitality and for giving me a good time when I was visiting Ghent and when we met at conferences and seminars.

This project would not have been possible without all the support at MIlab (NTNU) / St. Olavs University Hospital. Thank you for performing an endless number of ultrasound and magnetic resonance (MR) acquisitions of my heart, for giving me access to the necessary post-processing software and for being available with support whenever I needed. I am grateful to Professor Hans Torp and PhD Lasse Løvstakken for supporting me when I first came to their office as a masterstudent to ask for ultrasound recordings for my project. A special thanks goes to MD, PhD Brage Amundsen for all the help with MRI and 3D ultrasound acquisitions in the last part of my thesis. I am sorry for falling asleep in the MR machine over and over again. I would also express my gratitude to PhD Gabriel Kiss, for always answering my questions conserning medical imaging and for valuable comments on my manuscripts even when I did not ask for it. He was available with his support at any time.

A great motivation during my PhD has been the interest shown by MD, PhD Kjell Arne Rein and MD, PhD Stig Urheim at Rikshospitalet. Thanks for fruitful discussions about the anatomy, physiology and pathology of the left heart and for seeing clinical potential in my simulation models. A special thanks to Kjell Arne Rein who invited me to Rikshospitalet twice and invited several of his collegues to our meetings. He even let me attend a heart surgery, it was extremely interesting, but I will never forget the smell.

I would also like to thank the administration and the IT division at the Department of structural Engineering and at Simula Research Laboratory for their valuable help in technical, secretarial and administrative work. It has been appreciated.

Thanks to my collegues and friends at the Department of structural Engineering for all the nice distractions from work and for creating a friendly enviroment. Last, but not least, thanks to my friends and family for all the support and caring. You have all helped me staying sane (apperently) all these years.

Contents

I Introductory section **1**

1 Introduction **3**
1.1 Motivation . . . 3
1.2 Aims and scope . . . 4

2 Anatomy and physiology of the heart **7**
2.1 Cardiac cycle . . . 9
2.2 The mitral apparatus . . . 14
2.2.1 The mitral annulus . . . 14
2.2.2 The mitral valve leaflets . . . 14
2.2.3 The subvalvular apparatus . . . 15
2.3 Blood flow . . . 15

3 Numerical simulations of cardiac blood flow **17**
3.1 CFD approaches . . . 17
3.1.1 Deforming fluid domain . . . 18
3.2 Modeling the heart chambers . . . 20
3.2.1 Time-varying geometry . . . 20
3.2.2 Subject-specific models based on medical imaging . . . 20
3.2.3 The left ventricle . . . 21
3.2.4 The left atrium . . . 21
3.2.5 Uncertainties . . . 22
3.3 Modeling the mitral valve . . . 22

4 Summary of appended papers **25**
4.1 Declaration of authorship . . . 27
4.2 Publication list . . . 28

5 Conclusions and further work **31**
5.1 Conclusions . . . 31
5.1.1 General remarks . . . 33
5.2 Directions for further work . . . 33

II Research papers **37**

6 FSI-simulation of asymmetric mitral valve dynamics during diastolic filling **39**
6.1 Introduction . . . 40
6.2 Models and methods . . . 41
6.2.1 Geometrical model . . . 41
6.2.2 Numerical method . . . 42
6.2.3 Boundary and initial conditions . . . 42
6.2.4 Fluid structure interaction method . . . 42
6.3 Results . . . 46
6.4 Discussion . . . 49

7 An assessment of left atrial boundary conditions and the effect of mitral leaflets on left ventricular filling **53**
7.1 Introduction . . . 54
7.2 Models and methods . . . 55
7.2.1 Geometrical model . . . 55
7.2.2 Fluid structure interaction method . . . 56
7.2.3 Boundary and initial conditions . . . 57
7.3 Results . . . 57
7.3.1 c_I versus c_{II} . . . 57
7.3.2 c_{II} versus c_{III} . . . 59
7.4 Discussion . . . 60
7.4.1 Sensitivity to inlet geometry . . . 60
7.4.2 The leaflets' influence on the intraventricular flow . . . 62
7.4.3 Conclusions . . . 63

8 Impact of pulmonary venous locations on the intra-atrial flow and mitral plane velocity profile **65**
8.1 Introduction . . . 66
8.2 Method . . . 67
8.2.1 Magnetic Resonance Imaging and flux measurements . . . 67
8.2.2 Segmentation and geometrical reconstruction . . . 67
8.2.3 Numerical method . . . 68
8.2.4 Boundary conditions . . . 68
8.3 Results . . . 69
8.3.1 Normal intra-atrial flow pattern . . . 69
8.3.2 Sensitivity to PV location . . . 72
8.3.3 Cross-sectional velocity profile at the mitral plane . . . 74
8.4 Discussion . . . 74
8.4.1 Intra-atrial flow . . . 74
8.4.2 Mitral velocity distribution . . . 76
8.4.3 Limitations . . . 77
8.4.4 Conclusions . . . 77

9 3D moving boundary conditions for heart CFD simulations - from echocardiographic recordings to discretized surfaces 79
9.1 Introduction . . . 80
9.2 Method . . . 81
9.2.1 3D echocardiography and segmentation of the LV . . . 81
9.2.2 3D finite element model of the mitral valve . . . 81
9.2.3 Geometrical reconstruction . . . 82
9.2.4 Mitral valve position optimisation . . . 82
9.2.5 Construction of the left ventricular outflow tract (LVOT) and the ascending aorta (Aao) . . . 83
9.2.6 Prescribed LV movement . . . 84
9.2.7 Creation of intermediate computational meshes . . . 90
9.3 Results . . . 90
9.4 Discussion . . . 91
9.4.1 Limitations . . . 93
9.5 Conclusions . . . 93

A Impact of the mitral leaflets' curvature on flow dynamics during left ventricular contraction: An initial study 95
A.1 Background of the study . . . 96
A.2 2D study . . . 97
A.2.1 Models and method . . . 97
A.2.2 Results and discussion . . . 99
A.3 3D study . . . 100
A.3.1 The 3D model . . . 100
A.3.2 Modification of the FE MV model . . . 100
A.3.3 Numerical model . . . 103
A.3.4 Preliminary results and discussion . . . 104
A.3.5 In-vivo validation . . . 106
A.3.6 Limitations . . . 107
A.4 Concluding remarks . . . 107
A.5 Further work . . . 108

Part I

Introductory section

Chapter 1

Introduction

This thesis consists of two parts and one appendix. Part one is the introductory section and is organized in five chapters. The purpose of the introduction is to give a brief description of the background for the performed studies. The first chapter presents the motivation and the aims of the project. The second one gives an overview of the anatomy and the physiology of the heart. Chapter three gives a brief introduction to computational cardiac modeling, and in chapter four a summary of the papers and a publication list is presented. The introductory section is closed in chapter five with concluding remarks and directions for further studies. Part two, chapter six to nine, is a collection of research papers. Each paper is self-contained with its own introduction and conclusion and some of the information is therefore repeated.

1.1 Motivation

"Biomechanics is the study of the structure and function of biological systems by means of the methods of mechanics" Hatze [47]

Cardiovascular disease (CVD) is today the leading cause of death in the western world, with an incidence rate expected to increase following a trend of obesity in the population [111]. There is therefore an increasing need for accurate and efficient tools for cardiovascular diagnostics.

Non-invasive medical imaging of the cardiovascular system can be used to detect and grade pathology related to both anatomical and physiological abnormalities. A particular advantage of such techniques is the ability to measure the movement of blood and tissue, used for instance to investigate blood flow patterns inside the heart. To quantify in more detail the observed native or pathological flow patterns and their influence on the myocardium, it is beneficial to have analytical and computational models which allow for fundamental insight. In the field of biomechanics, tools exist for performing computer simulations of complex transient geometries. Coupling computational fluid dynamics (CFD) with medical imaging enables the opportunity to reconstruct subject-specific simulation models of the pumping heart. Such models can help us to understand the complex flow phenomenon and provide us with flow details on a level not possible by medical imaging alone.

A simulation environment offers flexible control of the boundary conditions (mimicking healthy and diseased myocardial tissue or vessel wall) and flow parameters (corresponding to changed hemodynamic loads). This gives the opportunity to easily alter the models and further check how the flow

responds to the applied changes. A future goal is to create subject-specific models that may have the potential to support professionals in clinical decision-making by performing virtual surgery. By doing this, new insight into the influence of surgical intervention on the blood flow can be obtained. However, before a model can be used for clinical purposes, thoroughly validation is necessary.

Different approaches have been suggested in order to create numerical simulations of the blood flow in the heart, where the main focus has been on the flow in the left ventricle (LV). All studies have various shortcomings and none of the models are yet applicable on a clinical base.

1.2 Aims and scope

The main goal of this thesis has been to enhance the understanding of cardiac blood flow, by means of the development and assessment of various approaches for subject-specific simulation of cardiac hemodynamics. The focus has been on the blood flow in the left side of the heart, which includes the left ventricle, the left atrium (LA), the mitral valve (MV) and the aortic valve (AoV).

The main research topics of this thesis may be summarized as follows:

- **Subject-specific models**
  Our aim was to use models and methods that could contribute to a better understanding of the hemodynamics in the heart. To obtain physiological realism in our models and to sooner get into clinical research, we wanted to use subject-specific models. A geometry-prescribed CFD approach was therefore chosen for the heart chambers in this thesis. To achieve subject-specific boundary conditions, the geometries were obtained from medical imaging data. Cardiovascular medical imaging, in particular ultrasound, magnetic resonance imaging (MRI) and computed tomography (CT) have reached a level that provides high quality geometrical data. Today, ultrasound is the major imaging tool in cardiology. A major benefit of ultrasound is that it allows for real-time inter-active display of image data and can therefore help in guiding treatment. The main objective was to build models based on ultrasound for both 2D and 3D flow simulations. However, other imaging modalities were used if necessary.

- **A fluid structure interaction (FSI) algorithm for two asynchronously moving, rigid leaflets**
  The mitral valve has a complex three-dimensional geometry and movement pattern. The two mitral leaflets are thin, rapidly moving structures which undergo large deformations during a heart cycle. The modeling of the mitral valve is therefore a challenging task and currently, no single method solves this task completely. Due to the complexity, the mitral leaflets are often excluded in simulations of ventricular flow. We wanted to study how the mitral leaflets affect the intraventricular flow field during diastole. We also wanted to avoid using symmetry in our simulations. One of the research objectives was therefore to develop an FSI algorithm which could handle two asynchronously moving, rigid leaflets. The leaflets' impact on the flow field was then analyzed in a 2D simulation of ventricular filling, where the anterior and posterior valve lengths were based on ultrasound recordings.

- **The influence of left atrial boundary conditions on the velocity profile at the mitral orifice and on the intraventricular flow pattern**
  Due to the complexity of the heart, the left atrium is often neglected in simulations of LV filling. The LA is then replaced by some simplified inlet condition, like a uniform pressure condition

or some symmetric velocity profile. Relatively few studies have focused on the normal flow distribution inside the LA and the understanding of the global flow pattern within the atrium is therefore sparse. We wanted to investigate the flow inside the atrium and the resulting velocity distribution at the mitral orifice. Both 2D and 3D simulations were performed for this purpose. The aim was to gain knowledge of inlet conditions for LV filling simulations.

- **Subject-specific 3D boundary conditions for the pumping left ventricle**
  Subject-specific CFD models generated from medical imaging data can be used to investigate healthy and pathological cardiac blood flow and to simulate the effect of virtual surgery and thereby optimize treatment.

  One of the research objectives was to develop a method for easily creating subject-specific 3D boundary conditions for simulations of ventricular blood flow. Our aim was to build models based on ultrasound. When a surface-tracking method of the heart chambers from 3D echocardiographic data became available in 2009, we wanted to develop the first subject-specific 3D CFD model based on real-time 3D echocardiography (RT3DE).

  We also wanted to have a physiologically representation of the mitral valve in this 3D CFD model. However, it is difficult to obtain the 3D valve dynamics from echocardiographic recordings. One of the research objectives was therefore to find a strategy for how the mitral valve could be represented in the 3D CFD model.

  A future goal is to have a methodology for constructing 3D CFD models from RT3DE incorporated into ultrasound scanner systems. Such real-time CFD simulations have the potential to improve and change clinical practice.

Chapter 2

Anatomy and physiology of the heart

Anatomy is the science concerned with the form and structure of living organisms. Physiology is closely related and pertains to the function of the structures. Most biological systems are very different from normal engineering systems in the sense that they are extremely complex. This means that simplifications are often necessary in biomechanical simulations, but in order to apply simplifications that still provide meaningful results, an understanding of the actual problem is required.

Myth has it that the heart is the seat of the emotions, but in fact, the heart is a muscular, hollow organ, responsible for pumping blood throughout the body. An overview of the heart and its main components are shown in Fig. 2.1.

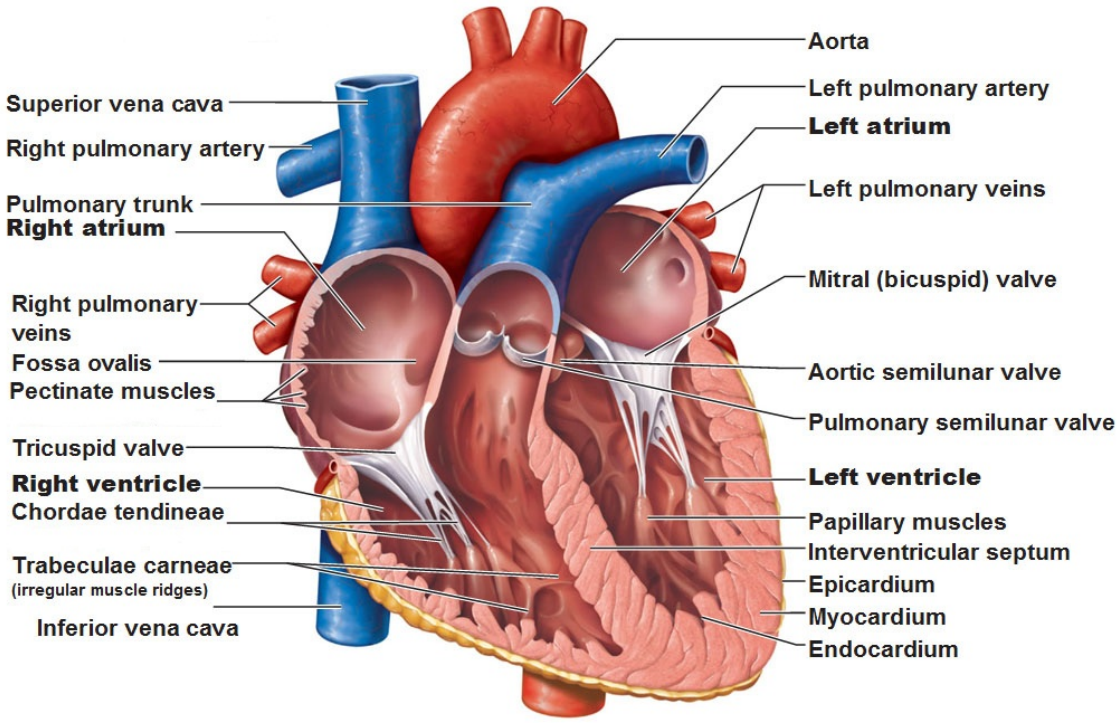

Figure 2.1: A longitudinal view of the heart and its main components [2].

A partition septum divides the heart into two halves often referred to as the right and left heart. Each half consists of two chambers; a thin-walled atrium and a thick-walled ventricle. The atria receive blood from the veins, while the ventricles pump the blood out of the heart and through the circulatory system. To maintain the unidirectional flow of blood, the heart has four valves. The valves between the atria and the ventricles are called atrioventricular valves. The right atrioventricular valve is the tricuspid valve, while the left atrioventricular valve is the bicuspid, or mitral valve. The last two valves are the semilunar valves, they are located at the base of the arteries who leave the ventricles. These are the pulmonary valve which lies between the pulmonary artery and the right ventricle (RV) and the aortic valve which is situated between the aorta and the left ventricle.

The magnetic resonance (MR) image in Fig. 2.2 shows a slice through all the four heart chambers during ventricular filling. The subject is lying on the back and the MR image is seen from the feet which mean that the right side in the picture is the subjects left side. As seen in Fig. 2.2, the heart is situated in the chest cavity in between the two lungs and behind and slightly left of the sternum (breastbone). The narrow end of the heart is called the apex whereas the broad end is called the base. The apex is pointing downwards and to the left, whereas the base is directed upwards and to the right. The left ventricle, the right ventricle, the left atrium and the right atrium (RA) are indicated in the MR image.

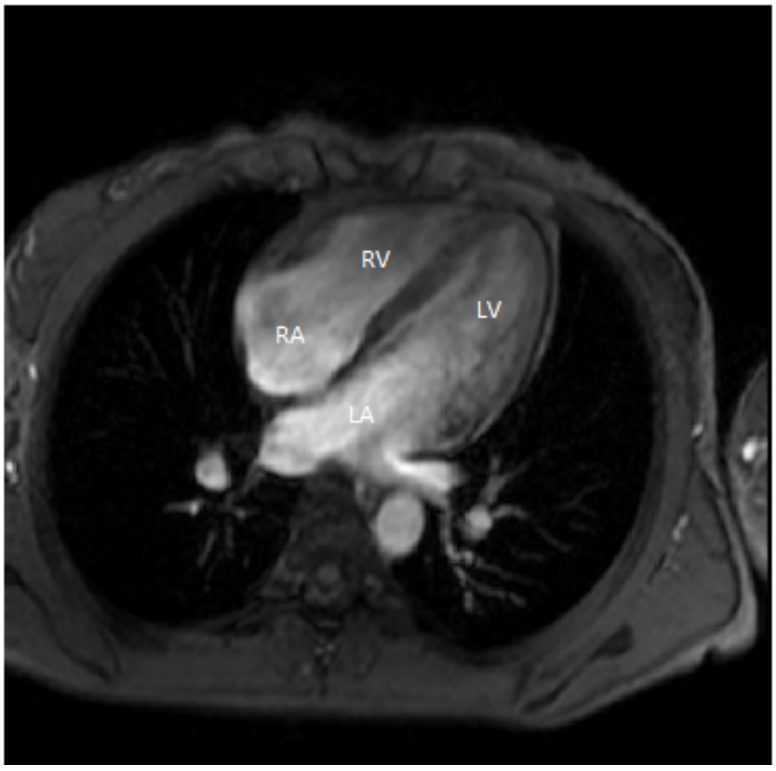

Figure 2.2: A MR image showing how the heart is positioned in a human. The image shows a slice through all the four heart chambers during ventricular filling. The image is seen from the feet so the right side in the picture is the subjects left side. The MR acquisitions were performed at St.Olavs University Hospital, Trondheim, October 2010.

The focus in this thesis will be on the left side of the heart which refers to the LV, the LA, the MV and the AoV. Fig. 2.3 shows an ultrasound image of the left heart recorded in the apical long-axis view

during ventricular filling. The ultrasound probe is then positioned directly above the apex pointing towards the subject's right shoulder. The apical long-axis view allows visualization of the LV, the LA, the MV and the AoV as indicated in the recorded image (Fig. 2.3). The AoV is here closed, whereas the MV has started to drift back towards its closed position after the first rapid filling.

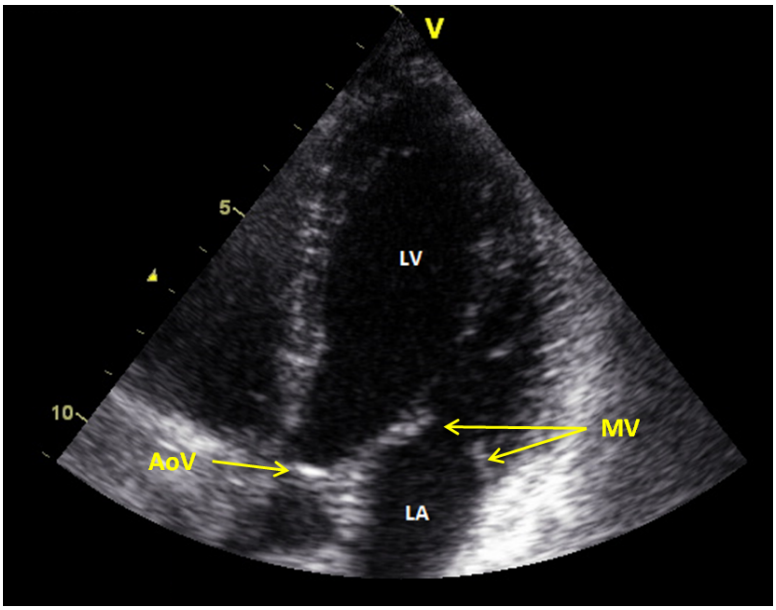

Figure 2.3: An ultrasound image of the left heart recorded in the apical long-axis view during ventricular filling. The AoV is closed, whereas the MV has started to drift back towards its closed position after the first rapid filling. The ultrasound acquisitions were performed at St.Olavs University Hospital, Trondheim, May 2006.

2.1 Cardiac cycle

The heart is, as mentioned, responsible for pumping blood through the circulatory system. The system is split into two separate circuits, called the systemic and the pulmonary circuit. The heart can be seen as a double pump, where the right side of the heart pumps deoxygenated blood into the pulmonary circulation and the left heart pumps oxygenated blood through the systemic circulation.

In the pulmonary circle, deoxygenated blood enters the right atrium from the venae cavae, from here it flows into the right ventricle which contracts and forces the blood through the pulmonary arteries and into the lungs. In the lungs the blood gets oxygenated before it returns to the left atrium via the pulmonary veins (PVs). The blood has now entered the systemic cycle. The left atrium guides the blood into the left ventricle which is the most powerful chamber. The ventricle ejects the blood into the aorta, which then distributes the blood throughout the body via a network of blood vessels, before the venae cavae bring the blood back into the right atrium where the process restarts.

The sequence of events that occur in the heart during one heart beat is called the cardiac cycle. The events occur nearly simultaneously for the right and left heart. The typical resting heart rate in adults is 60 - 90 beats per minute (bpm). A physically fit person has a lower heart rate as compared to an inactive person.

Each heart beat is commonly divided into two main phases: systole and diastole. Systole and diastole are synonymous with the contraction and relaxation of a heart muscle, respectively. Both the atria and the ventricles go through these two stages every heart beat, but when we refer to the terms diastole and systole alone, we often mean the ventricular ones. Fig. 2.4, illustrates the correspondence between the relaxation and the contraction of the chambers with respect to the ventricular phases. Fig. 2.5, illustrates how the blood travels through the heart during ventricular diastole and systole.

	Ventricular systole	Ventricular diastole	
Ventricles	Contract	Relax	
Atria	Relax	Relax	Contract

Figure 2.4: The figure illustrates the correspondence between the relaxation and the contraction of the atria and the ventricles with respect to the ventricular diastole and systole.

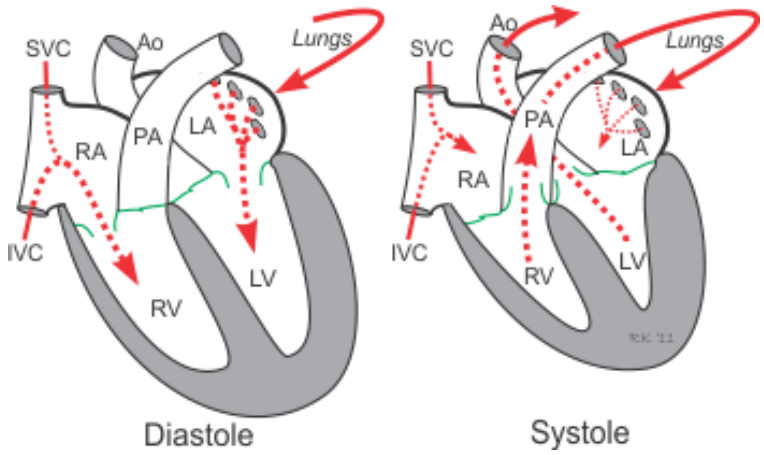

Figure 2.5: The two figures illustrate how the blood travels through the heart during ventricular diastole and systole [59].

To analyze the events in more detail, the cardiac cycle can be divided into several stages. From a ventricular view, seven phases can be considered:

- Phase 1: Atrial contraction
- Phase 2: Isovolumetric contraction
- Phase 3-4: Rapid and reduced ejection
- Phase 5: Isovolumetric relaxation
- Phase 6-7: Rapid and reduced filling

The timing of the events can be seen in Fig. 2.6. The diagram show the pressure variations in the LA, the LV and the aorta, the LV volume change and the aortic outflow rate throughout one cardiac cycle. The opening and closing events of the valves are indicated with a star. A typical electrocardiogram (ECG) tracing is shown at the bottom. The cycle in Fig.2.6 lasts for 800 ms, which corresponds to a heart rate of 75 bpm. As seen in the diagram, the cardiac cycle is defined to begin at the onset of atrial contraction, namely phase 1. In the following, the seven phases will be explained for the left heart. However, the same events occur in the right heart where an equal amount of blood has to be ejected, the main difference is that the pressure is significantly higher in the left heart.

- **Phase 1:** This is defined as the first phase of the cardiac cycle and is initiated by the P wave of the ECG. It is the last part of the ventricular diastole; all chambers are relaxed and the LV are partially filled with blood. There is hardly any transmitral flow at this stage because the pressure in the LA and LV are almost equal. As the atria contract, the intra-atrial pressure increases (also known as the a atrial pressure wave), causing an additional rapid flow of blood into the LV. This is called the second filling wave or the A-wave. The pressure in the LA exceeds the pressure in the veins, but only small amounts of back flow into the veins occur. Atrial systole lasts for approximately 100 ms. For a person at rest, atrial contraction may contribute to about 10% of ventricular filling, while for a person at higher heart rates, this extra filling may account for up to 40% of left ventricular filling [59]. The volume of blood inside the LV at the end of phase 1 is called the end-diastolic volume (EDV).

- **Phase 2:** : This is the first stage of ventricular systole. The ventricle starts to contract causing the intraventricular pressure to rise rapidly. As the intraventricular pressure exceeds the atrial pressure, the mitral valve closes immediately. The ventricle is now a closed chamber. For a short time, the pressure continues to rise rapidly while all valves are closed. During this phase there is no volume change and the contraction is, therefore, said to be isovolumetric. The rapid increase in LV pressure causes a subsequent bulging of the mitral valve into the LA, this can be observed as a small peak in the atrial pressure called the c atrial pressure wave.

- **Phase 3:** Once the ventricular pressure exceeds the pressure in the aorta, the aortic valve opens and a rapid ejection of blood into the aorta starts. The ventricular muscles begin to shorten and the ventricular volume decreases. As seen in Fig.2.6, the pressure gradient between the aorta and the LV is quite small. This is possible because of the relatively large aortic opening (i.e., low resistance). As a result of LV contraction and shortening, the mitral ring descends and the LA expands slightly, thus a fall in LA pressure occurs. Venous blood continues to flow into the LA from the veins and the atrial pressure begins once again to rise.

- **Phase 4:** A decline in ventricular active tension causes relaxation of the muscles and reduced LV pressure. The period of reduced ejection has now started. The LV pressure decreases gradually and falls slightly below the aortic pressure, which is also decreasing. However, the blood continues to flow out of the LV due to inertial effects. At the very end of systole, the LV pressure falls even faster and the blood begins to flow back towards the LV. The blood flows into the cusps of the aortic valve which close abruptly. The passive filling of the atrial chamber continues during this period and to the end of phase 5.

  The amount of blood remaining in the LV when the aortic valve closes is defined as the end-systolic volume (ESV). The total volume of blood ejected during systole is called the stroke

volume (SV) and is defined as: $SV = EDV - ESV$. In a normal resting heart, the total ventricular systole, phase 2-4, lasts approximately 270 ms having a SV around 70-80 ml [82].

- **Phase 5:** After the aortic valve closes, the ventricle continues to relax and the pressure decreases further. The LV volume remains constant because all valves are closed. This is the period of isovolumetric relaxation and the very beginning of ventricular diastole. The atrial pressure is now at its maximum after a slow pressure build up during phase 3 to 5. This is the peak of the v atrial pressure wave.

- **Phase 6:** When the LV pressure drops to below the pressure in the LA, the mitral valve opens rapidly. The blood accumulated in the atrium during systole will now flow into the LV. This is called the first rapid filling or the E-wave. Both the ventricular and the atrial pressure continue to fall in this period, the atrial one because it is emptying into the LV and the ventricular one because it still undergoes relaxation. The ongoing LV relaxation creates an additional suction which draws even more blood from the LA. The LA volume decreases, while the LV is expanding.

- **Phase 7:** As the LV continues to fill and expand it becomes less compliant and the LV pressure starts to increase again. This reduces the pressure gradient between the two chambers and the filling slows. The LV is now in the reduced filling phase or diastasis. During this period the PVs refill the LA and restore a positive atrioventricular pressure gradient.

  The diastolic period continues through atrial systole (phase 1) in the next heart beat. The total ventricular diastole, phase 5-7 and phase 1, lasts for about 430 ms in a resting heart at 75 bpm.

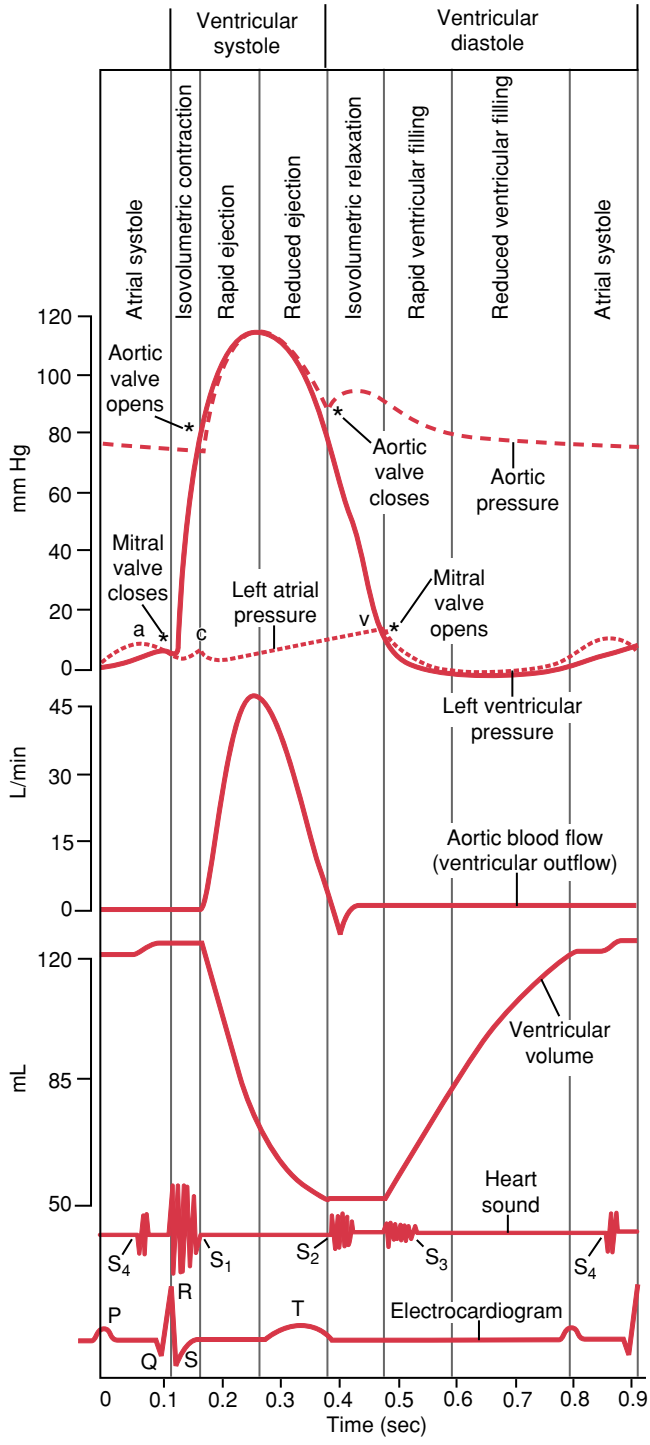

Figure 2.6: The diagram shows the timing of different events occurring in the left heart during one cardiac cycle [90]

2.2 The mitral apparatus

The mitral valve, also called the bicuspid valve, requires all its components in order to work properly. The components are the mitral annulus, the two mitral valve leaflets, the papillary muscles (PMs) and the chordae tendineae (abbreviated chordae), together they are called the mitral apparatus. The PMs and the chordae are also known as the subvalvular apparatus. The different components are indicated in Fig 2.7.

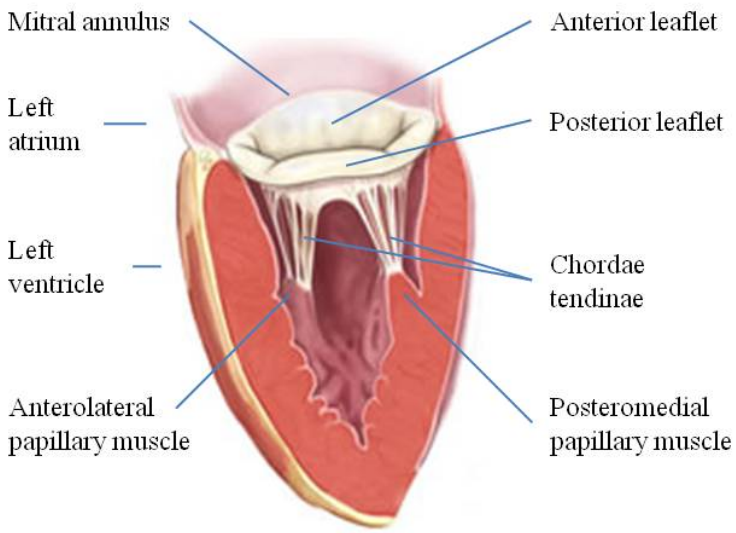

Figure 2.7: The structure of the mitral apparatus. Modified from Carpentier *et al.* [19].

2.2.1 The mitral annulus

The mitral annulus is a ring of fibrous tissue, which surrounds and supports the mitral orifice and anchors the two leaflets. The normal mitral valve orifice area in vivo ranges from 5.0 to 11.4 cm^2 (mean 7.6 ± 1.9 cm^2) [89]. The shape of the annulus approximates a hyperbolic paraboloid, often described as a three-dimensional saddle. Studies indicate that the saddle shape of the annulus might play an important role in optimizing chordal force distribution [52] and reducing leaflet stress [95].

2.2.2 The mitral valve leaflets

The mitral valve consists of two leaflets; the anterior and the posterior leaflet. Their size and circumferential length are quite different. The anterior leaflet is adjacent to the aortic artery and occupies one third of the annular circumference, whereas the posterior leaflet occupies the rest.

The anterior leaflet is largest and the leaflet is actually big enough to cover the mitral orifice alone. The posterior leaflet has a more supporting role and its movement is more restrained by the tendinous cords. During ventricular filling the soft leaflets comply and fold into the ventricle, allowing blood to pass freely. During valve closure the leaflets will fold towards each other, forming a seal. This seal is called the coaptation zone. When the coaptation height is more than 7 mm, measured from the tip to the point where the coaptation ends, the valve is usually competent and there will be no regurgitation [86].

2.2.3 The subvalvular apparatus

The subvalvular apparatus lies completely in the LV and is made up by the papillary muscles and the chordae tendineae (see Fig 2.7).

There are two papillary muscles in the left ventricle; the anterolateral one and the posteromedial one. The PMs are cone-shaped muscles extending upward from the ventricular free wall and into the LV cavity. The chordae tendineae are string-like fibrous structures which terminate from the tip of the PMs and insert into the ventricular surface of the mitral leaflets. Both of the PMs have chordae attachments to both of the leaflets. The chordae divide into branches. There are between 15 and 32 major chordal trunks arising from the PMs [62], on the other end, approximately 100 individual cords are attached to the two leaflets.

The main function of the subvalvular apparatus is to prevent the valve leaflets from being everted into the atrium when the ventricle contracts. During systole, the PMs contract to tighten the chordae tendineae. The forces exerted by the leaflets on the cords are then transferred to the PMs, hence they have an essential role in load bearing of the mitral valve during LV contraction. The distance between the PMs tips and the mitral annulus is approximately constant during systole [97]. During diastole, the PMs elongate to allow coaptation between the valve leaflets.

2.3 Blood flow

The earliest attempts to study blood flow were probably made by Young and Poiseuille in the 17th century. From an engineering perspective, blood is a very complex, but interesting fluid. Many attempts have been made in order to develop a general constitutive equation for blood. However, a theoretical reliable model which covers all relevant regimes of physiological blood flow still not exist. The study of the movements of blood and of the forces concerned is often referred to as hemodynamics.

Blood is a multipart medium consisting of cells and cell fragments suspended in a liquid. The liquid is called plasma and makes up about 55% of the total blood volume. Plasma is composed of 91.5% water, 7% proteins and 1.5% other solutes [102]. The remaining 45% of the blood volume consists of different blood cells, also called hematocytes. The three main kinds of hematocytes are the red blood cells (RBCs), the white blood cells (WBCs) and cell fragments called platelets. Under physiological conditions the WBCs and the platelets occupy only 1/600th and 1/800th of the total cell volume, respectively [83], i.e. the RBCs accounts for the major part of the cellular blood volume. The volume fraction of RBCs in whole blood is called the hematocrit level.

Plasma alone behaves like a Newtonian fluid with a dynamic viscosity[1] of $1.2 \cdot 10^{-3}\ kg/(m \cdot s)$ at $37\,^{\circ}\mathrm{C}$ [58]. However, due to the high cellular content, the whole blood behaves like a non-Newtonian fluid. The cardiovascular system is a network of vessels with geometries varying from the smallest vessels in the capillary network to the large heart chambers. It is therefore useful to characterize hemodynamic properties in terms of the environment in which the blood flows. In the smallest vessels the inner diameter is about the same size as the RBCs, ranging from 4 to $8\mu m$ [83]. When blood flows through these vessels, the RBCs have to be squeezed and deformed and move in single file [41]. The blood can then be characterized as highly non-Newtonian. However, in the largest arteries and in the heart chambers, the non-Newtonian effects are weak because of the large dimensions. The blood

[1] Dynamic viscosity is a property that characterizes the frictional resistance of a fluid to flow

can then be considered as a homogeneous fluid with Newtonian properties i.e. a constant coefficient of viscosity. The dynamic viscosity of blood in large vessels at normal physiological conditions is $3.5 \cdot 10^{-3}\ kg/(m \cdot s)$ [58].

Another common assumption is that blood is an incompressible fluid. The assumption of incompressibility comes from the fact that the density is unaffected by the pressure in the range of pressure concerned in physiology. The density is assumed to be in the range 1050-1060 kg/m^3 [105].

Blood is modeled as an incompressible, Newtonian fluid throughout this thesis.

Chapter 3

Numerical simulations of cardiac blood flow

Biomechanical problems are most often multidisciplinary and can involve elements from several domains like fluid mechanics, structural mechanics, electromechanics, scientific computing, mathematical modeling etc. Computational cardiac modeling and simulation are no exception. The heart is a highly complex organ where the flow, structural and electrical phenomena are tightly coupled. Electrical signals trigger mechanical activation, the heart walls contract and blood is ejected out in the body. However, this is not a one-way system, the blood flow influences the vessel wall mechanics and the deformation of the tissue again influences the electrical properties. A fully integrated model is the most promising tool for solving the overall heart function. However, a fully coupled physiological model of the heart which is clinically feasible still not exist. With the aim of getting into clinical research in a shorter time, separate approaches are currently more common. In this thesis the focus is on the hemodynamics in the left side of the heart. Electromechanics and material models of the myocardium and the heart valves are therefore not considered.

The numerical techniques used for solving problems involving fluid flows are often referred to as computational fluid dynamics or CFD. Different approaches have been suggested in order to create CFD models of cardiac blood flow. All studies have various shortcomings and none of the models are yet applicable on a clinical basis. In this chapter, some aspects of cardiac CFD simulations will be presented and briefly discussed. A short overview of the choices made for the CFD models in this thesis is provided in the last part of the chapter.

3.1 CFD approaches

The numerical simulations of cardiac blood flow can roughly be classified into two main groups as illustrated in Fig. 3.1. First, fluid structure interaction or FSI models, which take into account the interaction between the fluid flow and the surrounding tissue. Second, geometry-prescribed CFD models, which use prescribed wall movements as a boundary condition for the CFD simulation. The two methods cannot be considered as alternatives to each other, but approaches in their own right [98].

In a FSI simulation, the fluid flow exerts forces on the surrounding structure, the structure will then deform and in turn, affect the fluid flow. Hence, a FSI problem consists of a structural problem and a flow problem coupled together. The FSI problems can be solved using a monolithic or a partitioned approach. In the monolithic approach the structural equations and the flow equations are solved

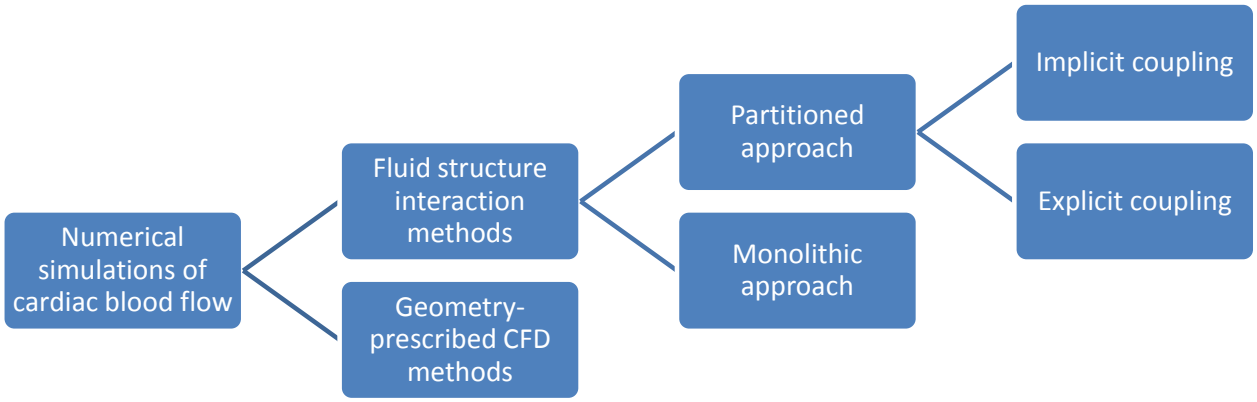

Figure 3.1: The numerical simulations of cardiac blood flow can roughly be classified into two main groups as illustrated in the flowchart. The flowchart also gives an overview over the main techniques used to solve the FSI problems. A brief description of the techniques illustrated in the flowchart is provided in the text.

simultaneously using a single code. In the partitioned approach the structural equations and the flow equations are solved within separate codes. The separate codes might be in-house codes or existing commercial solvers as long as they are treated as black boxes [30]. The partitioned approach requires a coupling algorithm which can couple the fluid and the structural systems in a stable way and assure convergence within a reasonable amount of time.

As illustrated in Fig. 3.1, the partitioned approach can be further categorized as implicit or explicit coupling [29]. In the implicit (also known as strongly coupled) partitioned techniques, iterations are performed within each time step until equilibrium between the fluid and the structure is achieved. In the explicit (also referred to as weakly or loosely coupled) partitioned techniques, the flow equations and the structural equations are solved only once or a fixed number of times within each time step. The lack of coupling iterations within each time step reduces the computational cost, but equilibrium is not necessarily achieved and the coupling scheme might become unstable. The explicit technique is therefore only sufficient when the interaction between solid and fluid is weak. If the interaction is strong, an implicit coupling technique is needed. The interaction is strong if for example the density ratio of fluid and structure is high, the fluid is incompressible or the structure is very flexible.

In a geometry-prescribed CFD simulation the boundary motion is known *a priori*. The geometry-prescribed CFD method is therefore a one-way approach which does not consider the interaction with the structure. This simplifies the modeling because there is no need for a material model or a numerical scheme capable of simulating the coupled system. However, a deforming geometry and a CFD solver capable of handling the large deformations of the fluid domain is necessary.

3.1.1 Deforming fluid domain

Traditionally, CFD simulations have been performed in domains which do not deform. In biomechanical problems, this is often not the case. There exist several techniques for calculating the flow equations in a deforming fluid domain. The techniques might be divided into two main categories. These are the fixed grid methods and the moving grid methods as illustrated in Fig. 3.2.

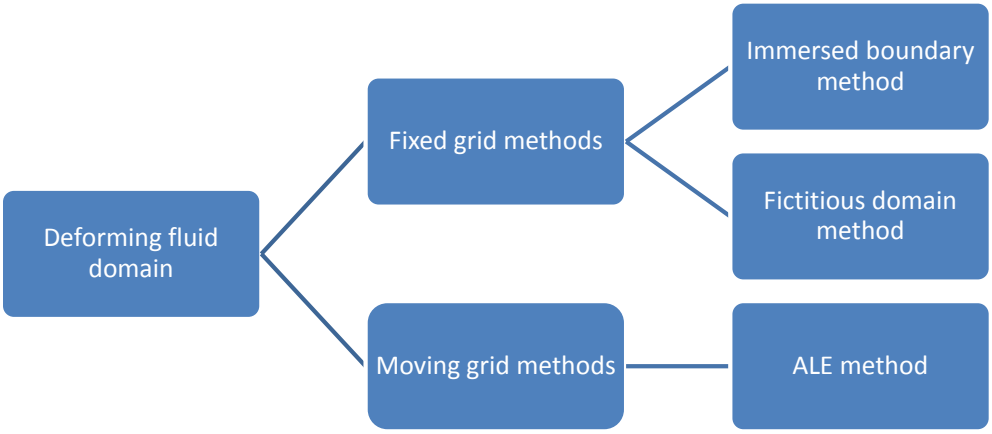

Figure 3.2: The flowchart illustrates the main methods for calculating the flow equations in a deforming fluid domain.

The fixed grid method is a non-boundary fitted method for which the fluid mesh remains unaltered in time. The influence of the structure is introduced by momentum sources in the momentum equations of the flow [116]. The first non-boundary fitted method was proposed by Peskin [78] and is now known as the immersed boundary method [79]. Another similar approach is the fictitious domain method described by Glowinski *et al.* [43]. The fictitious domain method can be seen as the finite element (FE) version of the immersed boundary method which is developed within the finite difference (FD) framework.

An advantage of the fixed grid methods is that the flow solver can be simple and fast because the fluid grid does not have to deform. A major drawback, on the other hand, is the loss of accuracy near the fluid-structure interface.

The moving grid method is a boundary fitted method where the fluid mesh moves with the moving interface throughout the computation. A common technique is to use the Arbitrary Lagrangian-Eulerian (ALE) formulation to express the Navier-Stokes equations on the moving grid. The ALE-formulation combines the best features of the Lagrangian and Eulerian descriptions and was first proposed by Donea *et al.* [34]. In the Eulerian formulation, the grid is fixed and the material moves through it. In the Lagrangian formulation, every grid point moves at the same velocity as their associated material point. In the ALE-formulation the grid and the material can move at different velocities. In other words, the grid can deform at an arbitrary velocity and not necessarily at the velocity of the fluid, hence the name. At the fluid-structure interface, the fluid grid follows the velocity of the structure. The resulting grid displacements at the interface will, in turn, be extended to the rest of the fluid domain by some mesh updating method. A common mesh updating method is called spring-based smoothing. In this method, the edges between any two mesh nodes are replaced by springs (see Ansys Fluent User's guide for more details on spring-based smoothing). However, if the deformations of the boundaries are large compared to the local cell sizes in the applied mesh, the grid elements might become ill-shaped, and hence, the spring-based smoothing alone is not sufficient. The solution is often to apply another mesh updating technique called local remeshing. The cells that violate some predefined criteria will then be remeshed when going to the next time step. However, frequently remeshing will increase the computational time. Another drawback is that the interpolation from the old to the new grid will introduce errors.

A great advantage of the ALE-formulation is that the wall shear stress at the fluid-structure interface can be calculated accurately. This is important in cardiac CFD simulations.

In this thesis, the ALE formulation has been used to express the Navier-Stokes equations on the moving grid. Due to the large deformations of the boundaries (both translations and rotations), both spring-based smoothing and local remeshing have been applied to update the fluid mesh.

3.2 Modeling the heart chambers

3.2.1 Time-varying geometry

Cardiac CFD simulations require detailed information about the geometry and the time-varying motion of the heart chambers. In the geometry-prescribed CFD approach, an initial geometry and a prescribed boundary motion needs to be implemented in the model. In the FSI approach, an initial geometry and an appropriate material model for calculating the mechanical behavior of the vessel wall is necessary. The FSI approach is promising, but currently no FSI method solves this problem with high accuracy. For a clinical *in situ* analysis and evaluation of cardiac flow, a geometry-prescribed CFD method is today better suited [98]. It is important to remember that the blood flow pattern will be the same whether the same wall motion is prescribed or computed by a coupled solution.

In both approaches, the geometries might be simplified and idealized or obtained from medical imaging. By simplifying the complex geometries to idealized models, valuable information might be lost. On the other hand, simplified models might be important pioneering steps on the way to more refined models. By rendering the geometries from medical imaging data, subject-specific CFD models might be obtained. Subject-specific CFD simulations can provide flow details on a level not possible by medical imaging alone. Such quantitative information can help us to understand the complex flow phenomenon occurring under both normal and pathological conditions.

The objective of this thesis was to use models and methods that could contribute to a better understanding of cardiac blood flow. In order to get sooner into clinical research, a geometry-prescribed CFD approach was chosen for the heart chambers. To obtain physiologically representative models, the time-varying geometries were rendered from medical imaging data. To understand pathological conditions we first have to understand the blood flow under healthy conditions. In this thesis we have mainly focused on the hemodynamics occurring under healthy conditions. We have therefore used the term ”subject-specific models” instead of ”patient-specific models” because our models are based on healthy people.

3.2.2 Subject-specific models based on medical imaging

Different imaging modalities like CT, MRI and ultrasound have in recent years been supported by simulation tools. CT has not been used in this thesis and will not be discussed further.

In most numerical studies, MRI has been used to obtain the transient geometries. MRI has a clear benefit with respect to image quality and has the advantage of producing anatomically detailed and functionally accurate datasets. MRI has also been a 3D method since its beginning. A drawback, however, is that the cardiac valves are less distinguishable due to high signal from blood. The reconstruction of a 4D (3D + time) volume is achieved over multiple heart cycles something which requires long acquisition time and the need for respiratory gating. A long acquisition time increases the cost of

the examination and inter-slice alignment errors might also occur due to different diaphragm positions in subsequent breath holds. MRI recordings cannot be performed on people with metallic implants, like some artificial heart valves. In such cases, MRI is not feasible for model building purposes. Due to high cost and complexity, the use of MRI is restricted on cardiac patients.

Cardiac ultrasound, often referred to as echocardiography, is, among medical doctors, the most applied method for diagnosing the heart. The particular strength of ultrasound is its ability to record moving structures in real-time and it can therefore be used to help guide invasive procedures. It is also a relatively easy and cost effective imaging technique. Another important advantage of echocardiography is the clear visualization of the cardiac valves. However, echocardiography yields larger inter-subject variation in image quality than MRI. 2D ultrasound has been on the market for several decades. 3D ultrasound, on the other hand, was first introduced by Philips in 2002. Since then, other providers of ultrasound systems have released systems with real-time 3D capabilities [25]. 3D ultrasound has undergone large improvements the last few years, and both image quality and temporal resolution are now at a level that makes it possible to extract high quality 3D geometries and deformations. There exists an extensive amount of 2D echocardiographic patient data. Now, 3D echocardiography is gaining popularity as a routine clinical tool.

In this thesis, we have mainly focused on building models based on cardiac ultrasound. There were several reasons for this choice. One is the extensive amount of patient data available and that ultrasound is the major imaging tool in cardiology. Furthermore, we assume that developing models from ultrasound data instead of MRI data might result in a more cost-effective, clinically viable tool with a broader area of application. If for example in-vivo recordings from patients with mechanical heart valves are necessary, ultrasound is better suited than MRI. Ultrasound also allows for real-time inter-active display of image data and therefore has the potential to help in guiding treatment. Another important benefit of using ultrasound is this project in our close collaboration with the medical ultrasound research group in Trondheim and their cooperation with GE Vingmed Ultrasound. Through this collaboration, we have access to the newest methods and latest developed segmentation tools.

3.2.3 The left ventricle

Most of the computational models of the heart have focused on the LV. The earliest work was mainly generic and did not rely on subject-specific data. In the last decade, both computational and imaging resources have increased and enabled the opportunity to create more refined subject-specific models.

In the beginning of the thesis, the 2D geometry of the LV was rendered from 2D echocardiographic recordings by a post-processing operation of EchoPAC PC (version 6.0.0, GE Vingmed Ultrasound, Norway) called speckle tracking (see chapter 6 and 7 and appendix A). In 2009, a mesh-based surface-tracking method called 4D AutoLVQ was introduced. 4D AutoLVQ provides a graphical output of pure 4D volume data from RT3DE. In the last part of the thesis, it was therefore possible to create a 3D model of the LV from RT3DE (see chapter 9 and appendix A). The endocardial border was here rendered using the AutoLVQ tool on an EchoPAC software workstation (version BT 11, GE Vingmed Ultrasound, Norway).

3.2.4 The left atrium

Relatively few studies have focused on modeling the LA. While the ventricular models have gotten more refined, the models of the left atrium are still mostly oversimplified. Even if the LA provides

the inlet conditions for the ventricle during diastole, the LA is most often excluded in simulations of intraventricular and transmitral flow. The atrial cavity is then replaced by an approximated inlet condition imposed directly at the mitral opening or at the end of some tube. However, the LA is far from being a passive transport chamber prior to the LV [14]. According to Fyrenius *et al.* [42], the normal LA has important roles in optimizing left ventricular filling.

It is possible to render the atrial geometry with 4D AutoLVQ, but, the details of the complex 3D LA geometry like the left atrial appendix and the entry locations of the pulmonary veins are today not easily detectable with this software. MRI is more effective in providing detailed and complete imaging of the LA and its PVs. In our 3D study of intra-atrial flow, we therefore chose MRI to provide the 3D geometry of the LA (see chapter 8).

3.2.5 Uncertainties

When numerical simulations are performed, the uncertainties should be addressed to know which errors that might have an influence on the simulation results. When the CFD models are based on medical imaging, the uncertainties will mainly originate from three stages. The first stage is the recordings of the medical images, the second is the segmentation and the subsequent geometrical reconstruction and the third is the numerical simulations.

To control whether the CFD model produces physiologically representative results, some validation is necessary. However, validations are generally difficult for subject-specific modeling because of the lack of a non-invasive gold standard for individual cases [64]. In-vivo flow measurements might be used to give an indication whether the results are within the physiological range. Both Echo-Doppler flow imaging and MR phase mapping can be used to obtain in-vivo flow measurements. However, a drawback of all techniques for measuring blood flow velocity in-vivo is the absence of a standard of reference. The overall error in the measurements is therefore difficult to estimate [66].

In this thesis, simulation results have been compared with in-vivo flow measurements obtained with MR phase mapping (see chapter 8 and appendix A). There are some challenges and limitations associated with MR flow measurements [24, 56]. However, MR is currently considered as the gold standard for non-invasive quantification of blood flow and velocity.

3.3 Modeling the mitral valve

The mitral valve has a complex geometry and movement pattern. The two mitral leaflets are thin, rapidly moving structures which undergoes large deformations during a heart cycle. To model the MV is a challenging task. Currently, there is no single method which is applicable to every problem. To find the method which is best suited, one should focus on the features of the given problem. If the interest lies only on the mechanical behavior of the valve, the interaction with the fluid flow does not have to be considered. If the focus is purely on the fluid dynamics, then the motion of the leaflets can be prescribed, e.g. from experimental data or medical imaging data. If it is important to have flow driven leaflets, an FSI approach is necessary.

Another aspect is whether the problem requires rigid or flexible heart valves or if a subject-specific model is desired. The majority of published heart valve models have focused on fluid motion near a monoleaflet or bileaflet mechanical valve in a steady flow [65]. A subject-specific model of the mitral valve is, on the other hand, a very challenging task. A subject-specific FSI model will require

subject-specific material parameters, something which is difficult or not even possible to obtain for a heart valve. A subject-specific geometry-prescribed model will require detailed information of the valve dynamics from medical imaging data, currently such information is difficult to obtain. Technical advances have enabled echocardiography to identify valve structures and the time resolution in echocardiographic recordings is also sufficient enough to capture the leaflets' motion. But, due to their rapid movement, the time-dependent shape of the valve leaflets is not easily extractable. There does not exist any automatic tool for valve segmentation, thus, manual tracking is the only alternative available today.

In the first part of the thesis, we focused on flow driven rigid leaflets (see chapter 6 and 7). We wanted to simulate two rigid, asynchronously moving mitral leaflets during ventricular filling. For this purpose we chose the partitioned FSI technique. Because the leaflets strongly interact with the surrounding fluid, an implicit coupling scheme was necessary to achieve equilibrium between fluid and structure. The implicit coupling scheme presented in chapter 6 is an extension of the coupling scheme for one leaflet developed in Vierendeels *et al.* [116] and validated in Dumont *et al.* [35]. The FSI algorithm was tested in a 2D simulation, where the mitral valve was rendered as two rigid asymmetric leaflets with lengths obtained from ultrasound recordings. The algorithm applies to 3D structures as well.

In the last part of the thesis, we focused on the fluid dynamics in a subject-specific 3D model of the LV (see chapter 9). The prescribed ventricular boundary conditions were obtained from RT3DE. A physiological representation of the MV was also desired in this 3D model. Because 3D tracking of heart valves from medical imaging data is a complicated and time-consuming task, we chose to use an advanced 3D finite element material model to represent the MV geometry [84]. A transient simulation of the FE MV model in Abaqus provided us with the time-dependent systolic movement of the valve. This prescribed valve motion was subsequently implemented as a boundary condition in the 3D CFD model. The FE MV model is not subject-specific, however the valve model can be modified to follow different subject-specific valve profiles, e.g. rendered from 2D echocardiographic images.

In addition, an initial study on how the curvatures of the mitral leaflets influence the systolic flow field is provided in appendix A. In this study we wanted to have full control of the valve motion, we therefore chose prescribed leaflet dynamics. The study was first performed in 2D, then in 3D. In the 2D study, we wanted to simulate two different types of leaflet curvatures and thereby compare the resulting ventricular flow field. For the first model, normal, healthy leaflet dynamics were desired. Hence, a code for tracking structures in 2D ultrasound images was written and used to obtain the systolic motion of the valve in a healthy subject. For the second model, we wanted a more irregular valve curvature with a higher degree of billowing. For this purpose the transient cross-sectional valve profile of the 3D FE MV model [84] was implemented as a boundary condition in the 2D simulation. An initial 3D CFD simulation was also performed. For this simulation we used the 3D model introduced in chapter 9, but with a modified MV geometry.

Chapter 4

Summary of appended papers

PAPER 1:

FSI-simulation of asymmetric mitral valve dynamics during diastolic filling
S.K. Dahl, J. Vierendeels, J. Degroote, S. Annerel, L.R Hellevik and B. Skallerud
Computer Methods in Biomechanics and Biomedical Engineering, 15(2), 121-130, 2012
In this article, we present an implicit coupling algorithm for the partitioned fluid structure interaction simulation of two asynchronously moving rigid bodies. The mutual interaction between the two bodies was accounted for by including the full Jacobian in the coupling iterations. The algorithm was used to perform a numerical simulation of mitral valve dynamics during diastolic filling. In numerical simulations of intraventricular flow and mitral valve motion, the asymmetry of the leaflets is often neglected. In this study the valve was rendered as two rigid, asymmetric leaflets. The two-dimensional simulations incorporated the dynamic interaction of blood flow and leaflet motion and an imposed subject-specific, transient left ventricular wall movement obtained from ultrasound recordings. By including the full Jacobian matrix in the algorithm, the speed of the simulation was enhanced and the total computational time was reduced by 22,5 % compared to using a diagonal Jacobian matrix. Furthermore, our results indicate that important features of the flow field may not be predicted by the use of symmetric leaflets or in the absence of an adequate model for the left atrium.

PAPER 2:

An assessment of left atrial boundary conditions and the effect of mitral leaflets on left ventricular filling
S. K. Dahl, E. Thomassen, J. Vierendeels, L. R. Hellevik and B. Skallerud
Inflow conditions are of great importance in numerical simulations. The aim of this study is to investigate, qualitatively, the effect of the left atrial geometry and the mitral valve on the flow field in the left heart. The study is performed through two-dimensional numerical models: a reference model which includes both an atrium and flow driven leaflets and two modified models where either the atrium or the leaflets are excluded. Our results indicate that atrial vortices will be generated if a more physiological representation of the atrium and venous inflows are included. The atrial vortices will cause a nonuniform velocity profile across the mitral opening, which in turn, influence the leaflets

dynamics and intraventricular flow pattern. To which extent the leaflets influence the intraventricular flow is a matter of discussion in the literature. Our simulations, with their limitations, indicate that the leaflets play a major role in the development of the flow field. The leaflets form an inflow tract which guides the flow into the ventricular cavity. The anterior leaflet also blocks the aortic outflow tract during filling and prevents vortices from being formed in this area.

PAPER 3:

Impact of pulmonary venous locations on the intra-atrial flow and mitral plane velocity profile

S. K. Dahl, E. Thomassen, L. R. Hellevik and B. Skallerud

Submitted 2011

In this paper we present a three-dimensional computational fluid dynamics framework of the left atrium and its pulmonary veins. The framework uses magnetic resonance imaging to render the subject-specific atrial and venous geometries. The aim was first to investigate the diastolic flow field in an anatomically representative model of the left atrium and the pulmonary veins. Second, to investigate the impact of different venous entry locations on the intra-atrial flow and on the resulting mitral plane velocity distribution. Three 3D models with different venous entry locations were created for this purpose. The mitral velocity profile in the model with anatomically based venous positions, showed qualitatively good agreement with the magnetic resonance flow measurements. When comparing the flow field in the three models, the results clearly illustrate that the pulmonary veins have a significant impact on the intra-atrial flow and the final mitral plane velocity profile. Because the interpatient variability in venous number and branching patterns is large, the mitral plane velocity profile should be considered as a subject-specific property. Therefore, we suggest that in order to obtain a physiological correct simulation of ventricular filling, a subject-specific representation of the left atrial and the pulmonary venous anatomy should be included in the model.

PAPER 4:

3D moving boundary conditions for heart CFD simulations - from echocardiographic recordings to discretized surfaces

S. K. Dahl, E. Fagerholt, G. Kiss, V. Prot, B. Amundsen, L. R. Hellevik and B. Skallerud

MekIT'11: Sixth National Conference on Computational Mechanics, 2011

In this paper we present a technique concerning the creation of subject-specific 3D moving boundary conditions for the simulation of flow inside a pumping left ventricle. The method uses real-time three-dimensional echocardiography to provide the time-dependent geometry of the left ventricular wall. The endocardial border was then generated using a semi-automated tool (4D AutoLVQ). A finite element mitral valve model was included in the left ventricular grid topology to represent the geometry and movement of the valve leaflets. To validate the correlation between the model and the echocardiographic recordings, the model was realigned with the original echocardiographic data. A reasonable agreement was obtained in this first model. One benefit of the presented approach is the simplicity of using replaceable parts. The software is capable of incorporating different models of the mitral valve, the outflow tract or the left ventricle, with a limited amount of user intervention.

4.1 Declaration of authorship

In paper 1, Sigrid Kaarstad Dahl built the model and performed all the numerical simulations. The group of Jan Vierendeels provided the coupling algorithm between the flow solver and the structural solver, whereas Sigrid Kaarstad Dahl adapted the algorithm to the specific structural solver. She also wrote the structural code. In paper 2, Sigrid Kaarstad Dahl built the models and performed all the numerical simulations. In paper 3, Sigrid Kaarstad Dahl performed all the numerical simulations. Espen Thomassen did the segmentation of the left atrium and created the geometrical models. Brage Amundsen performed the MRI acquisitions at St.Olavs University Hospital, Trondheim, Norway. In paper 4, Sigrid Kaarstad Dahl wrote the algorithms for creating 3D CFD models from echocardiographic data and further built the model. Victorien Prot and Bjørn Skallerud contributed with the finite element model of the mitral valve. Egil Fagerholt and Gabriel Kiss contributed with knowledge on image processing. Brage Amundsen performed the echocardiographic acquisitions and did the subsequent segmentation at St.Olavs University Hospital, Trondheim, Norway.

In papers 1, 2, 3 and 4, Sigrid Kaarstad Dahl wrote the manuscripts. The co-authors contributed constructive criticism that increased the scientific quality of the papers.

4.2 Publication list

The following is a list of all reasearch papers and conference contributions during my PhD where I have contributed as a main or co-author. The contributions marked with a star (*) are fully or partly included in the subsequent chapters and appendix.

Journal articles

* S. K. Dahl, E. Thomassen, L. R. Hellevik and B. Skallerud, Impact of pulmonary venous locations on the intra-atrial flow and mitral plane velocity profile, submitted, 2011.

S. Annerel, J. Degroote, T. Claessens, S. K. Dahl, B. Skallerud, L. R. Hellevik, P. Van Ransbeeck, P. Segers, P. Verdonck and J. Vierendeels, Application of a strong FSI coupling scheme for the numerical simulation of BMHV dynamics: Study of wall shear stress on the valve leaflets, Progress in Computational Fluid Dynamics, Accepted, 2011

S. Annerel, J. Degroote, T. Claessens, S. K. Dahl, B. Skallerud, L. R. Hellevik, P. Van Ransbeeck, P. Segers, P. Verdonck and J. Vierendeels, A Fast Strong Coupling Algorithm for the Partitioned Fluid-Structure Interaction Simulation of BMHVs, Computer Methods in Biomechanics and Biomedical Engineering, Accepted, 2011

* S. K. Dahl, J. Vierendeels, J. Degroote, S. Annerel, L. R. Hellevik and B. Skallerud, FSI simulation of asymmetric mitral valve dynamics during diastolic filling, Computer Methods in Biomechanics and Biomedical Engineering, 15(2), 121-130, 2012.

Peer-reviewed conference proceeding papers

* S. K. Dahl, E. Fagerholt, G. Kiss, V. Prot, B. Amundsen, L. R. Hellevik and B. Skallerud, 3D moving boundary conditions for heart CFD simulations - from echocardiographic recordings to discretized surfaces, in: MekIT'11: Sixth National Conference on Computational Mechanics, Trondheim, 23-24 May 2011. Tapir Akademisk Forlag 2011, ISBN 978-82-519-2798-7: p. 33-46.

* S. K. Dahl, J. Vierendeels, J. Degroote, S. Annerel, B. Skallerud and L. R Hellevik, Implicit interaction of two rigid mitral leaflets in a partitioned fluid-structure approach, in: MekIT'09: Fifth National Conference on Computational Mechanics, Trondheim 26-27 May 2009. Tapir Akademisk Forlag 2009, ISBN 978-82-519-2421-4: p. 135-149.

Conference abstracts

* S. K. Dahl and B. Skallerud, Effect of mitral valve shape on flow dynamics during left ventricular contraction. 6th World Congress on Biomechanics; Singapore, 1-6 August 2010.

S. K. Dahl, B. Skallerud and L. R. Hellevik, A 2D patient-specific FSI assessment of mitral valve dynamics during diastolic filling, 8th. World Congress on Computational Mechanics (WCCM8) and the 5th. European Congress on Computational Methods in Applied Sciences and Engineering (ECCOMAS 2008); Venice, 30 June-4 July 2008.

Invited speaker

S. K. Dahl, Fluid-structure interaction simulation of mitral valve dynamics in a subject-specific geometry during diastolic filling, MI-Lab seminar: Cardiac imaging and LV mechanics; 10 November 2009.

S. K. Dahl, Fluid structure interaction with an user defined subroutine, SINTEF: Fluent Users Group; Trondheim, 3 June 2009

Chapter 5

Conclusions and further work

5.1 Conclusions

Like most of the biomechanical problems, the project is multidisciplinary and involves scientific computing, mathematical modeling, fluid dynamics, structural mechanics and physiology. In this study different framework for the simulation of the hemodynamics in the left heart has been developed. Even though the work and applications in this thesis are focused on and motivated by gaining knowledge of the blood flow in the heart, the thesis also contributes to computational methodology for cardiac modeling. The main findings and developments are listed below:

- An implicit coupling algorithm for the partitioned FSI simulation of two rigid leaflets has been developed. The algorithm allows for asynchronous motion of two leaflets and is therefore also suitable for simulating bileaflet mechanical heart valves. The mutual interaction between the leaflets can be accounted for in the coupling iterations by including the full 2×2 Jacobian matrix. We compared the difference in convergence rate when we used the full Jacobian matrix versus the diagonal Jacobian matrix. The results show that including the full Jacobian matrix in the coupling iterations significantly enhanced the convergence rate and thereby the speed of the simulation. Overall, the total computational time was reduced by 22,5%.

  The algorithm was tested in a 2D simulation of the mitral valve during diastolic filling, where the valve was modeled as two rigid, asymmetric leaflets. Our results indicate that important features of the diastolic flow field may not be predicted by the use of symmetric leaflets or in the absence of an adequate model for the LA, particularly during diastasis and atrial contraction.

  The algorithm applies to 3D structures as well.

- Due to the complexity of the heart, the LA and the MV are often neglected in simulations of ventricular filling. However, it is important to know what impact such limitations might have on the resulting flow pattern. A qualitative investigation of the influence of left atrial inlet conditions and flow driven mitral leaflets on the diastolic ventricular flow pattern were performed. Three 2D models were created. In the reference model both the LA and the flow driven leaflets were included, while in the two other models, either the LA or the leaflets were excluded. The transient geometry of the LV was rendered from 2D echocardiographic recordings and the same wall motion was implemented in all the three models. It is important to notice that although the

investigated 2D models cannot simulate the real 3D filling process, some qualitative information can be obtained.

We observed that in the model where the LA and some venous inflows were included, vortices developed inside the LA during diastole. The atrial vortices caused a non-uniform velocity profile across the mitral opening, which in turn, influenced the leaflets' dynamics and the intraventricular flow pattern. In the model where the inflow region was rendered as a tube with the inlet at the far end, no vortices were generated in the inlet geometry and the resulting mitral velocity profile was approximately uniform. Based on our observations, we suggest that a realistic representation of the atrium should be included in simulations of LV filling and MV dynamics to achieve a physiologically representation of the velocity profile at the mitral orifice. However, 3D simulations are necessary for quantitative information of the intra-atrial flow field and the velocity distribution at the mitral plane.

No other studies have so far compared the intraventricular flow field with and without flow driven leaflets. The leaflets' influence was significant in our 2D study. The leaflets formed an inflow tract which guided the flow into the ventricular cavity and reduced the recirculation in the aortic outflow channel due to the presence of the anterior leaflet. This is an important new finding, but whether this is the case in a 3D ventricle with flexible leaflets has to be investigated further. Currently, such information is not easily available from 3D FSI models, due to limitations in the computational concepts and computational power.

- An anatomically based 3D CFD model of the LA and its PVs was developed from MRI data and used to investigate the flow field during diastole. Two additional models were constructed in order to examine the impact of venous entry locations on the intra-atrial flow and on the resulting velocity distribution at the mitral plane. The intra-atrial flow is made up of four crossing jets flowing into an asymmetric chamber and is therefore complex. Our results illustrate that the locations of the PVs have a significant impact on the intra-atrial flow and the mitral velocity profile. Our findings indicate that asymmetric located PVs might prevent instabilities in the flow field. We observed that in the anatomically representative model, where the PVs were asymmetrically located, the venous jets flowed towards the mitral plane without noticeable collision. This model also produced a more uniformly distributed mitral flow profile with lower maximal velocity than the two other models where the PVs were located at the same height. The mitral plane velocity profile in the anatomically representative model, showed qualitatively good agreement with MRI flow measurements.

  Due to its complexity, it is very difficult to predict the nature of the mitral jet by making general deductions about the conditions under which the jet is formed. The interpatient variability in PV number and branching patterns is large, hence, the mitral velocity profile should be considered as a subject-specific property. Therefore, a representative geometry of both the LA and the PVs is essential for physiological simulations of LV filling and MV dynamics. Our findings may influence future CFD studies regarding transmitral and intraventricular flow.

- A technique for creating subject-specific 3D boundary conditions for simulations of intraventricular flow has been developed. The algorithms provide a framework for the coupling of different data sets of the LV, the LVOT and the MV. Real-time 3D echocardiography was used to provide the time-dependent geometry of the LV wall. As far as we know, this is the first subject-specific 3D CFD model rendered from RT3DE.

It is difficult to obtain the 3D dynamics of the mitral leaflets from medical imaging data. A 3D FE MV model was therefore included in the LV grid topology to represent the geometry and movement of the valve leaflets. The FE MV model was pre-simulated in Abaqus, however only the systolic phase of the cardiac cycle was computed [84]. The prescribed valve motion and the final systolic curvature can be modified to follow different subject-specific valve curvatures, e.g. rendered from 2D echocardiographic images.

To examine the correlation between this first model and the echocardiographic recordings, the model was realigned with the original echocardiographic data. A reasonable agreement was obtained.

A preliminary CFD simulation of ventricular contraction was performed (Appendix A). As a first step for validation, the maximum velocity out of the LVOT was compared with in-vivo velocity measurements from MR phase mapping scans. The MR acquisitions were taken at the same day and in the same subject as the RT3DE acquisitions. Even if the velocities could not be directly compared, the comparison with the in-vivo flow measurements indicated that our results were within the physiological range.

5.1.1 General remarks

It is feasible to generate input data to computational cardiac models from several types of medical imaging modalities. However, developing models from ultrasound data instead of MRI data might result in a more cost-effective, clinically viable tool with a broader area of application. For example MRI acquisitions cannot be performed on people with metallic implants, like some artificial heart valves. Due to the findings in this project, subject-specific geometries of the LA and PVs should be included in simulations of LV filling. Though, we experienced that MRI was better suited to extract the complex LA geometry and particularly to render the geometry and entry locations of the PVs. However, considering the large improvements RT3DE and 4D AutoLVQ have undergone the last few years, further development might lead to high quality ultrasound rendering of the LA and PVs as well.

Due to the strong dependency of flow characteristics on the LV geometry and motion, the accuracy of the 3D geometry is a key factor in numerical simulations of intraventricular flow. It is well known that there is a systematic bias between RT3DE and MR volume measurements where echocardiography generates smaller volumes when compared to MRI [72]. This has to be taken into account when simulation results are interpreted. Although, there is a negative bias in EDV and ESV estimation for RT3DE measurements compared to MRI, the measured stroke volume lies in the same range as long as the negative bias in EDV and ESV are approximately the same.

5.2 Directions for further work

- The various modules developed in this project should be coupled together to improve the outcome of the simulations and to gain further knowledge about the hemodynamics in the left heart. Thus, both the systolic and the diastolic phase should be included. The mitral valve can be replaced by a BMHV where the developed FSI algorithm can be used for leaflet movement. A BMHV can also be placed in the aortic position, something which is widely used in the clinic. Another combination is to use a BMHV in the aortic position and the FE MV model as represented in Appendix A in the mitral position. The FE MV simulation should then be extended

to include the diastolic movement as well. Another option is to do a FSI simulation where the subject-specific chambers are coupled with the FE analysis of the MV model in a partitioned FSI approach. However, subject-specific material parameters of the mitral valve are difficult or not even possible to obtain and the FSI simulation will not be subject-specific regarding the mitral valve. FSI simulation of the complete valve closure is also a challenge, as the closed valve will split the flow domain in two separate regions. However, attempts of such simulations have been performed [49].

- A simulation environment offers flexible control of the boundary conditions and flow parameters. This gives the opportunity to easily alter the models and further check how the flow responds to the applied changes. This can for example be used to reduce the movement of the ventricular vessel wall or to change the orientation of a BMHV. Subject-specific models have the potential to predict the outcome of procedures on an individual level and thereby improve diagnosis and treatment planning. Thorough validation of the developed models is necessary prior to their use in clinical settings.

- To improve the outcome of the left atrial flow simulations and to extend its area of application. A future simulation model of the LA should include moving boundaries to correct for the influence the wall motion has on the intra-atrial flow field. By including moving boundaries and also the systolic phase, a more complete picture of the intra-atrial flow pattern can be obtained.

- The first subject-specific 3D CFD model based on RT3DE has been presented in this thesis. Some future improvements of the LV model are listed below:

  - The 3D LV model does not include LV torsion about the ventricular central axis. GE Vingmed has a recently developed application called 4D strain, which enables the user to follow material points and hence, to account for LV torsion. Effort should be put into extending the current CFD model to incorporate the torsion as well.
  - The papillary muscles and the chordae are missing in the LV model. Their influence on the flow field should be investigated to determine whether the subvalvular apparatus is important to include in future simulation models.
  - The algorithms used to create the transient boundary conditions for the CFD simulation, should be further improved to make the procedure more efficient.
  - Reproducibility analysis should be performed in order to determine how much the surface-tracking and volume measurements of the LV vary between acquisitions and how this will influence the simulation results. The RT3DE acquisitions must then be taken of the same subject on the same day with as small variations in heart rate as possible.
  - An ultimate goal is to have a methodology for 3D model construction from echocardiographic data incorporated into ultrasound scanner systems. Real-time CFD simulations can support the decision-making during surgical interventions and have the possibility of changing clinical practice.

- A normal, healthy mitral valve billow slightly into the LA during LV contraction. Changes in leaflet curvature might occur due to MV pathology or surgical interventions. However, one of the most common heart valve abnormalities is leaflet billowing which means that one or both

valve leaflets are bulging more than normal into the atrium during systole. Echocardiography identifies and assesses the extent of billowing, but no specific echocardiographic criteria that can differentiate normal from pathological billowing exists [12]. By adjusting the systolic shape of the leaflets in the 3D LV model, the resulting flow pattern can be investigated. Through cooperation with clinical personnel, it might be possible to develop echocardiographic criteria that would allow to differentiate normal from pathological billowing leaflets. The project can also be extended to include prolapse and flail which causes mitral regurgitation. A preliminary study on this topic is provided in Appendix A. The initial results from this study indicate that the shape of the anterior leaflet affects the aortic outflow profile. This might be an important new finding and should be further investigated.

- Today, different imaging modalities are used for generating subject-specific boundary conditions for CFD simulations. It would have been interesting to compare 3D CFD models based on RT3DE with models based on MRI and CT, to assess the differences that might occur. The recordings should then be obtained on the same day of the same subject having approximately the same HR in all the acquisitions. Experienced personnel should be used in order to reduce potential sources of error [72]. A possible follow-up study might be to combine the strengths of several modalities into one single model. For example RT3DE is better at the valve, whereas MRI provides a sharper delineation of the myocardium. MRI could then be used to obtain the geometry at time point zero and RT3DE for real-time movement and for the valve geometry. The framework developed in this thesis supports to combine different models from different imaging modalities.

- Another interesting usage of CFD simulations is to link them with ultrasound imaging simulations [10, 107, 108]. The CFD simulation provides the velocity distribution at any point in the domain. Based on this velocity field, ultrasound simulations can be made using established and experimental acquisition setups. In the end, the ultrasound method can be compared to the true reference CFD velocities. This is a versatile tool to validate and develop flow imaging methods with flexible control over both the flow and imaging setup. Coupling subject-specific CFD models of the LV with ultrasound imaging simulations can increase the understanding of conventional flow imaging in echocardiography and its limitations in the quantification of flow patterns. It might also contribute to improve and further develop flow imaging techniques for the cardiac domain.

Part II

Research papers

Chapter 6

FSI-simulation of asymmetric mitral valve dynamics during diastolic filling

FSI-simulation of asymmetric mitral valve dynamics during diastolic filling
S.K. Dahl, J. Vierendeels, J. Degroote, S. Annerel, L.R Hellevik and B. Skallerud
Computer Methods in Biomechanics and Biomedical Engineering, 15(2), 121-130, 2012

6.1 Introduction

The mitral valve (MV) separates the left ventricle (LV) and left atrium (LA) in the heart. It consists of two leaflets with significantly different geometries, namely the anterior and posterior leaflet. The valve allows flow of blood into the LV during diastole and prevents back flow into the LA in systole. The mitral valve moves in response to the blood flow, associated pressure differences over the leaflets and leaflet muscle fiber activation [103] resulting from a complex interaction of wall tension in the LA/LV and the flow pattern in each compartment. During the filling phase, namely the diastole, the LA directs inflow from the pulmonary veins (PVs) towards the MV. The filling phase corresponds with continued LV relaxation which increases the pressure difference between the two chambers and therefore assists the valve opening. As the ventricle fills, it becomes stiffer and an atrial contraction at end-diastole is needed to force blood into the distended ventricle.

In the past few years, a number of papers have been published concerning fluid-structure interaction (FSI) of leaflets in a fluid. Some of the studies have simulated one leaflet, either in aortic position [28, 36, 37, 40, 105, 106, 113, 116] or in mitral position [20, 77, 106, 114]. Others have simulated two or more leaflets in the aortic position [6, 11, 15, 18, 22, 23, 45, 73, 75, 76], while just a few have simulated two leaflets in the mitral position [38, 39, 68, 78, 80, 117]. Numerical techniques for flows with moving boundaries can broadly be classified in two main categories: moving grid methods which is mainly the Arbitrary Lagrangian Eulerian (ALE) method, and fixed grid methods like the immersed boundary method. In this study we shall focus on the ALE-method where a fluid solver and a structural solver are coupled in an iterative procedure. Of the above mentioned papers, the ALE-method was applied by [20, 23, 36, 37, 40, 45, 73, 75, 76, 116]. Those accounting for two or three leaflets, [23, 45, 73, 75, 76], did not explain if or how the mutual interaction between the leaflets was included in the coupling algorithm.

In several studies on the fluid-structure interaction of the mitral valve, a common assumption is the neglection of geometrical realistic models for the ventricular and atrial geometries and motions. Simulations with geometrical realistic models of the LV exists, but in those studies the complex phenomena of blood-leaflet interaction is avoided. The only papers we found which included both a moving LV and the blood-leaflet interplay were the work done by [68, 80]. In the other studies the LV was modeled as a straight tube [20, 39, 77, 78, 106, 114, 117] or with a more realistic, but fixed, 2D geometry [39]. In all of the mentioned studies, the LA was simplified to a straight tube.

In this paper we report results from an FSI study on the MV behavior during LV filling. An implicit ALE-procedure was implemented for the rigid body motion of the mitral leaflets. The leaflets were simulated with an asymmetric geometry and their motion was computed with an FSI coupling scheme that accounts for the mutual interaction of the leaflets. To the best of our knowledge, such an algorithm was not presented before. To achieve physiological realism in the simulations, ultrasound recordings with speckle tracking were utilized to render the subject-specific left ventricular wall movement of a healthy young person. The specific movement was imposed as a boundary condition in a 2D transient simulation of diastolic filling. As far as we know, ultrasonic speckle tracking has never been utilized for this purpose before.

The aim of this work was twofold: first, to develop an FSI algorithm for the implicit coupling of two rigid, asymmetric leaflets based on the coupling scheme of Vierendeels *et al.* [116], and second to study the impact of asymmetric leaflet motion on LV filling pattern. The actual problem of FSI in the left ventricle is three-dimensional, and as such one can argue that our simulations should be in 3D. However, we take a two-step approach with a 2D study first in order to investigate on simple

models whether the algorithm works satisfactory. Also, it is easier to interpret 2D results and learn from these before we carry out the second step in our study, i.e. the 3D analyses.

6.2 Models and methods

6.2.1 Geometrical model

To reconstruct the anatomical geometry of the LV chamber, two dimensional ultrasound recordings of a young healthy adult (26 years) without any known history of heart disease, were performed. Subject-specific data for the transient LV wall geometry and movement was obtained in a post-processing operation with the speckle tracking option of EchoPAC PC (version 6.0.0, GE Vingmed Ultrasound, Norway). The speckle tracking algorithm works within a region of interest (ROI) which must be defined by the user. For the LV wall, a ROI of 93 points was specified, their corresponding coordinates were recorded at 37 time frames throughout the heart cycle. The ROI in the particular ultrasound image is depicted as colored dots in Fig.6.1.

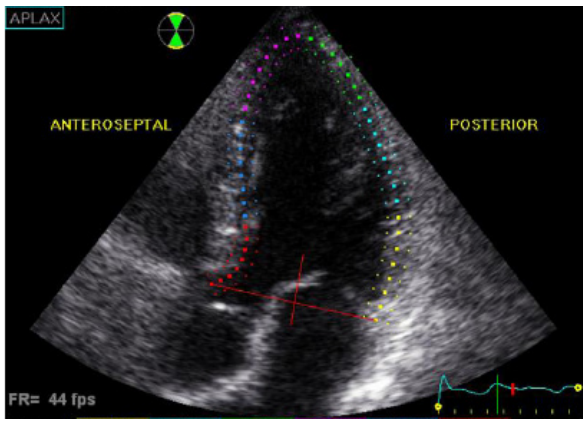

Figure 6.1: The region of interest (ROI) for the ventricular wall. ECG in the lower right corner.

The end points of the ROI were set to follow the annulus and the aortic outflow tract at their posterior and the anterioseptal sides, respectively. In this way, the longitudinal movement of the annulus was included in the measurements. In Fig.6.1, the ECG is plotted in the lower right corner. The green vertical line marks the start of our simulation, i.e. early diastole. The short red line depicts the instant when the displayed image was taken.

The inflow region was modeled as a typical, but fixed, atrium with two inlets in the upper part, each reflecting an orifice of a pulmonary vein.

The leaflets were modeled as two separate rigid bodies, rotating around their annulus attachment points. The anterior and posterior valve lengths were taken as $l_a = 19.9\ mm$ and $l_p = 6.6\ mm$, respectively. The choice of lengths was based on ultrasound recordings. The thickness was set to be uniformly $t = 1.0\ mm$ for both leaflets.

6.2.2 Numerical method

The numerical simulations were performed with the finite-volume CFD software Fluent 6.3.26 (Ansys Inc.), which offers a dynamic mesh feature for flows with moving boundaries. However, any other CFD code with moving mesh capabilities could be used instead. The solution of the Navier Stokes equations for deforming meshes in the flow solver is provided by the use of the ALE formulation, which makes it possible to include grid velocities in the momentum and continuity equation of the fluid domain. The domain was discretized with triangular cells. The grid density was increased around the leaflets to allow for to their large motions. Due to limitations in the dynamic mesh module, a gap is required between the moving parts to maintain a continuous fluid domain. A two cell gap of $0.5\ mm$ between the leaflets and the wall, and a two cell gap of $0.6\ mm$ between the two leaflets in their closed position, were included in the model.

The blood was modeled as an incompressible, Newtonian fluid, with properties representative for healthy human blood, a density of ρ = 1056 kg/m^3 and a dynamic viscosity of $3.5 \cdot 10^{-3}\ kg/ms$ [20]. Laminar flow is assumed.

The dependence of the results on the time step has been analyzed. The results do no longer change significantly when the physical time step is reduced from 0.2ms to 0.1ms. The diastole (0.43s) was thus discretized with 2150 time steps.

6.2.3 Boundary and initial conditions

The prescribed motion of the ventricular wall was implemented in the flow solver using a user-defined function (UDF). A no-slip condition was imposed on the walls. Since the ventricle expands during filling, no outlet was defined. A pressure corresponding to a typical diastolic pressure history in the LA was applied as an inlet condition on each pulmonary vein opening. Only the diastolic period after the onset of MV opening was considered. The pressure curve was scaled to the period of the ultrasound measurements.As an initial condition, the pressure in both LA and LV was set to $1200\ Pa$, which corresponds to the average pressure in the chambers when the pressure gradient changes direction and the MV is about to open. The initial position of the valve was its closed position. The prescribed LV expansion will drive the flow.

6.2.4 Fluid structure interaction method

Fluent 6.3.26 does not have a built-in procedure for implicit solutions of FSI problems. However, FSI procedures can be implemented using UDFs for the structural part, and an external subroutine which enables control of the time-iteration/sub-iteration procedure.

The problem has two degrees of freedom, one for each leaflet. The equation of motion can be written as: $\mathbf{M} = \mathbf{I} \cdot \ddot{\boldsymbol{\theta}}$ where $\mathbf{M}$ is the torque applied on the leaflet's external surface by the pressure and the viscous force, $\mathbf{I}$ the moments of inertia, $\ddot{\boldsymbol{\theta}}$ is the angular acceleration of the leaflets. The component for the anterior and posterior leaflet is given by subindex 1 and 2, respectively:

$$\begin{bmatrix} M_1 \\ M_2 \end{bmatrix} = \begin{bmatrix} I_1 & 0 \\ 0 & I_2 \end{bmatrix} \cdot \begin{bmatrix} \ddot{\theta}_1 \\ \ddot{\theta}_2 \end{bmatrix} \tag{6.1}$$

The moment of inertia for each leaflet is approximated as for a thin rectangular plate of unit depth: $I_j = \frac{1}{3} m_j\ (l_j^2 + t_j^2)$, where $m_j = \rho_{leaflet} \cdot l_j \cdot t_j$ denotes the mass per unit depth, $\rho_{leaflet}$ the density of the leaflet $(1100 kg/m3)$, t the thickness and l the length of the leaflet, $j = 1, 2$.

The flow diagram of the implicit coupling between the flow and the two leaflets is shown in Fig.6.2. The coupling algorithm consists of two loops: one time loop and one subiteration loop. The coupling scheme presented here is an extension of the coupling scheme for one leaflet developed in Vierendeels *et al.* [116] and validated in Dumont *et al.* [35].

The coupling algorithm starts with initialization of all the UDF variables t, n, k, θ, $\dot{\theta}$, $\ddot{\theta}$. The subsequent position of the leaflets at time level $t + \Delta t$ is calculated by coupling the time-integration scheme for the solid with the CFD-code. Dynamic mesh simulations in Fluent only work with first-order time advancement, thus a backward Euler first-order implicit scheme was utilized for the fluid problem. From the stability analysis of Vierendeels *et al.* [116] we know that matching of the time integration scheme for the fluid and the solid problem is important. The backward Euler scheme was therefore utilized for the calculation of the leaflet's velocity and position:

$$\begin{aligned} \dot{\theta}_j^{n+1} &= \dot{\theta}_j^n + \Delta t \cdot \ddot{\theta}_j^{n+1} \\ \theta_j^{n+1} &= \theta_j^n + \Delta t \cdot \dot{\theta}_j^{n+1} \end{aligned} \tag{6.2}$$

To obtain the acceleration $\ddot{\theta}_j^{n+1}$ required to estimate the velocity $\dot{\theta}_j^{n+1}$ and position θ_j^{n+1} at timestep $t + \Delta t$ (Eq. 6.2), an iterative approach is used. For each timestep n, k subiterations are performed to reach the equilibrium between fluid and structure. The subiterations are indicated with a second superscript. A way to have implicit coupling in the subiterations, is to compute $\ddot{\theta}_j^{n+1,k+1}$ with a linear approximation of the moment $M_j^{n+1,k+1}$:

$$\mathbf{M}^{n+1,k+1} \approx \mathbf{M}^{n+1,k} + \frac{\partial \mathbf{M}}{\partial \ddot{\boldsymbol{\theta}}} \cdot \left(\ddot{\boldsymbol{\theta}}^{n+1,k+1} - \ddot{\boldsymbol{\theta}}^{n+1,k} \right) = \mathbf{I} \cdot \ddot{\boldsymbol{\theta}}^{n+1,k+1} \tag{6.3}$$

The above equation, requires knowledge of the Jacobian $\frac{\partial \mathbf{M}}{\partial \ddot{\boldsymbol{\theta}}}$. When simulating two leaflets, their mutual interaction can be included in the coupling iteration. If each of the leaflets is moved separately by using an algorithm for one leaflet twice, the Jacobian will be a diagonal matrix only including the derivatives $\frac{\partial \mathrm{M}_1}{\partial \ddot{\theta}_1}$ and $\frac{\partial \mathrm{M}_2}{\partial \ddot{\theta}_2}$, hence the leaflets' influence on each other will be neglected during the coupling iteration. By also including the derivatives: $\frac{\partial \mathrm{M}_1}{\partial \ddot{\theta}_2}$ and $\frac{\partial \mathrm{M}_2}{\partial \ddot{\theta}_1}$, the Jacobian will be a full 2×2 matrix and the leaflets' mutual interaction will be captured. The Jacobian is then written as follows:

$$\frac{\partial \mathbf{M}}{\partial \ddot{\boldsymbol{\theta}}} = \begin{bmatrix} \frac{\partial \mathrm{M}_1}{\partial \ddot{\theta}_1} & \frac{\partial \mathrm{M}_1}{\partial \ddot{\theta}_2} \\ \\ \frac{\partial \mathrm{M}_2}{\partial \ddot{\theta}_1} & \frac{\partial \mathrm{M}_2}{\partial \ddot{\theta}_2} \end{bmatrix} \tag{6.4}$$

As the value of the derivatives only affects the convergence rate, the Jacobian is calculated once in the beginning of each time step [116]. It takes three subiterations to estimate the full 2×2 Jacobian matrix. At $(k = 0)$, a first approximation of the velocities $\dot{\theta}_j^{n+1,0}$ and positions $\theta_j^{n+1,0}$ at $t + \Delta t$ are estimated with the old values of the angular accelerations $\ddot{\theta}_j^n$. The flow solver is then called to update the mesh and to solve the Navier-Stokes equations. After convergence of the Navier-Stokes equations, $M_j^{n+1,0}$ is calculated. In the second subiteration $(k = 1)$, the posterior leaflet is kept in the same position as in $(k = 0)$, $\theta_2^{n+1,1} = \theta_2^{n+1,0}$, while the position of the anterior leaflet is updated by perturbing its angular acceleration with a constant $\delta\ddot{\theta}_1 = 100\ rad/s^2$ (Eq.6.5). It is shown that the choice of this value is application dependent, but that the result is not very sensitive to this choice [116]. The minimal value of this parameter is related to the convergence criterion of the residuals,

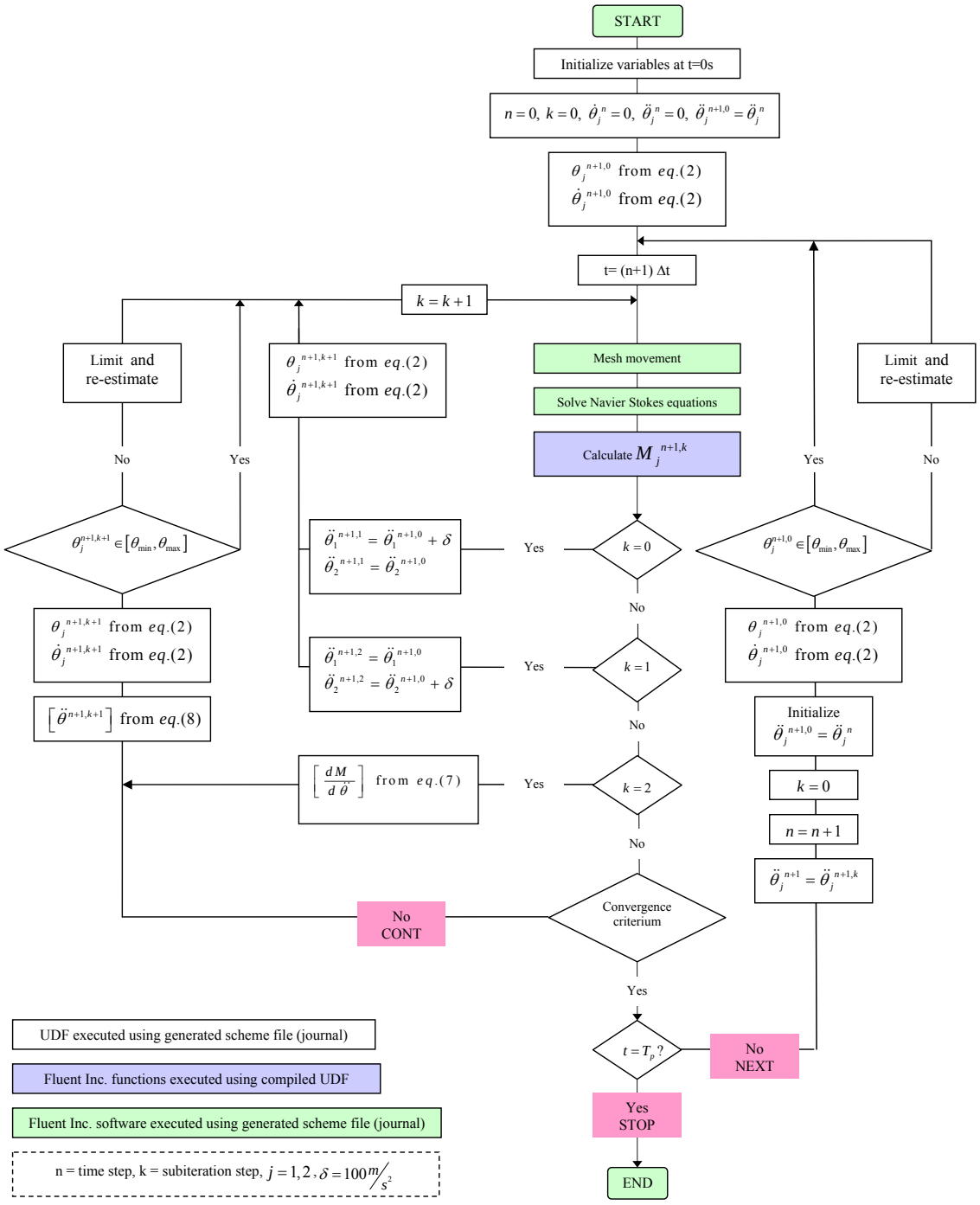

Figure 6.2: Flow diagram of the implicit coupling between the flow and the two leaflets

while a too large value can lead to divergence of the moving mesh solver because the displacement that corresponds to it becomes too large.

$$\begin{aligned} \ddot{\theta}_1^{n+1,1} &= \ddot{\theta}_1^{n+1,0} + \delta\ddot{\theta}_1 \\ \ddot{\theta}_2^{n+1,1} &= \ddot{\theta}_2^{n+1,0} \end{aligned} \tag{6.5}$$

This second iteration step results in $M_j^{n+1,1}$. There is now sufficient information to estimate the derivatives $\frac{\partial \mathrm{M}_1}{\partial \ddot{\theta}_1}$ and $\frac{\partial \mathrm{M}_2}{\partial \ddot{\theta}_1}$ (Eq.6.7). To avoid a singular Jacobian, the next perturbation (Eq.6.6) is done in a direction normal to the last perturbation (Eq.6.5). The anterior leaflet is set back to its initial position $\theta_1^{n+1,2} = \theta_1^{n+1,0}$, while the position of the posterior leaflet is updated by perturbing the angular acceleration at $(k = 0)$ with a constant $\delta\ddot{\theta}_2 = 100\ rad/s^2$:

$$\begin{aligned} \ddot{\theta}_1^{n+1,2} &= \ddot{\theta}_1^{n+1,0} \\ \ddot{\theta}_2^{n+1,2} &= \ddot{\theta}_2^{n+1,0} + \delta\ddot{\theta}_2 \end{aligned} \tag{6.6}$$

A third estimation of the velocities $\dot{\theta}_j^{n+1,2}$ and positions $\theta_j^{n+1,2}$ can now be computed and after convergence of the fluid problem, $M_j^{n+1,2}$ is calculated. There is now enough information to estimate the two remaining derivatives $\frac{\partial \mathrm{M}_1}{\partial \ddot{\theta}_2}$ and $\frac{\partial \mathrm{M}_2}{\partial \ddot{\theta}_2}$. The equations for the four derivatives are as follows:

$$\begin{aligned} \tfrac{\partial M_1}{\partial \ddot{\theta}_1} &= \tfrac{M_1^{n+1,1} - M_1^{n+1,0}}{\delta\ddot{\theta}_1} \\ \tfrac{\partial M_2}{\partial \ddot{\theta}_1} &= \tfrac{M_2^{n+1,1} - M_2^{n+1,0}}{\delta\ddot{\theta}_1} \\ \tfrac{\partial M_1}{\partial \ddot{\theta}_2} &= \tfrac{M_1^{n+1,2} - M_1^{n+1,0}}{\delta\ddot{\theta}_2} \\ \tfrac{\partial M_2}{\partial \ddot{\theta}_2} &= \tfrac{M_2^{n+1,2} - M_2^{n+1,0}}{\delta\ddot{\theta}_2} \end{aligned} \tag{6.7}$$

From now on, the Jacobian can be used to calculate better approximations of the angular accelerations. Rewriting Eq.(6.3) gives:

$$\begin{bmatrix} \ddot{\theta}_1^{n+1,k+1} \\ \ddot{\theta}_2^{n+1,k+1} \end{bmatrix} = \begin{bmatrix} \mathrm{I}_1 - \frac{\partial \mathrm{M}_1}{\partial \ddot{\theta}_1} & -\frac{\partial \mathrm{M}_1}{\partial \ddot{\theta}_2} \\ -\frac{\partial \mathrm{M}_2}{\partial \ddot{\theta}_1} & \mathrm{I}_2 - \frac{\partial \mathrm{M}_2}{\partial \ddot{\theta}_2} \end{bmatrix}^{-1} \cdot \left[\begin{bmatrix} M_1^{n+1,k} \\ M_2^{n+1,k} \end{bmatrix} - \begin{bmatrix} \frac{\partial \mathrm{M}_1}{\partial \ddot{\theta}_1} & \frac{\partial \mathrm{M}_1}{\partial \ddot{\theta}_2} \\ \frac{\partial \mathrm{M}_2}{\partial \ddot{\theta}_1} & \frac{\partial \mathrm{M}_2}{\partial \ddot{\theta}_2} \end{bmatrix} \cdot \begin{bmatrix} \ddot{\theta}_1^{n+1,k} \\ \ddot{\theta}_2^{n+1,k} \end{bmatrix} \right] \tag{6.8}$$

With these updated values of the angular accelerations, the new velocities and positions can be calculated and the flow solver is again called to update the mesh, to solve the Navier-Stokes equations and to calculate new moments $M_j^{n+1,k}$. For a fully implicit procedure, the moment $M_j^{n+1,k}$ calculated by the flow solver must be balanced by the angular acceleration $I \cdot \ddot{\theta}_j^{n+1,k}$:

$$\left| M_j^{n+1,k} - I_j \ddot{\theta}_j^{n+1,k} \right| \leq \varepsilon \ \ (no\ sum\ on\ j) \tag{6.9}$$

A relative convergence criterion with a residual drop of three orders of magnitude is applied. The criterion is restricted by a lower limit of $10^{-6}\ Nm$, to avoid very small values in the beginning of the calculation. If the requirement is not fulfilled, a better approximation $\ddot{\theta}_j^{n+1,k+1}$ has to be computed. When equation Eq.(6.9) is fulfilled for both leaflets, the simulation can move on to the next timestep. The simulation ends at $t = T_p$, where T_p is the end of the diastole.

A physiological restriction has to be imposed on the leaflet's position, $\theta_j^{n+1,k+1}$. When one leaflet exceeds its limits $\theta_j^{n+1,k+1} \leq \theta_j^{\min}$ or $\theta_j^{n+1,k+1} \geq \theta_j^{\max}$, its value is set equal to $\theta_j^{\min}$ or $\theta_j^{\max}$, respectively. New velocities $\dot{\theta}_j^{n+1,k+1}$ and accelerations $\ddot{\theta}_j^{n+1,k+1}$ will now be re-estimated from this limited angle. Hence, the position of the other leaflet is recalculated and has to be examined and so forth. The convergence criterion for the limited case is different. The subiteration loop is converged when equilibrium of equation Eq.(6.10) is fulfilled:

$$M_j^r + M_j^{n+1,k} - I_j \cdot \ddot{\theta}_j^{n+1,k} = 0 \ \ (no\ sum\ on\ j) \tag{6.10}$$

Here M_j^r is the reaction moment exerted by the contact point. M_j^r can only have one sign, depending on θ_j^{min} or θ_j^{max}.

6.3 Results

A convergence study for the number of subiterations when using a diagonal Jacobian matrix without coupling of the leaflets, versus the full 2×2 Jacobian matrix with coupling of the leaflets (Eq.6.4) is shown in Fig.6.3. The graph demonstrates that the full Jacobian matrix gives a better convergence throughout the computation. In the beginning of the simulation the convergence rate is up to 69 % faster. After approximately 150 time steps the convergence rate stabilizes, where the simulation with the full 2×2 Jacobian matrix is about 20 % faster.

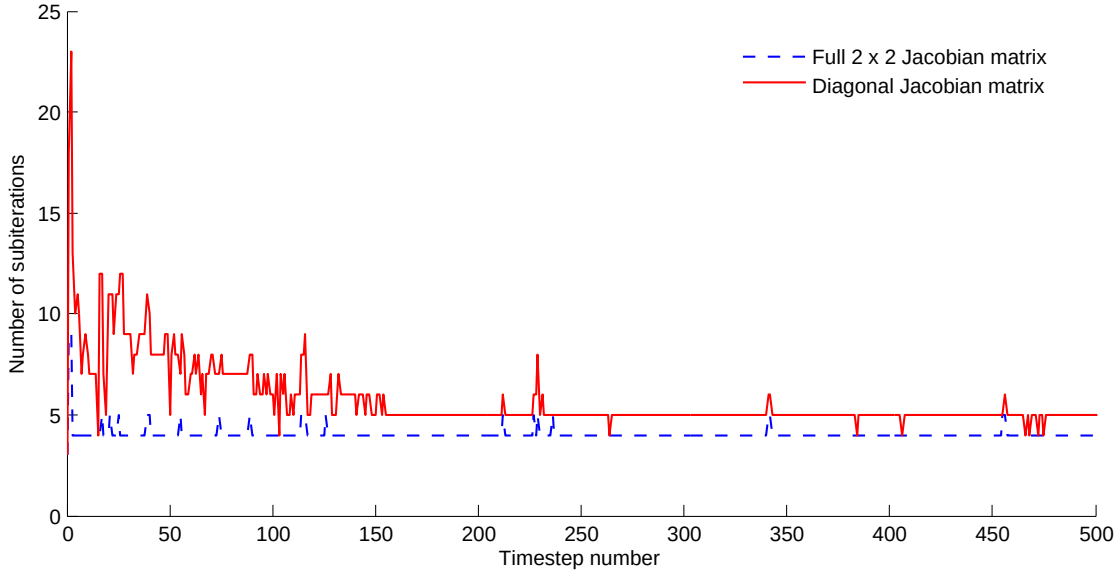

Figure 6.3: Convergence using the diagonal Jacobian matrix versus the full 2×2 Jacobian matrix.

In Fig.6.4, the opening angle of the simulated valve is plotted against the opening of a natural MV, measured in the same ultrasound recordings as the LV wall movement. The three stages of the diastole can be identified in the graph. These are early-diastole that depicts the rapid or early filling phase, mid-diastole or the diastasis, that shows the partial closing, and end-diastole, which represents the second opening due to atrial contraction.

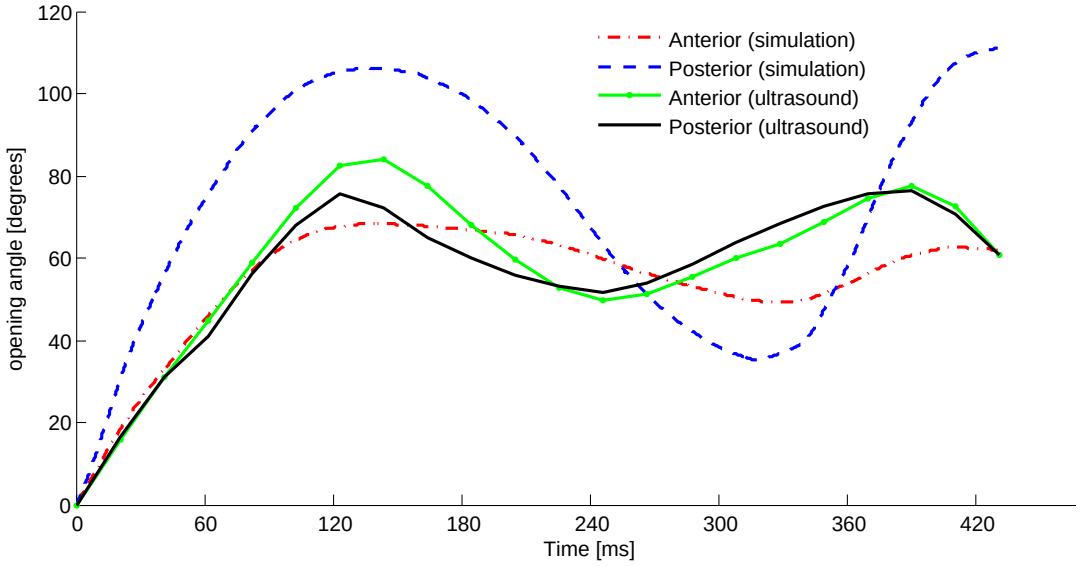

Figure 6.4: Opening angle versus time of simulated and measured mitral leaflets.

During early diastolic filling, the simulated anterior leaflet's opening angle coincides relatively well with the measurements. In mid- and end-diastole there are some deviations between the simulation and the measurements. The posterior leaflet, on the other hand, has higher angular velocities throughout the simulation. However, despite some variations, the simulated leaflets follow the same main pattern as in the measurements. In the ultrasound recordings the opening velocities of the posterior and anterior leaflet do not deviate much from each other. In the simulation, the two leaflets have significantly different velocities.

Fig. 6.5 shows the initial grid and seven sequential velocity-vector plots at time intervals of approximately 60 ms. When the ventricular pressure falls below the atrial pressure, the rapidly changing LA - LV pressure gradient leads to an opening of the valve. In this first filling phase, ((b)-(c)), the transmitral flow is almost uniform. No vortices are observed in the LV, while a vortex has started to develop at each PV orifice in the LA. As the blood flows into the ventricle, the atrio-ventricular pressure gradient decreases and reaches a minimum value in mid-diastole/diastasis ((d)-(f)). This causes a deceleration of the transmitral flow and the leaflets are now drifting back towards the annulus. This is called the partial closure. Two large vortices develops in the LA during diastasis. A vortex also starts developing at the tip of each leaflet, probably enhancing the partial closing seen in mid-diastole. The vortex developing behind the anterior leaflet is larger and more intense then the vortex behind the posterior leaflet. During the deceleration of the first filling wave((d)), the velocity distribution across the mitral annulus is slightly skewed. The inflow at the anterior side of the annulus has ceased, while it continuous at the posterior side. In the two subsequent plots, ((e)-(f)), the transmitral flow is almost zero.

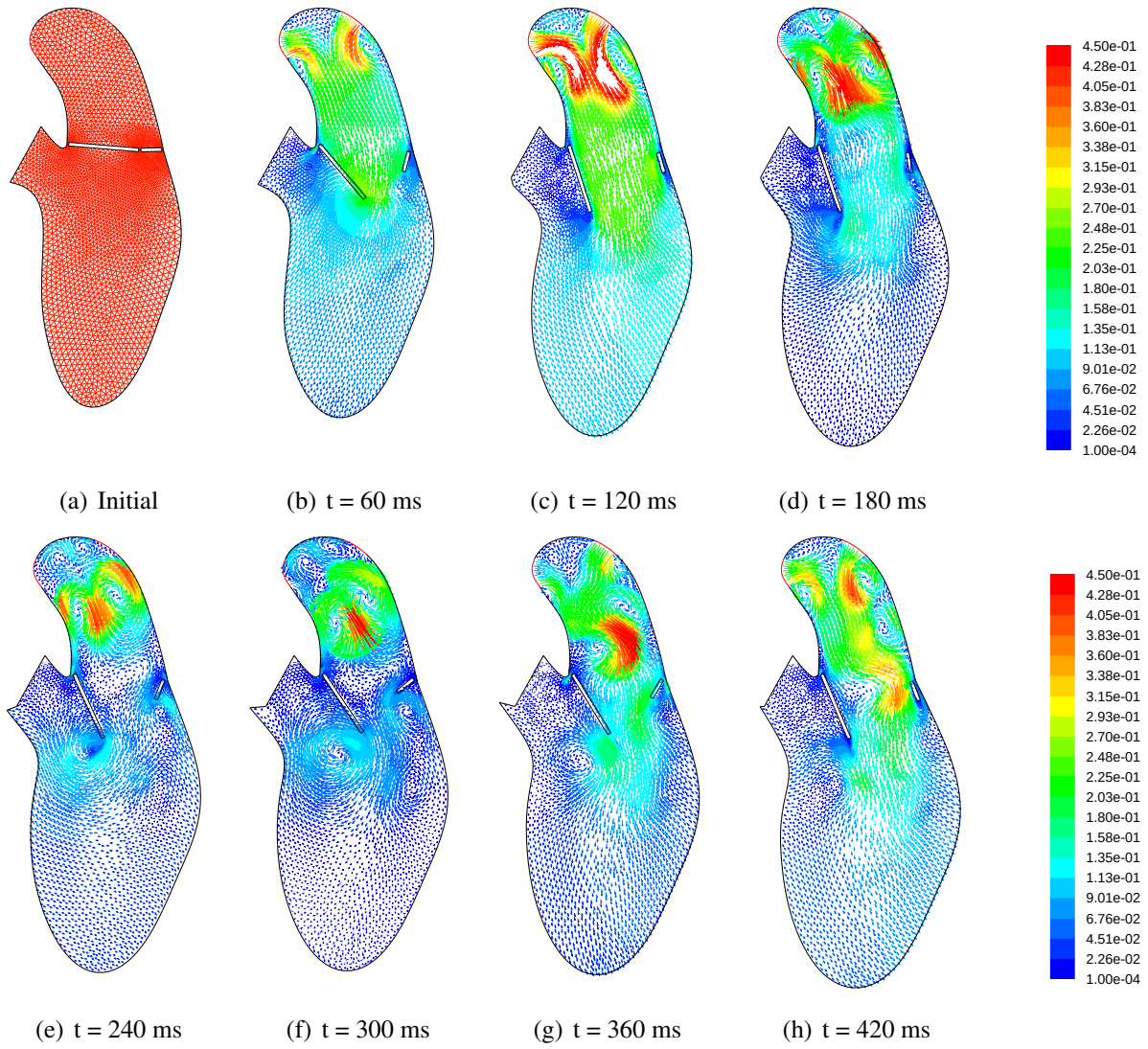

(a) Initial (b) t = 60 ms (c) t = 120 ms (d) t = 180 ms

(e) t = 240 ms (f) t = 300 ms (g) t = 360 ms (h) t = 420 ms

Figure 6.5: Initial grid and velocity vectors at seven different times during diastole, the velocity scale to the right is given in $[m/s]$

At the end of diastasis, $t = 330\ ms$, the atrium contracts and the pressure gradient increases causing a second acceleration of flow into the ventricle ((g)-(h)). The valve opens and the vortices at the leaflets tips become less intense. The vortices developed in the LA during diastasis, disappear through the MV opening, resulting in a prominent asymmetric transmitral flow with a high velocity at the posterior side. At the very end of diastole, the atrio-ventricular pressure gradient decreases again. The flow is retarding, the leaflets have started to drift back, but due to inertia the blood continues to flow through the MV (Fig.6.5(h)), predominantly near the posterior side.

The prescribed motion of the LV during filling can be seen as time progresses. It is evident that variations in shape and volume occur during diastole.

6.4 Discussion

In this study an FSI algorithm accounting for the mutual interaction between two rigid leaflets has been developed. If each of the leaflets is moved separately by using an algorithm for one leaflet twice, the Jacobian will be a diagonal matrix and the leaflets mutual influence will be neglected during the coupling iteration. By also including the derivatives: $\frac{\partial \mathrm{M}_1}{\partial \ddot{\theta}_2}$ and $\frac{\partial \mathrm{M}_2}{\partial \ddot{\theta}_1}$, the Jacobian will be a full 2×2 matrix and the leaflets mutual interaction will be captured. We compared the difference in performance when we used the full 2×2 Jacobian matrix versus the diagonal Jacobian matrix. The results demonstrate that including the full 2×2 Jacobian matrix significantly enhances the speed of the simulation. During the first 50 time steps, the rate of convergence is up to 69 % faster. As the simulation proceeds, the variation in convergence speed between the two schemes decreases. After approximately 150 time steps, the convergence rate stabilizes, in which the simulation including the full Jacobian has a 20 % better convergence throughout the computation. Overall, the total computational time was reduced by 22.5 % when including the full Jacobian matrix.

The FSI algorithm was used to perform a numerical simulation of the mitral valve during diastolic filling. In our study, the simulations incorporated the dynamic interaction of blood flow and leaflet motion and an imposed subject-specific, transient LV wall movement. The MV was modeled as two rigid asymmetric leaflets. By appearance the two leaflets resembles artificial heart valves rather than physiological heart valves [84], in particular when it comes to flexibility. Among other factors, some physical restraining mechanisms (e.g. bending moments, clamping moments, moments of inertia) are missing that would help describe the mitral valve opening dynamics properly. The posterior leaflet has the longest attachment zone and is therefore physiologically more constrained than the anterior leaflet, which acts more like a hinge. Due to this, the posterior leaflet will be more influenced by the lack of restraining mechanisms, resulting in higher angular velocities and more extreme opening angles throughout the simulation. Furthermore, a recent study addresses the effect of active muscle fibers on the global response of the mitral valve during systole [103]. Whether these muscles also have an impact on the mitral valve movement during diastole has not yet been addressed. The algorithm presented here would be appropriate to use for bileaflet mechanical heart valves (BMHV), which consists of two separate rigid leaflets without any physical restraining mechanisms.

In the simulations the leaflets' lengths were chosen based on ultrasound images recorded in the apical long-axis view. In this plane, the length distribution is close to 25 % for the posterior and 75 % for the anterior leaflet. However, the total surface area distribution for the natural MV is, due to its shape, close to 38 % for the posterior and 62 % for the anterior leaflet. The mismatch in surface area, between the modeled and natural MV, will alter the simulated opening velocities because the total amount of forces acting on the leaflets' surfaces will differ. Based on the given premises of this study, and the limitations due to the 2D formulation, the opening angle obtained from the ultrasound recordings can not be accurately described by the simulations. However, the simulation results capture the main features of the leaflets' movement pattern.

The results show that during the deceleration of the first filling wave, a vortex is developing behind each leaflet. The vortex observed behind the anterior leaflet is larger and more intense than the vortex behind the posterior leaflet. These observations are consistent with studies that have demonstrated a large vortex behind the anterior leaflet and a smaller vortex behind the posterior leaflet [13, 39, 57, 87, 88]. However, vortices developed at the tip of rigid leaflets would be more intense than vortices resulting from flexible leaflets with ability to follow the flow. In studies only including one mitral leaflet, a large vortex has developed at the tip of this leaflet [77, 106]. By replacing the asymmetric

geometry of the mitral valve with a symmetric valve or one valve only, the vortex structures that develop as the blood flows through the valve and fills the ventricle will be altered. The interaction between the asymmetric leaflets will also be lost. Our results indicate that the asymmetry of the leaflets affects the vortex formation in the LV and therefore we believe that it is essential that both leaflets are present.

In general, the left atrium and its pulmonary veins is commonly neglected when simulating LV filling. In our model, the PV inflows were incorporated in the LA and recirculated in vortices. The vortices increased in size during diastasis, until they were flushed into the ventricle at end-diastole. This is in accordance with the findings of [42], who studied and analyzed the normal left atrial flow pattern in 11 healthy subjects with magnetic resonance imaging (MRI). They observed that vortex formation followed early diastolic filling, and that the vortices reached their maximum diameter in mid-diastole, before they disappeared with atrial contraction. In our simulation we observe that these atrial vortices affect the cross-sectional mitral velocity distribution, hence, they might have an influence on the opening of the leaflets. Thus, further studies are needed to investigate this issue.

During the deceleration of the first filling, the cross-sectional velocity profile at the level of the mitral annulus is skewed, predominantly near the posterior side. This skewed velocity distribution can again be seen with atrial contraction in end-diastole, but this time it is more prominent. A nonuniform cross-sectional mitral velocity distribution during the deceleration of early diastolic filling and atrial systole was also observed by [57] who studied the velocity distribution across the natural mitral valve in pigs with ultrasound. Like in our study, the mitral inflow was predominantly seen at the central and posterior parts of the mitral opening. It is likely that for BMHVs, where each leaflet is allowed to rotate due to interaction with the blood flow, this phenomenon may lead to different opening patterns for the two leaflets, particularly in mid- and end-diastole.

Our results indicate that important features of the flow field may not be predicted in the absence of an adequate model for the LA. This was also the conclusion of [31], who simulated the flow in the human ventricle, however, they did not include the mitral leaflets.

Although, the qualitative flow behavior in our simulation is similar to the observations in [57] and [42], a moving atrium will have a quantitative influence on the flow. The jet flow from the PV's will be weaker during early filling if the LA is moving, because the fluid entering the LV will then mainly come from the blood that was stored in the LA and not from the PV's. If the LA is not moving, a stronger jet occurs, leading to more intense vortices. Another important factor contributing to more intense vortices is the rigid PV orifices. In reality, PV orifices are made up of elastic tissue which would contribute to a softer transition into the LA chamber.

The longitudinal movement of the annulus is included in the simulations, however, the diameter of the annulus is kept fixed. Measurements done in our ultrasound recordings showed that the diameter of the mitral orifice changed with about 13% during diastole, which was in good agreement with published numbers [53, 112]. Fluid injection across an orifice into a larger container can result in the generation of vortex rings if the ratio orifice to cavity diameter is in a certain range. Experiments of [16] showed that if the ratio is smaller than about 0.5, propagation of vortex rings is possible. If the ratio is larger, the vortices will be arrested or not develop. Based on their experiments and an average value of the annulus and ventricular diameter, they concluded that for a normal ventricle the conditions are such that vortices will most likely not be generated. Our recordings, on the other hand, gave a ratio decreasing from 0.62 to 0.44 during diastole. According to this we would expect that a compliant annulus will have an influence on the flow, hence simulations have to be done to verify this. However, the experiments by [16] were stationary, a transient orifice may give other conclusions.

Some the of the features not incorporate in the present study (e.g. the angle of tilt of the fixed LA, a moving LA, a compliant annulus, different locations of the PVs orifices and definitely 3D characteristics) would most likely affect the left atrial flow and hence the valve movement and hemodynamics during diastole.

In this paper an expanding LV with no outlet, was imposed as a boundary condition. We chose to use a subject-specific geometry and prescribed ventricle wall movement based on ultrasound recordings, which enables us to analyze the flow phenomena in a particular subject. The intraventricular flow will be the same whether the same wall motion is prescribed or computed by a coupled solution. Previously, MRI/CT has been used to track and prescribe a transient ventricular wall in both 2D and 3D [31, 63, 69, 70]. In the present paper we showed that speckle tracking may provide subject-specific prescribed wall motions as input for 2D numerical models. As far as we know, ultrasonic speckle tracking has never been utilized for this purpose before. The imaging performed in this study had a temporal resolution of 22ms. Ultrasound may be more accurate for wall tracking since the temporal resolution often is higher than for MRI. However, MRI has a clear advantage with respect to image quality.

In our simulation, a pressure profile was applied at the two PV inlets. However, the flows at the inlets are following the prescribed movement of the LV wall. As long as the motion of the boundaries is prescribed, it does not matter what pressure profile is applied at the inlets as a function of time. This is because there is no time derivative of the pressure in the governing equations. E.g. the use of a constant pressure at the inlets results in exactly the same flow behavior. This has been verified.

In this preliminary study of LV filling, several simplifications have been done. A crucial simplification is the 2D approach. By excluding the potential for 3D vortex instability, the vortex wake will become more persistent and sustain for a longer time. Simulations in 3D are required to capture the evolution of a wake after the formation phase [9]. However, a 2D approach still gives a qualitative description of the vortex formation. The FSI-method presented here also applies to 3D structures.

In conclusion, we have developed an algorithm accounting for mutual interaction between two rigid, asymmetric leaflets in an ALE FSI approach. The inclusion of the full Jacobian matrix significantly enhances the speed of the simulation. Overall, the total computational time was reduces by more than 22,5%. Furthermore, our results indicate that important features of the flow field may not be predicted by the use of symmetric leaflets or in the absence of an adequate model for the LA, particularly during diastasis and atrial contraction.

Acknowledgement

The authors would like to express their gratitude to Professor Hans Torp and PhD Lasse Løvstakken at the Norwegian University of Science and Technology (NTNU) for issues regarding ultrasound measurements and cardiologist Johannes Soma at St. Olavs hospital, Norway, for echocardiographic recordings.

Chapter 7

An assessment of left atrial boundary conditions and the effect of mitral leaflets on left ventricular filling

Parts of the contents in this chapter are based on Dahl et al. (2009), **Implicit interaction of two rigid mitral leaflets in a partitioned fluid-structure approach**, *MekIT'09: Fifth National Conference on Computational Mechanics, Trondheim 26-27 May 2009, Tapir Akademisk Forlag 2009 ISBN 978-82-519-2421-4: p. 135-149.*

7.1 Introduction

A challenge in all areas of computational fluid dynamics (CFD) is the treatment of boundary conditions. An understanding of the actual problem is required in order to apply simplifications that will still provide meaningful results.

Intraventricular flow and mitral valve (MV) dynamics have been subject to research both computationally, in vivo and in vitro. Simulations have been executed with a rather broad variation of realism regarding heart chamber geometry, valve modeling and inlet conditions. Due to the heart's complexity, the left ventricle (LV) is, in most of these studies, isolated from the rest of the heart. The LA and the MV are therefore often excluded. The aim of this study is to investigate how the flow pattern is affected when the LA and MV are accounted for compared to when they are not.

The cardiac cycle is divided into two main phases, this is the diastole, which is the ventricular filling phase, and the systole, which is the ventricular contraction phase. The LA is located prior to the LV and will therefore serve as an inlet conduit for the LV. The LA's function during a cycle can be divided into three phases: the reservoir, conduit and contraction phase. The reservoir phase is during systole when the LA receives oxygenated blood from the lungs through its pulmonary veins (PVs) and acts like a reservoir to the LV. The conduit phase is the passive emptying of the atrium due to ventricular relaxation in early diastole. The contraction phase occurs at the end of diastole when the LA contracts to re-increase the pressure and eject more blood into the ventricle. According to Fyrenius *et al.* [42], the normal LA has important roles in optimizing left ventricular filling. In vivo measurements indicate that vortices develop in LA during diastole before they disappear with atrial contraction. During the last decades, relatively few studies have concentrated about flow dynamics in the left atrium [42, 55, 109], hence, the understanding of the global flow pattern within the LA has remained undefined [42].

When the atrium is excluded from the model, the mitral inlet properties, which normally are a result of the flow development inside the LA, have to be replaced by alternative inlet conditions. A uniform pressure condition or some symmetric velocity profile are of the most common assumptions. The inlet is, in some studies, imposed directly at the mitral opening [8, 9, 32, 33, 39, 50, 63, 69, 74, 81, 93], while in other papers the atrial geometry has been represented as some tube with the inlet at the far end [7, 20, 36, 39, 77, 78, 91, 94, 98, 106, 114, 117]. Mihalef *et al.* [70] included a subject-specific LA with four venous inflows and a simplified prescribed leaflet motion. The group of Oertel included an atrium with two PVs, but no leaflets [31, 60, 104].

Long *et al.* [63] imposed various computed inflow profiles directly at the MV opening and concluded that CFD simulations of LV flow are highly sensitive to the imposed boundary conditions during diastolic filling. Schenkel *et al.* [98] investigated the sensitivity to inflow conditions by comparing a curved and a straight atrial geometry having one inlet covering the whole end. They concluded that the atrial geometry plays a major role in the development of intraventricular flow dynamics. None of these studies included the mitral leaflets. Samstad *et al.* [96] investigated the early mitral inflow in one plane in patients with mitral reguritation and with mitral stenosis using two-dimensional color Doppler ultrasound. Their data suggested that the early mitral flow was variably skewed in both patient groups. Kim *et al.* [57], was the first to investigate the entire cross-sectional mitral inflow velocity distribution by echocardiographic recordings in pigs. Their results showed that the inflow velocity across the mitral orifice is not uniformly distributed throughout diastole, but is variably skewed. These observations disagree with the common assumption of an imposed symmetric inlet profile and emphasize the need of further investigations regarding inlet configurations.

The MV separates the LA and LV and controls the blood flow between the two chambers. The valve has two leaflets with significantly different geometries and motion. As for the atrium, there are several approaches regarding MV modeling in simulations of LV filling. One approach neglects the mitral leaflets and the leaflet-blood interplay will then be lost and consequently also the effect the mitral leaflets could have on the flow [7–9, 21, 31–33, 60, 63, 69, 74, 93, 94, 98, 104, 115]. Another approach includes the leaflets by using a simplified prescribed leaflet motion, here the complex phenomena of blood-leaflet interaction are avoided [70, 91]. A third method is to include full FSI of the blood and the leaflets [3, 20, 27, 36, 39, 77, 78, 106, 114, 117]. To what degree the leaflets influence the intraventricular flow is a matter of discussion in literature.

The objective of this study was first to investigate the diastolic flow pattern and MV opening dynamics when the mitral inflow profile was allowed to develop inside a geometrical realistic 2D representation of the atrium with two flow inlets to render the venous inflows, and compare with results from a model with a simplified atrium. Second, to observe what effect the mitral leaflets may have on the intraventricular flow by simulating the diastole with and without flow driven leaflets. The study is two dimensional and the results are aimed to show, qualitatively, the changes in flow pattern when structures like the MV or the LA are excluded or not. To the best of our knowledge no study of LV filling has incorporated both an atrium with venous inflows and flow driven mitral leaflets.

Echocardiographic recordings were utilized to obtain subject-specific ventricular wall movement and the atrial geometry. The subject-specific LV movement was imposed as a boundary condition in a 2D transient simulation of diastolic filling. The leaflets were simulated with an asymmetric geometry and their motion was computed using a previously developed FSI coupling scheme where both leaflets are allowed to move asynchronously [3, 27].

7.2 Models and methods

7.2.1 Geometrical model

To investigate the influence of the inlet configuration on LV filling and MV dynamics, two 2D models, c_I and c_{II}, were considered. In c_I, the inflow region was rendered as a stiff tube having an inlet at the far end, whereas for c_{II}, the inflow region was represented by a typical, but fixed, atrium with two inlets in the upper part, each reflecting an orifice of a pulmonary vein. Flow driven mitral leaflets were included in both models.

To observe which changes that occurred in the flow field when excluding the mitral leaflets, a third model, c_{III}, was created. This model was identical to c_{II}, but without the leaflets.

Echocardiographic recordings of a young healthy adult were utilized to create the subject-specific 2D models. The long-axis plane of the ventricle was chosen because the aortic outflow, the mitral inflow, the left ventricle and the left atrium are all visible in this view. The recordings had a temporal resolution of $20ms$ resulting in a total of 20 time frames throughout diastole. The inner ventricular geometry and its diastolic movement were extracted from the image data. The size and shape of the fixed LA geometry were rendered in the mid-diastolic period. The geometry of the ventricle at start and end diastole are shown in Fig. 7.1. More details about the prescribed movement can be found in [27].

The mitral leaflets were modeled as two asymmetric, rigid leaflets rotating around their annulus attachment points. The lengths of the leaflets were chosen based on echocardiographic images from

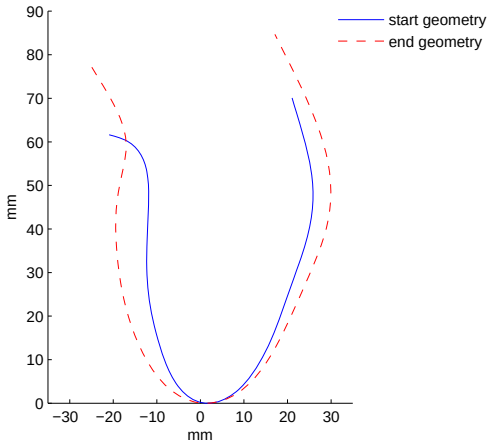

Figure 7.1: Geometry of the left ventricle at start and end diastole, extracted from echocardiographic recordings in the ventricular long axis plane

the apical long-axis view. In this plane, the length distribution is close to 25 % for the posterior and 75 % for the anterior leaflet. The thickness was set to be uniformly $t = 1.0\ mm$ for both leaflets.

7.2.2 Fluid structure interaction method

The FSI problem was solved in a partitioned way with separate solvers for the flow equations (Fluent 6.3.26, Ansys Inc.) and the structural equations (in-house code).

The problem has two degrees of freedom, one for each leaflet. The equation of motion can be written as: $\mathbf{M} = \mathbf{I} \cdot \ddot{\boldsymbol{\theta}}$, where $\mathbf{M}$ is the torque applied on the leaflet's external surface by the pressure and the viscous force, $\mathbf{I}$ the moments of inertia and $\ddot{\boldsymbol{\theta}}$ is the angular acceleration of the leaflets. This can be written in matrix notation where the component for the anterior and posterior leaflet is given by subindex 1 and 2, respectively:

$$\begin{bmatrix} M_1 \\ M_2 \end{bmatrix} = \begin{bmatrix} I_1 & 0 \\ 0 & I_2 \end{bmatrix} \cdot \begin{bmatrix} \ddot{\theta}_1 \\ \ddot{\theta}_2 \end{bmatrix} \tag{7.1}$$

The FSI formulation is based on the ALE approach and utilizes a previous developed, fully implicit, coupling algorithm, which allows asynchronous motion of the two leaflets. An accurate description of the coupling scheme can be found in [3, 27] and is an extension of the coupling scheme for one leaflet developed in Vierendeels *et al.* [116] and validated in Dumont *et al.* [35].

The blood was treated as an incompressible, Newtonian fluid, with properties representative for healthy human blood, a density of ρ = 1056 kg/m^3 and a dynamic viscosity of μ = $3.5 \cdot 10^{-3}$ kg/ms [20]. Laminar flow was assumed.

The dependence of the results on the time step has been analyzed. The results do no longer change significantly when the physical time step is reduced from 0.2ms to 0.1ms. The diastole (0.43s) was thus discretized with 2150 time steps.

7.2.3 Boundary and initial conditions

The prescribed motion of the ventricular wall was implemented in the flow solver through a user-defined function (UDF). A no-slip condition was imposed on the walls. Since the aortic valve is closed during ventricular filling, no LV outlet was defined. The mitral leaflets were initially in their closed positions.

The venous inlets were treated as passive pressure inlets as LV expansion will drive the flow in all three cases.

7.3 Results

7.3.1 c_I versus c_{II}

Fig. 7.2 and 7.3 shows the initial grid and seven sequential velocity-vector plots at time intervals of 60 ms for the two configurations c_I and c_{II}, respectively. The prescribed motion of the LV during filling can be seen as time progresses. It is evident that variations in shape and volume occur during diastole.

Mitral inflow profile

In early diastole, during the acceleration phase of the first filling, also called the E-wave, ((b)-(c)), the velocity profile across the mitral valve is almost uniform for both c_I and c_{II}. The velocity magnitude is almost the same for the two configurations at the level of the mitral annulus. In the deceleration phase of the E-wave, (d), the flow is retarding and the velocity distribution across the MV becomes variably skewed for c_{II}, the blood is predominantly flowing near the posterior side of the annulus. In c_I, the velocity distribution is still approximately uniform. The two subsequent plots, ((e)-(f)), represent the partial closure of the leaflets in the mid-diastolic period. The transmitral flow is now almost zero for both c_I and c_{II}.

At the end of diastasis, ((g)-(h)), the atrium contracts, causing a second filling wave (A-wave) into the ventricle. A prominent asymmetric mitral inflow with a high velocity at the posterior side can be observed in c_{II}. The velocity distribution in c_I, is still almost uniform. At the very end of diastole, the flow is retarding and the leaflets start to drift back.

LV flow field

The observed ventricular flow pattern does not deviate considerably between the two configurations during the first filling, however the inflow penetrates somewhat further into the mid-cavity in c_{II}. At this time, no vortices are observed in the ventricle. During the deceleration of the E-wave, (d), a vortex starts to develop at the tip of each leaflet in both configurations. The clockwise vortex developing behind the anterior leaflet is, in both c_I and c_{II}, larger and more intense then the counterclockwise vortex behind the posterior leaflet. These vortices probably enhance the partial closure seen in mid-diastole.

During the second filling wave, vortices developed in the atrium are flushed into the ventricle in c_{II}. Since no atrial vortices are present in c_I, this phenomenon does not occur and the blood flows more uniformly into the ventricle.

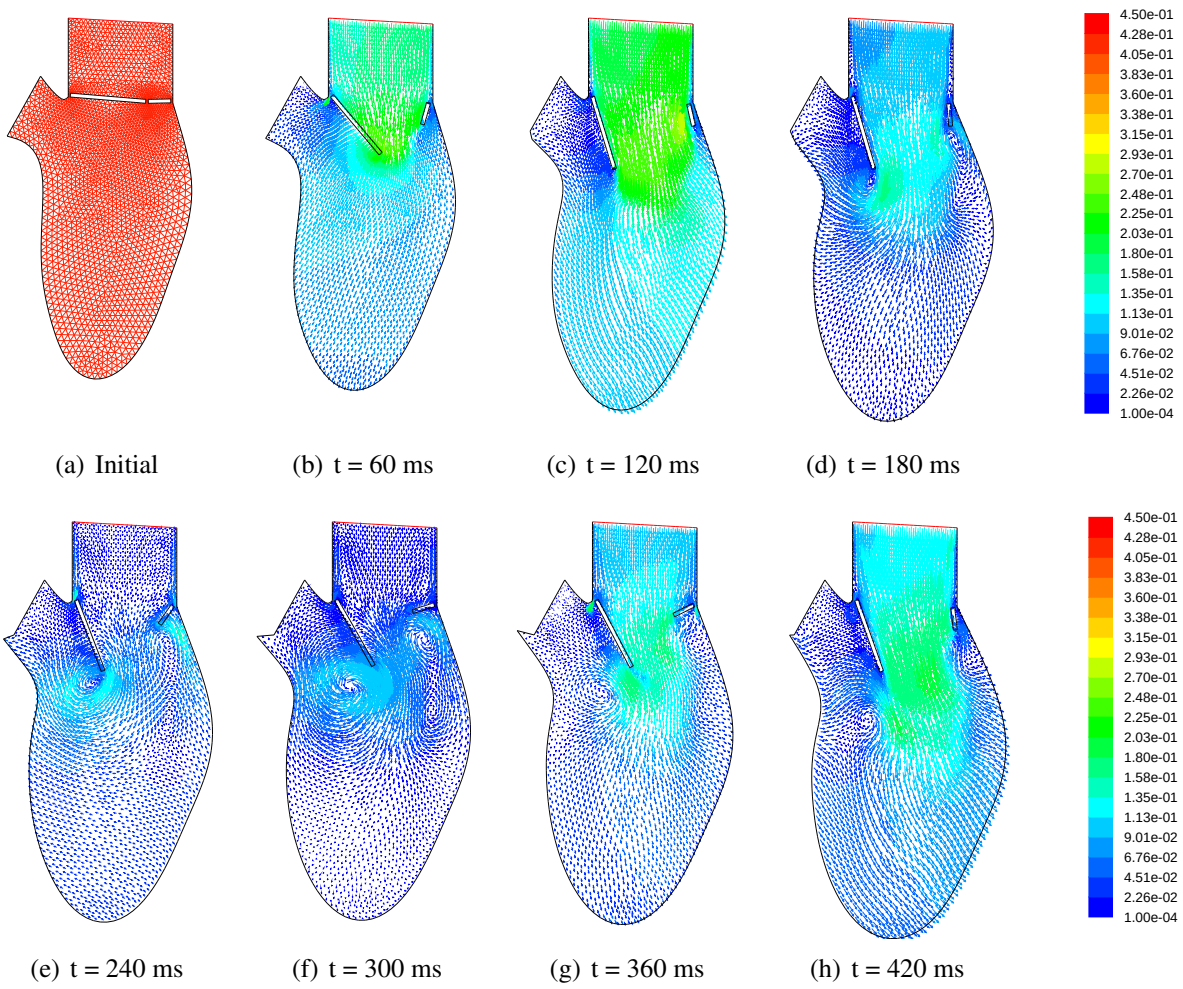

(a) Initial (b) t = 60 ms (c) t = 120 ms (d) t = 180 ms

(e) t = 240 ms (f) t = 300 ms (g) t = 360 ms (h) t = 420 ms

Figure 7.2: Initial grid and velocity vectors at seven different times for c_I during diastole, the velocity scale to the right is given in $[m/s]$

LA flow field

During the first filling phase, a vortex starts to develop at each PV orifice in c_{II}. The vortices increase in size during mid-diastole until they are flushed through the MV opening at atrial contraction (A-wave). Throughout diastole, no vortex was observed in the inlet geometry of c_I.

MV opening dynamics

The fluid forces acting on the leaflets are different for the two cases, hence, the resulting opening dynamics will differ. Fig. 7.4 shows the opening angle for both leaflets in c_I and c_{II}, compared with the leaflets' opening angle measured in the 2D echocardiographic recordings. The simulated opening velocities is almost identical during the first rapid filling for both leaflets. However, only the anterior leaflet corresponds to the measured opening velocity. In mid- and end-diastole, the leaflets' opening angles deviate some between the two simulations, particularly for the posterior leaflet where the most extreme angle is found in c_I. The partial closing occurred later in the simulations then in the measurement, but the simulations do capture the main features of the leaflets movement pattern.

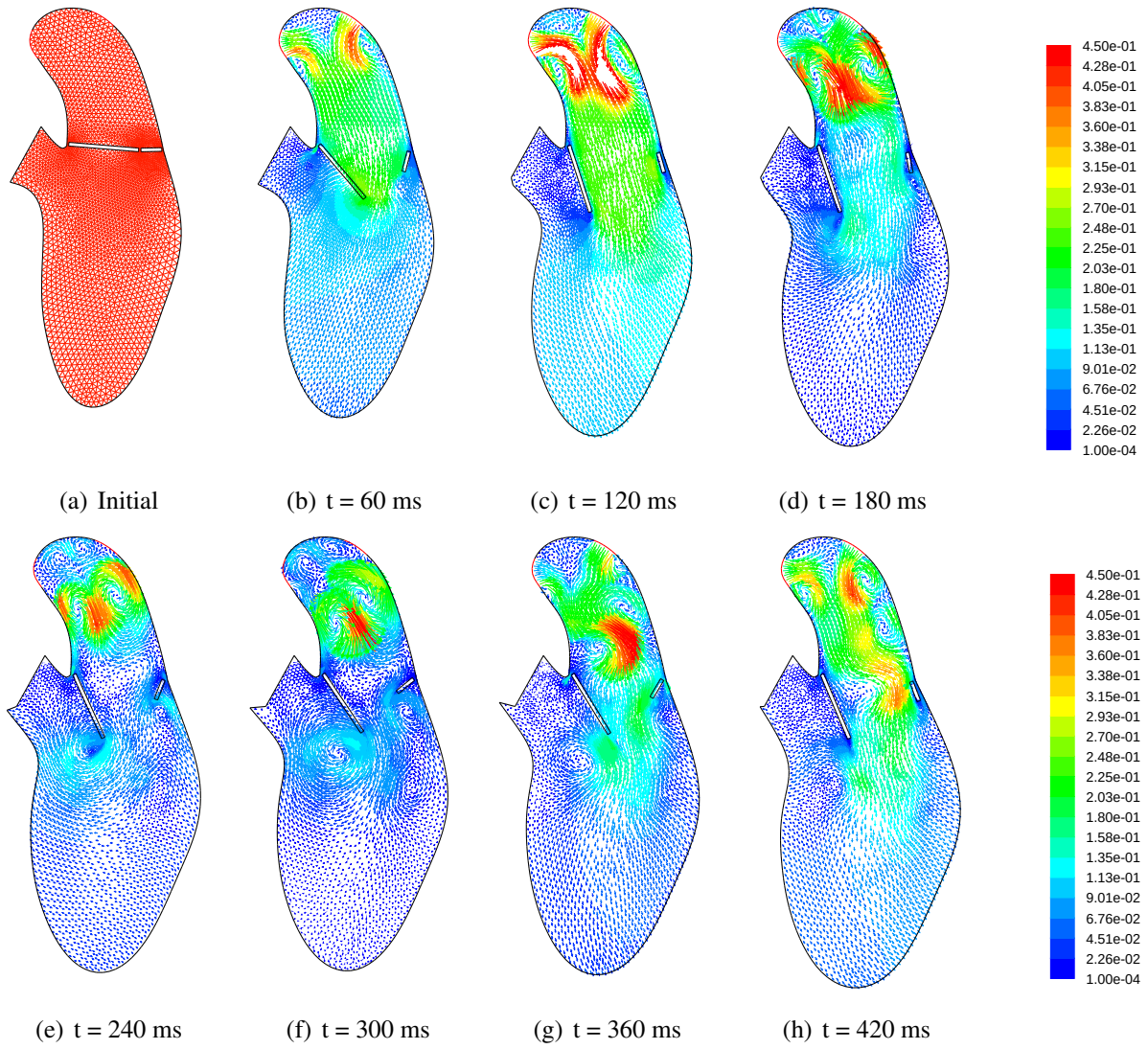

(a) Initial (b) t = 60 ms (c) t = 120 ms (d) t = 180 ms

(e) t = 240 ms (f) t = 300 ms (g) t = 360 ms (h) t = 420 ms

Figure 7.3: Initial grid and velocity vectors at seven different times for c_{II} during diastole, the velocity scale to the right is given in $[m/s]$

7.3.2 c_{II} versus c_{III}

Fig. 7.5, shows the initial grid and seven sequential velocity-vector plots at time intervals of 60 ms for c_{III}. The flow pattern across the mitral annulus is skewed as in c_{II}, hence, the leaflets' absence do not seem to affect the velocity profile particularly at this level. However, the leaflets significantly change the flow field below the annulus. In c_{II}, the mitral inflow is guided into the ventricle by the leaflets where two vortices develop at the leaflets' tips. In c_{III}, the fluid expand into the ventricle. When fluid flows into a cavity with a larger diameter vortices tend to develop if the ratio between the opening and the cavity is within a certain range. For c_{III} we can observe a vortex developing in the left ventricular outflow tract, as there is no leaflet present to prevent it. At the posterior side, no vortices are observed. When the flow in the mitral opening stagnates during diastasis, there is almost no rotational flow inside the LV for c_{III}.

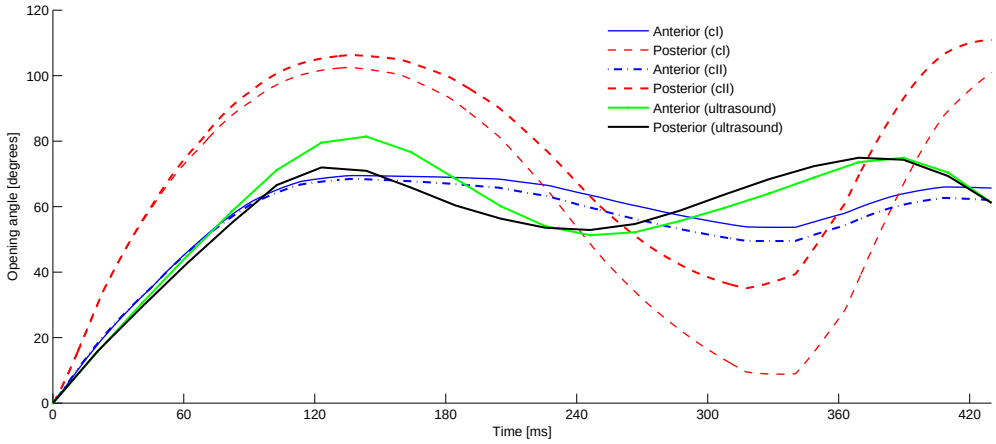

Figure 7.4: Opening angle versus time for both leaflets in c_I and c_{II}, compared with the leaflets' opening angle measured in 2D echocardiographic recordings

7.4 Discussion

7.4.1 Sensitivity to inlet geometry

In general, the left atrium and its pulmonary veins are commonly neglected for simulations of ventricular filling and mitral valve motion. As the current knowledge of the mitral velocity distribution is sparse, the imposed inlet profile is often approximated to a uniform pressure condition or some symmetric velocity profile across the mitral annulus. Our results indicate that atrial vortices will be generated if a more physiological representation for the atrium with venous inflows are included. The vortices will induce a nonuniform velocity profile across the mitral opening, which in turn, influence the leaflets dynamics and intraventricular flow pattern.

In c_{II}, atrial vortices are observed during diastole. The vortices start to develop at each PV orifice during early filling phase. The vortices increase in size during diastasis, before they are flushed into the ventricle at atrial contraction. The same atrial flow behavior was observed by [42] who investigated the normal left atrial flow pattern in 11 healthy subjects. They observed that vortex formation followed early diastolic filling. Further, they found that the vortices reached their maximum diameter in mid-diastole, before they disappeared with atrial contraction.

In c_{II}, we observe that these atrial vortices affect the cross-sectional velocity distribution both at the level of the mitral annulus and the leaflet tips. During the deceleration of the early filling wave, the cross-sectional velocity profile at the level of the mitral annulus is skewed, predominantly near the posterior side. This skewed velocity distribution can again be seen with atrial contraction in end-diastole, but this time it is more prominent. This is in accordance with the findings of Kim *et al.* [57], who studied the velocity distribution across the natural mitral valve in pigs with ultrasound. They observed a nonuniform cross-sectional mitral velocity distribution during the deceleration of early diastolic filling and at atrial contraction. In c_I, no vortices were observed in the inlet geometry and the inflow velocity was approximately uniformly distributed across the mitral opening and at the leaflet tips.

Kim *et al.* [57] suggested that the nonuniform blood flow distribution across the mitral opening is caused by the development of an anterior vortex in the LV during the deceleration of early filling and

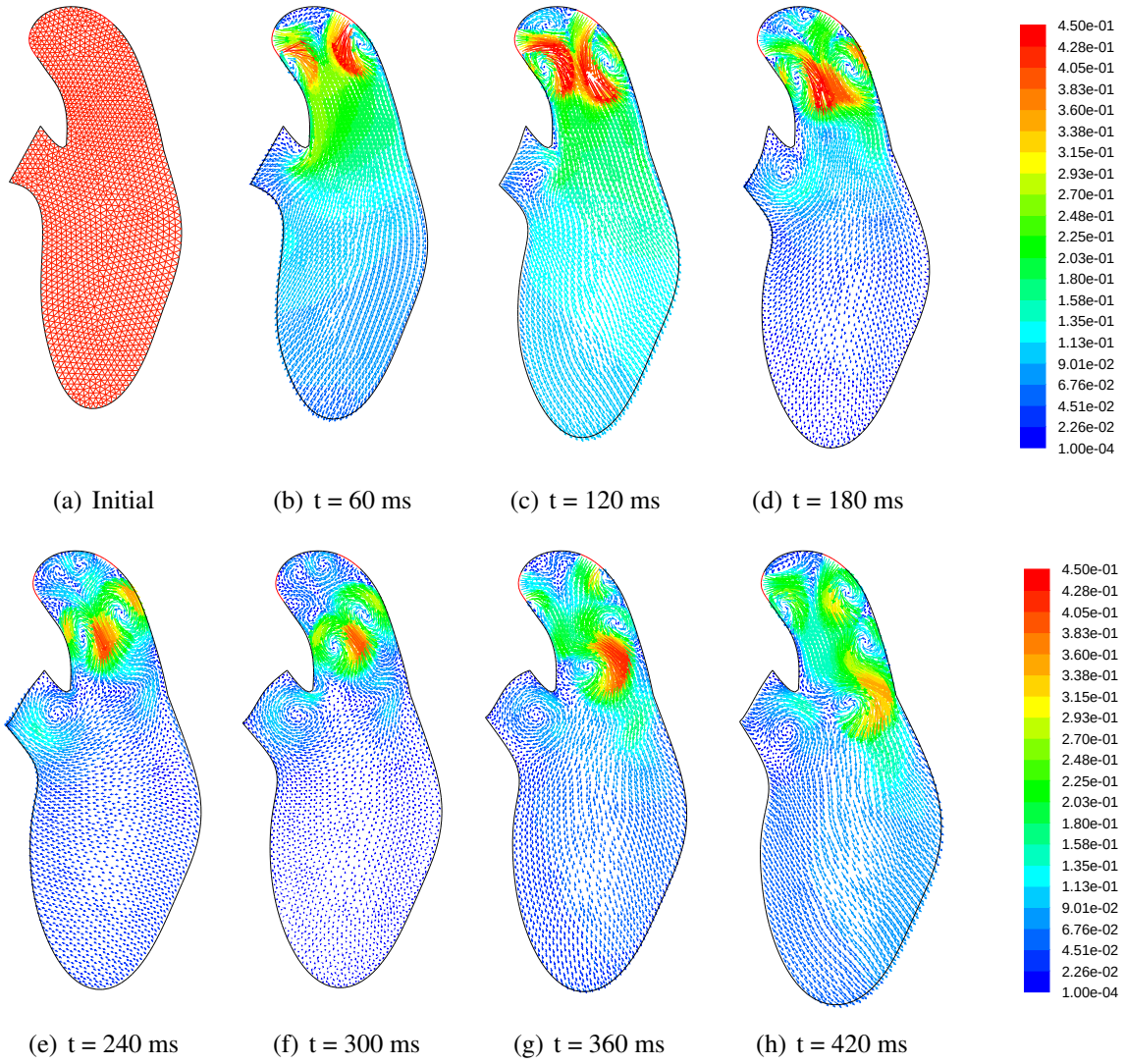

(a) Initial (b) t = 60 ms (c) t = 120 ms (d) t = 180 ms

(e) t = 240 ms (f) t = 300 ms (g) t = 360 ms (h) t = 420 ms

Figure 7.5: Initial grid and velocity vectors at seven different times for c_{III} during diastole, the velocity scale to the right is given in $[m/s]$

atrial systole. Based on our simulations, we suggest that the nonuniform flow distribution mainly is caused by atrial vortices. In c_I, the velocity profile is approximately symmetric, even if an anterior vortex has developed at the leaflet's tip. In c_{III}, where no leaflets are present, a skewed profile can still be observed, but the profile is somewhat altered compared to c_{II}. This indicates that while the left atrium and its associated venous inflows cause the nonuniform velocity distribution, the leaflets presence will slightly alter the velocity profile at the level of the mitral orifice.

Although, the qualitative atrial flow behavior in c_{II} is similar to in vivo observations [42, 57], a moving atrium will have a quantitative influence on the flow. The jet flow from the PV's will during early filling be weaker if the LA is moving, because the fluid entering the LV will then mainly come from the blood that was stored in the LA and not from the PV's. If the LA is not moving, stronger PV jets occur, leading to more intense vortices. The rigid PV orifices in our model is also contributing to more intense vortices, for a compliant orifice, the vortices will be less intense.

We believe that interindividual differences in the mitral inflow will occur, among other factors, due to variations in atrial geometry, shape of the mitral orifice, the viscosity of the blood, the velocity of the inflows and particularly due to the number and locations of the PVs. Further studies are needed to investigate the sensitivity to variations in the venous inflows.

The mitral leaflets opening dynamics were affected by the inlet configuration. After the first rapid filling the opening velocity started to diverge between the two cases. Where the opening of the posterior leaflet differed the most. The best agreement between measured and simulated opening dynamics was found in c_{II}, however the partial closing occurred later in the simulation and the opening angle of the posterior leaflet was too extreme. Some physical restraining mechanisms are missing that would help describe the MV opening dynamics properly. The posterior leaflet has the longest attachment zone and is physiologically more constrained than the anterior leaflet, which acts more like a hinge. Our posterior leaflet model will consequently be more influenced by the lack of restraining mechanisms, resulting in higher angular velocities and more extreme opening angles throughout the simulation. On the basis of the given premises of this study, and the limitations due to the 2D formulation, the opening angle obtained from the ultrasound recordings cannot be accurately described by the simulations. However, the simulation results capture the main features of the leaflets movement pattern.

For bileaflet mechanical heart valves (BMHV), where each leaflet is allowed to rotate independently due to interaction with the blood flow, a skewed inlet profile may lead to different opening patterns for the two leaflets. A correct velocity distribution across the mitral opening will therefore be essential to capture this phenomenon. Also, an algorithm which allows asynchronous motion of the two leaflets is needed [3, 27].

7.4.2 The leaflets' influence on the intraventricular flow

To what degree the leaflets affect the intraventricular flow pattern is a matter of controversy in literature. In both c_I and c_{II}, a vortex starts developing at the tip of each leaflet during the deceleration of the E-wave. These observations are consistent with studies that have demonstrated a large vortex behind the anterior leaflet and a smaller vortex behind the posterior leaflet [13, 39, 57, 87, 88]. The leaflets are rigid in our study, for flexible leaflets the vortices will not have the same intensity. Mihalef *et al.* [70], modeled 3D valve leaflets having a simplified prescribed motion, they observed a main vortex ring right below the mitral valve shooting towards the apex. Physiological leaflets are very flexible and will probably align more with the flow, however they still form an inflow tract which will guide the inflow further into the ventricular cavity before vortices are formed. During filling, the anterior leaflet is more or less blocking the outflow tract and prevents vortices from being formed in this area, as seen in c_{II}. If leaflets are not present, the flow will spread out further up in the LV base, as in c_{III}, where a large vortex develops in the aortic outflow tract.

In valveless ventricles the most observed phenomenon is the formation of an annular vortex ring behind the mitral orifice. How far into the ventricle the vortex ring penetrates depend, among other factors, on the ratio of mitral inlet to ventricular radius. Fluid injection across an orifice into a larger container can result in the generation of vortex rings if the ratio of orifice to cavity diameter is in a certain range [16, 101]. The ratio of mitral inlet to ventricular radius will therefore play an important role in the forming and propagation of vortices during LV filling, especially when no leaflets are present. Experiments of Bot *et al.* [16] showed that if the ratio is smaller than about 0.5, propagation of vortex rings is possible. If the ratio is larger then 0.6, the vortices will be arrested or not develop.

In Shortland *et al.* [101], vortices developed for larger inlet-to-ventricular-radius ratios than in Bot's work (0.85 opposed to 0.6). A possibly explanation is that Shortland *et al.* [101] used a moving ventricular wall that encouraged radial flow velocities and hence vorticity during filling. No leaflets were included in the experimental models. In c_{III}, the ratio was within the range of vortex formation at the anterior side, however, the vortex did not penetrate further into the ventricular cavity. In several numerical studies, the valve is modeled as a 2D projection into the mitral plane, the ratio will then change significantly during diastole and will, at least in parts of the filling, be within the range of vortex formation. In the beginning of diastole the vortex ring will be bounded by the incoming jet and the wall of the ventricle. When the flow decreases, the vortex will no longer be bounded by the jet and more fluid will entrain into the vortex. In studies with asymmetric ventricular geometry and a laterally displaced mitral orifice, the ring vortex will grow asymmetrically. The development of vortices in models without leaflets will also be affected of the imposed inflow condition [16, 63] and the atrial geometry [31, 98, 104].

So far, this is the only study comparing the ventricular flow pattern with and without leaflets. The study is two dimensional with rigid leaflets and has its shortcomings, but qualitative information may be extracted. Our simulations indicate that the leaflets play a major role in the development of the flow field inside the ventricle. To fully understand the influence of the leaflets, this study should be extended to 3D.

7.4.3 Conclusions

In conclusion, our results indicate that important features of the diastolic flow field may not be predicted in the absence of an adequate representation of the LA or of the mitral leaflets. As it is difficult to measure the blood flow velocities in the beating heart, the current knowledge of the mitral velocity profile is sparse. We therefore suggest that a realistic representation of the atrium and venous inflows should be included in simulations of LV filling dynamics. The leaflets' impact on the intraventricular flow is significant in our study. Whether this is the case in a real ventricle with flexible leaflets have to be investigated further.

Chapter 8

Impact of pulmonary venous locations on the intra-atrial flow and mitral plane velocity profile

Impact of pulmonary venous locations on the intra-atrial flow and mitral plane velocity profile
S. K. Dahl, E. Thomassen, L. R. Hellevik and B. Skallerud
Submitted 2011

8.1 Introduction

The left atrium (LA) is the upper left chamber of the heart and connected to the left ventricle (LV) via the mitral valve (MV). Intraventricular flow has been widely investigated the last decades both in vivo, in vitro and by computational fluid dynamics (CFD). Relatively few studies have focused on the normal flow distribution inside the left atrium [42, 55, 100, 109, 110, 120].

Kilner *et al.* [55] and Fyrenius *et al.* [42] made use of in vivo magnetic resonance imaging (MRI) to visualize the flow across the pulmonary veins (PVs) and within the LA. They discovered that a portion of the normal LA was occupied by organized vorticial flow. To validate in vitro the observations of Kilner *et al.* [55] and Fyrenius *et al.* [42], Tanne *et al.* [109, 110] used a pulsed mock circulatory system to explore the flow dynamics in a realistic anatomical-shaped LA by particle image velocimetry (PIV). By this, they confirmed the asymmetries in the atrial flow already observed in vivo.

The atrium is far from being a passive transport chamber prior to the LV [14]. The relationship between the two chambers can be characterized as highly interactive and dynamic. According to Fyrenius *et al.* [42], the normal LA has important roles in optimizing left ventricular filling. Due to the complexity of the heart, the LV is often isolated in simulations regarding LV filling. The most common simplification is to replace the atrial cavity with an approximated inlet condition imposed directly at the mitral opening or at the end of some tube. Due to difficulties in measuring blood flow velocities in vivo, the current knowledge of the cross sectional mitral velocity distribution is sparse. Domenichini & Pedrizzetti [32] declared that at the present state of knowledge, it is not immediate to ensure a realistic modeling of the transmitral flow. The imposed MV inlet profile is therefore normally simplified to a uniform pressure condition or some symmetric velocity profile.

Kim *et al.* [57], was the first to investigate the entire cross-sectional mitral velocity distribution by echocardiographic recordings in pigs with no known heart disease. Their results showed that the velocity distribution across the mitral opening was variably skewed and that it was large interindividual discrepancies. These observations disagree with the common assumption of a symmetric mitral inlet condition. One approach to avoid the problem of prescribed MV inlet profiles, is to include an atrium with venous inlets and let the flow develop inside the chamber before it enters the mitral plane. This has been done in a few studies. The group of Oertel modeled a fixed, generic atrium with two PVs [31, 60, 104], whereas Mihalef *et al.* [71] included a subject-specific LA with four venous inflows.

The typical PV pattern consists of four main veins, with four separate ostia entering the atrium. The veins from the right lung enters the right (septal) side of the LA, whereas the veins from the left lung enters the left (lateral) side of the LA. Normally, there are two right and two left PVs, but, the interpatient variability in PV number and branching patterns are large [17, 54, 67].

In this study, we present 3D CFD simulations focusing on the intra-atrial flow during LV diastole. The 3D geometries were obtained from Magnetic Resonance Imaging (MRI) recordings of a young healthy adult. The aim was first to investigate the flow field in an anatomically representative model of the LA during diastole. Second, to investigate the effect of PV entry locations on the intra-atrial flow field and the resulting velocity distribution at the mitral plane. The main focus here will be on the mitral plane velocity distribution to see whether this should be considered as an important factor in CFD simulations of LV filling and MV opening dynamics.

8.2 Method

8.2.1 Magnetic Resonance Imaging and flux measurements

MRI recordings of the LA and each of the pulmonary vessel stubs was acquired from a 25-year-old healthy male on a Siemens Avanto 1,5 T system. A temporal resolution of 26ms was achieved, resulting in 40 frames during one cardiac cycle. Images were acquired in the four-chamber and the short-axis orientation. A total of 14 slices with a slice thickness of 5mm were needed in both orientations to cover the atrium and the mitral plane.

In-vivo measurements of the flow velocity through the mitral orifice and the mass flow rate through each of the venous inlets were performed by velocity phase mapping scans.

8.2.2 Segmentation and geometrical reconstruction

The MR images were analyzed using the freely available software Segment v1.8 R1172 [48]. The anatomical geometry of the atrium was reconstructed using the automatic segmentation tool to outline the endocardial border in the short-axis view. By combining both image stacks (short-axis and four chamber view), the proposed contour in every short-axis slice was evaluated using the intersection points to the four chamber view. If necessary, the contours were refined using the manual dynamic contour editing tool.

The MRI showed that the subject had the typical PV pattern consisting of four main PVs with four separate ostia. The location and inlet angle of each PV relative to the LA, were determined with a fairly good accuracy. The veins are denoted left or right according to their position relative to the center of the body, and superior (upper) or inferior (lower) according to their distance from the head. Hence, the name of the four common PVs are the right superior PV (RSPV), left superior PV (LSPV), right inferior PV (RIPV) and left inferior PV (LIPV). The orifice of each PV was reconstructed by measuring the major and minor diameter of each vein in their respective MR scan (see Table 8.1). The measured values fall within clinical reported data [54, 67]. Fig. 8.1 shows an elliptic PV orifice, the two lines indicate the minor and major diameters.

	LSPV	LIPV	RSPV	RIPV
Minor diameter $[mm]$	11.9	10.6	12.1	16.1
Major diameter $[mm]$	15.4	15.8	17.0	16.1
Area $[mm^2]$	113.8	131.2	156.4	203.1

Table 8.1: Diameters and areas of PVs extracted from MRI scans.

The segmentation data was used to build a subject-specific atrial geometry. The first model, denoted c_A, has its four PVs located in the anatomically correct positions as adopted from the MR recordings. The geometry of c_A is shown in Fig. 8.2(a,b). There is a close proximity between the ostia of the right PVs (RPVs) and between the ostia of the left PVs (LPVs), this is in accordance with findings in the literature [17, 54, 67]. In general, and also in our subject, the entry locations of the LPVs are closer to the mitral plane than the RPVs (8.2(a)). The LA appendage (LAA) lies adjacent to the ostium of the LSPV and is indicated with an arrow in 8.2(b).

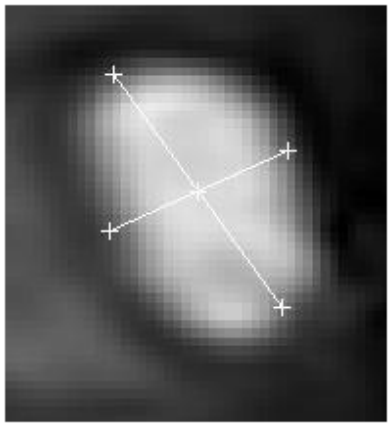

Figure 8.1: A MR image showing an elliptic PV orifice, the two lines indicate the minor and major diameters.

In order to examine the impact of the venous entry locations, two additional models were constructed; c_B and c_C. There are several possible entry locations for the PVs. We chose to keep the angle fixed between the PV trunks, as seen from an atrial view, while the PVs vertical distance to the MV plane were modified. The geometry of the atrial chambers were identical with c_A. Regarding the distance between the veins and the MV, only studies on "The Isthmus Line" were found. The Isthmus Line is the distance between the lower border of the LIPV ostium and mitral annulus. Schmidt *et al.* [99] measured this line to be $28.5 \pm 6mm$ (range 17.3 - 40.5 mm), whereas Wittkampf *et al.* [119] found a mean value of $35 \pm 7mm$ (range 23 - 50 mm). The two studies illustrate the wide dispersion among subjects. In our subject this line was measured to be $30mm$. Based on the findings in the literature and in our subject we chose the following: In c_B, the LPVs are moved up to the same level as the RPVs, the isthmus line is then in accordance with the maximum distance measured in Schmidt *et al.* [99]. We assume the interpatient variability also applies for the RPVs, and thus in c_C the RPVs were therefore moved down and located at the same vertical position as the LPVs in c_A. The geometry of c_A, is shown in Fig.8.2(a,b), whereas (c) and (d), show c_B and c_C, respectively.

8.2.3 Numerical method

The flow simulations were performed using the finite volume method as implemented in Ansys Fluent 13.0 (Ansys Inc.). The diastolic duration was measured to be $0.665s$ and the simulation time step size was set to $0.5ms$. The models were meshed with tetrahedral elements with an element size determined from grid convergence tests. Laminar flow was assumed and the blood was modeled as an incompressible, Newtonian, homogeneous fluid, with a density of ρ = 1050 kg/m^3 and a viscosity of $3.5 \cdot 10^{-3}$ kg/ms, which is a reasonably good approximation for blood flow in large cavities [61].

8.2.4 Boundary conditions

The unique mass flow rate for each of the four PVs was measured using MR phase mapping scans. The measured PV flows correlate with results reported from in vivo studies. For every vein, a power function was fitted to the diastolic mass flow rate as can be seen in Fig. 8.3. The flow pattern is similar for the four PVs, but the mass flow rate differs, where the LSPV has the lowest inflow rate.

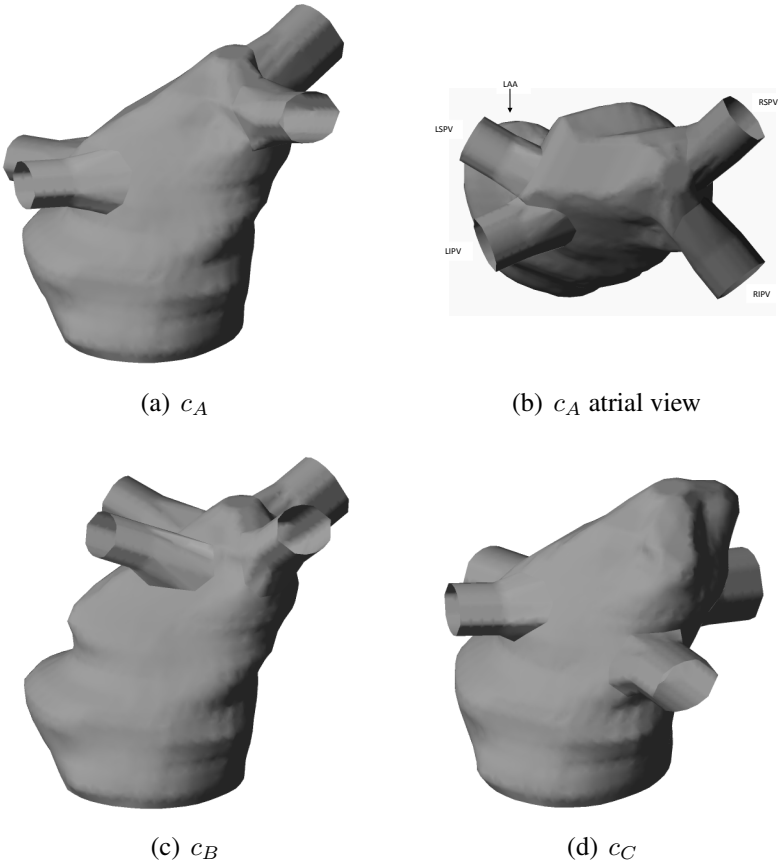

(a) c_A (b) c_A atrial view

(c) c_B (d) c_C

Figure 8.2: The figure shows the geometry of c_A from an inferior,(a), and atrial view,(b), whereas c_B and c_C are shown in (c) and (d), respectively. The name of the four veins and the location of the LAA are indicated in (b).

The atrium was kept fixed during the simulation. However, the measured venous mass flow rates do not account for the extra mass flow exiting the atrium due to atrial contraction throughout diastole. The additional flow due to atrial volume change was calculated from the segmented atrial geometry and evenly distributed among the four venous flow inlets. The change in atrial volume during diastole is illustrated in Fig. 8.4. A no-slip condition was imposed at the walls.

8.3 Results

8.3.1 Normal intra-atrial flow pattern

The intra-atrial flow field is characterized by four jets entering the atrial chamber. During the acceleration of the first filling (E-wave) the inflowing jets are deflected by each other before they progress directly towards the mitral plane. As time progresses, some recirculation occurs. Fig. 8.5 illustrates the streamlines for each PV and the velocity distribution at the mitral orifice at $t = 100ms$, relative to start diastole. We chose to present the flow field by streamlines. Streamlines provide an instantaneous image of the flow field by using information from a single time frame and must not be confused with pathlines. The RIPV, fig. 8.5(a), enters the LA near its septal side and the streamlines follows the

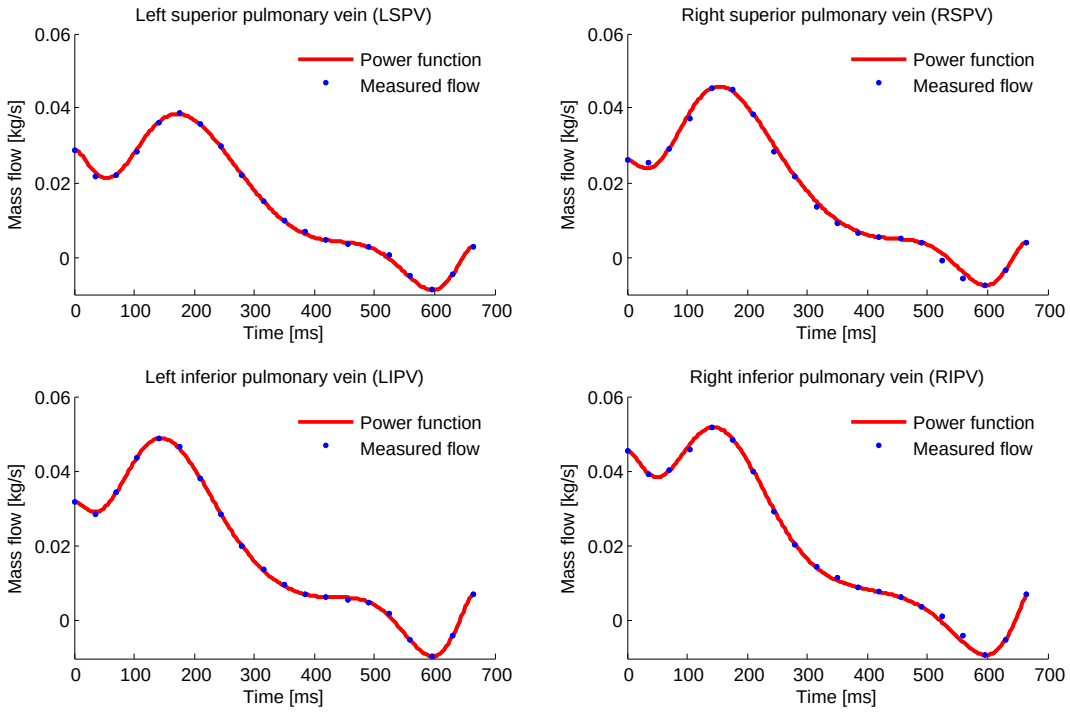

Figure 8.3: The power function (solid line) was fitted to the mass flow rate measured by MR velocity phase mapping (dotted line). The graphs represent the flow through the LSPV, RSPV, LIPV and RIPV, respectively.

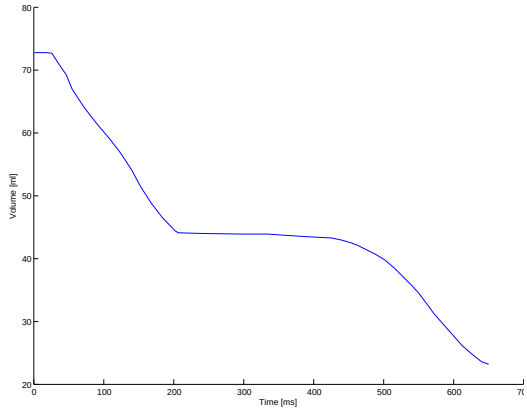

Figure 8.4: The volume change of the atrial cavity measured from MR recordings throughout diastole.

smooth contour of the atrial wall towards the septal/inferior side of the mitral plane. The jet is deflected by the jet from the LIPV, but the jets do not interfere at this stage. The streamlines originating in the RSPV, fig. 8.5(b), behaves in a similar manner but enters the MV at the septal/superior side. The outer, most superior, part of the RSPV inflow, is disturbed by the jet from the LSPV and turns into a rotational motion towards and into the LAA before crossing the mitral plane at its lateral side just below the appendix.

In our subject, the trunks of the LPVs are oriented almost perpendicular to the atrial chamber. The direction of the inflowing jets, fig. 8.5(c) and (d), are therefore almost parallel to the mitral plane. The flow from the left veins have the highest velocities due to their small orifice areas (see Table 8.1). As they flow into the atrial chamber, the jets are deflected by the flow descending from the RPVs. The jets change direction with almost 90 degrees before heading towards the mitral plane.

The main part of the flow from the LSPV enters the central/superior part of the mitral orifice, whereas the rest is involved in the swirling motion caused by the interaction with the RSPV jet. The LIPVs' inflow, on the other hand, occupies the center towards the inferior side of the MV. Some of the streamlines originating from the LIPV recirculate into a clockwise vortex before entering the valve.

During the deceleration of the E-wave, the degree of recirculation increases. As the transmitral flow diminishes in mid-diastole and the atrial volume stays constant, the vortices increase in size and number, resulting in an even more complex flow field as illustrated in Fig. 8.6. At the onset of the second filling, A-wave, the vortices disappear and the main part of the venous inflows are again constrained into more direct paths towards the mitral valve.

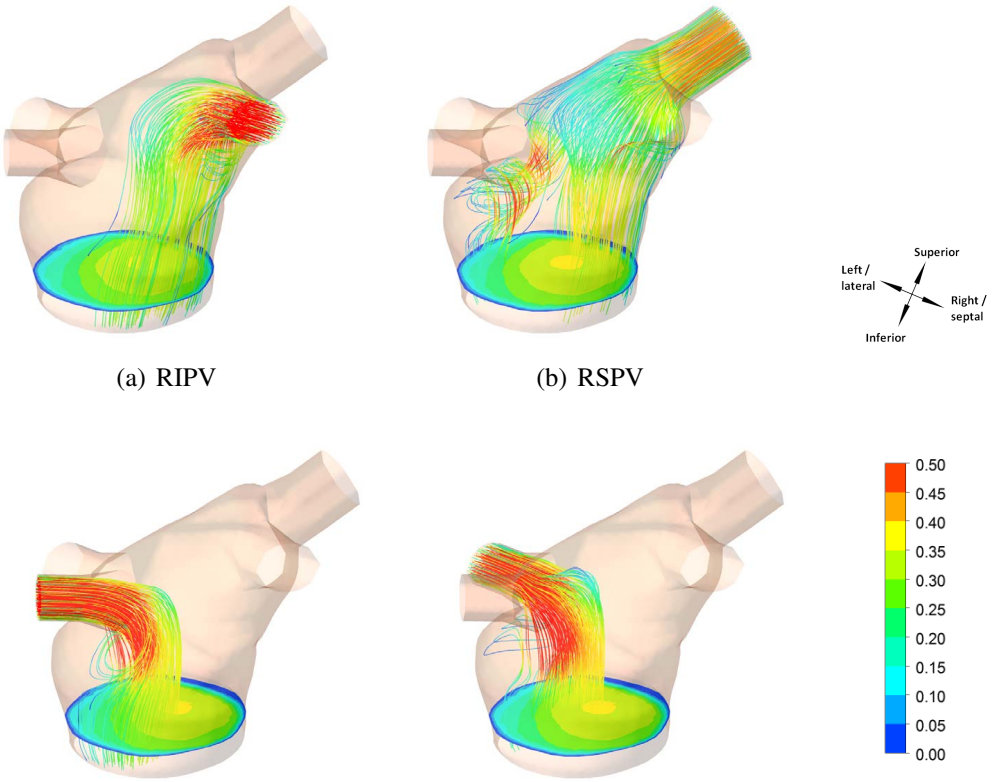

(a) RIPV (b) RSPV

(c) LIPV (d) LSPV

Figure 8.5: The figure shows the velocity contour at the level of the mitral valve and the streamline for each of the four veins during the acceleration of the first filling wave, $t = 100ms$. The velocity scale is given in $[m/s]$. The cross shows the orientation of the model as seen from an atrial view.

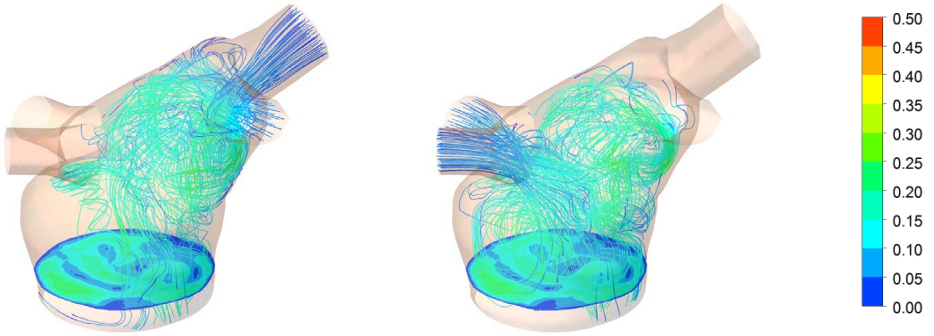

(a) right PVs (b) left PVs

Figure 8.6: The figure shows the velocity contours at the level of the mitral valve with a more complex flow field of mid-diastole compared to early diastole. In (a) and (b) the streamlines of the right and left PVs are illustrated, respectively. The velocity is given in $[m/s]$

8.3.2 Sensitivity to PV location

The graph in Fig. 8.7 illustrates the maximum transmitral velocity for c_A, c_B and c_C, throughout diastole. During the acceleration of the first filling the maximum velocity is the same for the three cases. When approaching peak velocity, the results start to deviate. The maximum is reached at $t = 160ms$ for c_A with a velocity of $0.50m/s$. In c_B and c_C, the maximum velocities are 16% and 33% higher than in c_A and occur 45 and $30ms$ later, respectively. The variations in maximum velocity decreases in mid-diastole, but increases again at atrial contraction. This time the highest velocity occurs in c_A. It is interesting to notice that the ratio of peak E to peak A velocity (E/A ratio), changes significantly with the location of the veins. The E/A ratio yields 1.85, 2.72 and 3.10 in c_A, c_B and c_C, respectively. Only c_A fall within the range of clinically reported data of 1.5 ± 0.40 [4].

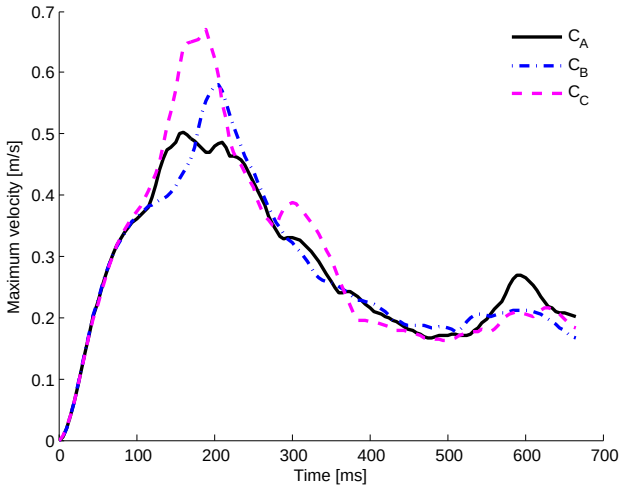

Figure 8.7: The graph illustrates the maximum transmitral velocity of c_A , c_B and c_C throughout diastole.

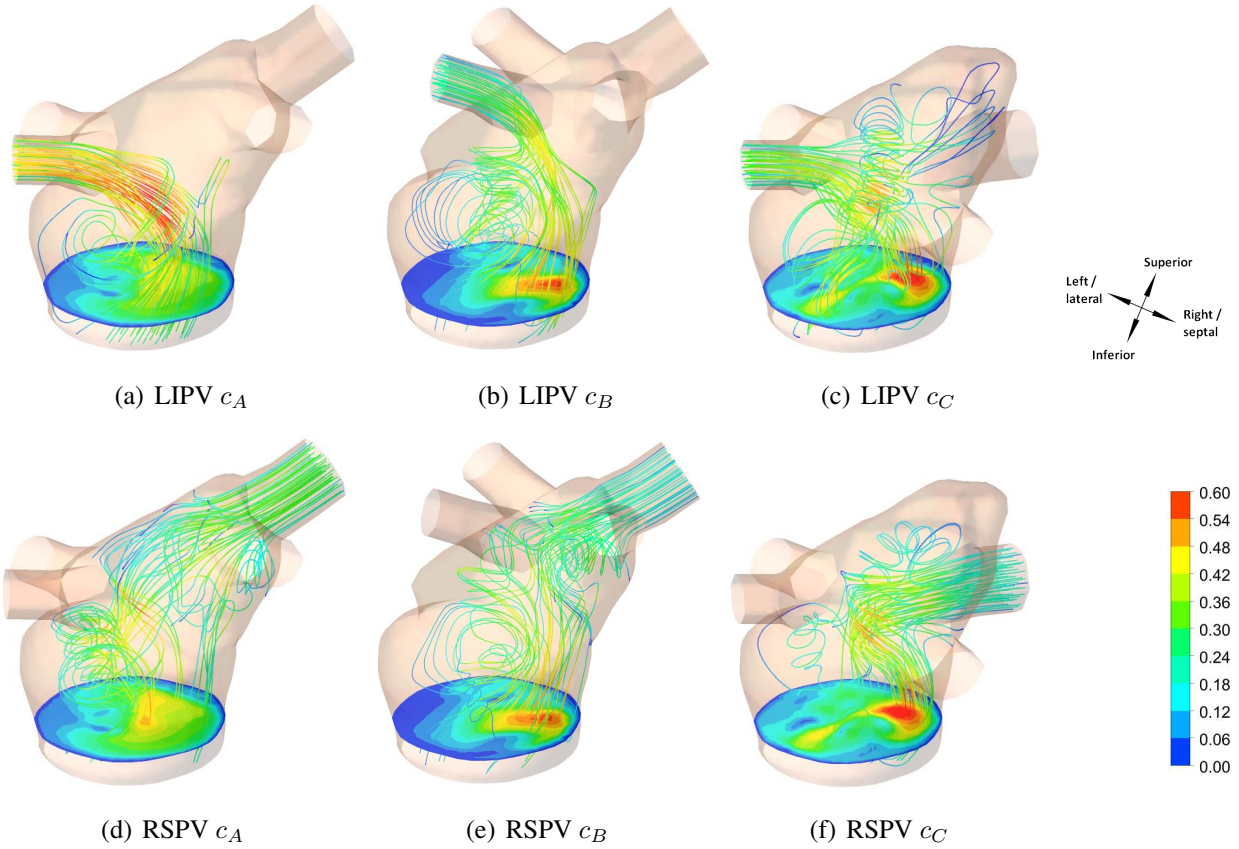

(a) LIPV c_A (b) LIPV c_B (c) LIPV c_C

(d) RSPV c_A (e) RSPV c_B (f) RSPV c_C

Figure 8.8: Streamlines from LIPV and RSPV are plotted for each configuration at their maximum velocity. The maximum velocity occurs at $t = 160ms$, $t = 205ms$ and $t = 190ms$ for c_A, c_B and c_C, respectively. The contours shows the velocity distribution at the MV plane, given in [m/s].

Fig. 8.8 shows the streamlines from the LIPV and the RSPV for each case at their respective maximum velocity. The shortest atrial transit time for blood originating in the LIPV, was found for model c_A. For c_C, the distance from the LIPV to the MV is exactly the same as for c_A, but the average transit time was higher. This is because the left and right jets collide with each other in c_C, and induce a recirculating motion towards the upper part of the LA. In c_B, Fig. 8.8(b), some of the streamlines goes directly to the septal side of the mitral opening, while another portion turn into a swirling motion towards and also into the LAA.

The jet from the RSPV is, in c_A, similar to the one observed in Fig. 8.5(b), but the degree of recirculation has increased and the flow profile at the MV has changed. In c_C, Fig. 8.8(f), the right jets collide with the jets from the LPVs and change direction completely. Whereas large parts of the flow from the LIPV was forced into a swirling motion, the jet from the RSPV turns directly towards the septal side of the MV. For c_B, the streamlines originating in the RSPV are similar to the streamlines origination in the LIPV, but the number of streamlines having a direct path towards the MV is less.

8.3.3 Cross-sectional velocity profile at the mitral plane

Fig. 8.9 shows the transmitral velocity distribution for c_A , c_B and c_C at 6 different times during the first filling wave. The instant when the maximum transmitral velocity occur lies within the selected time span for all three cases.

Fig. 8.9 clearly illustrates that the locations of the PVs have a significant impact on the orientation of the skewness in the mitral velocity profile. During the acceleration of the E-wave, all three models have the highest veloctites in the septal/superior quadrant of the mitral opening. As time progresses the velocity distributions become more skewed and dissimilar. In c_B, the highest transmitral velocities are mainly restricted to a limited spatial area at the right half of the opening, while the flow is almost zero at the lateral side. In the two other models, the blood flow covers a larger part of the MV. In c_C, a narrow area with high velocity is stretched across the MV from the superior/septal side to the inferior/lateral side, this model has the highest velocities. In c_A, the velocity is more evenly distributed. At $t = 160ms$, the region with high velocity is covering the right half of the MV, whereas at $t = 200ms$ the highest velocity is found along the mitral border, like a horseshoe with its opening towards the lateral side.

The simulated profiles were qualitatively compared with the MRI flow profile. Fig. 8.10 shows the velocity distribution at the mitral plane during peak E-wave, as measured with MRI. The maximum velocity was found to be $0.60m/s$. The MRI flow pattern resembles a horseshoe-like profile, similar to the profile observed in c_A. The highest velocities is seen in the septal/superior quadrant, whereas the lowest inflow is occur at the lateral side. The best agreement between the measured and simulated velocity distribution was found in c_A.

8.4 Discussion

In this study, we used MRI to construct an anatomically based geometric model of the LA and its PVs. The aim was to investigate the flow field in the LA during diastole and the impact of the PVs' entry location on the intra-atrial flow and the resulting mitral plane velocity distribution. Three models with different venous entry locations were created. The results illustrate that the locations of the PVs have a significant impact on the flow field. In the model with the anatomically based PV positions, the venous jets flow towards the mitral plane without noticeable collision, this model also produces a more uniformly distributed mitral flow profile with lower maximal velocity than both the other models where the PVs are located at the same height. The interpatient variability in PV number and branching patterns is large, hence, the mitral velocity profile should be considered as a subject-specific property. It will not be possible to predict the nature of the mitral jet by making general deductions about the conditions under which the jet is formed. Therefore, a representative geometry of both the LA and the PVs, is essential for physiological simulations of LV filling and MV dynamics.

8.4.1 Intra-atrial flow

The intra-atrial flow is made up of four crossing jets flowing into an asymmetric chamber and is therefore complex. Each jet behaves very differently during diastole. To the best of our knowledge our study is the first to apply in-vivo measured PV mass flow rates as an inlet condition in a CFD simulation. By using individual measurements of the venous inflow rates, we ensure a realistic distribution

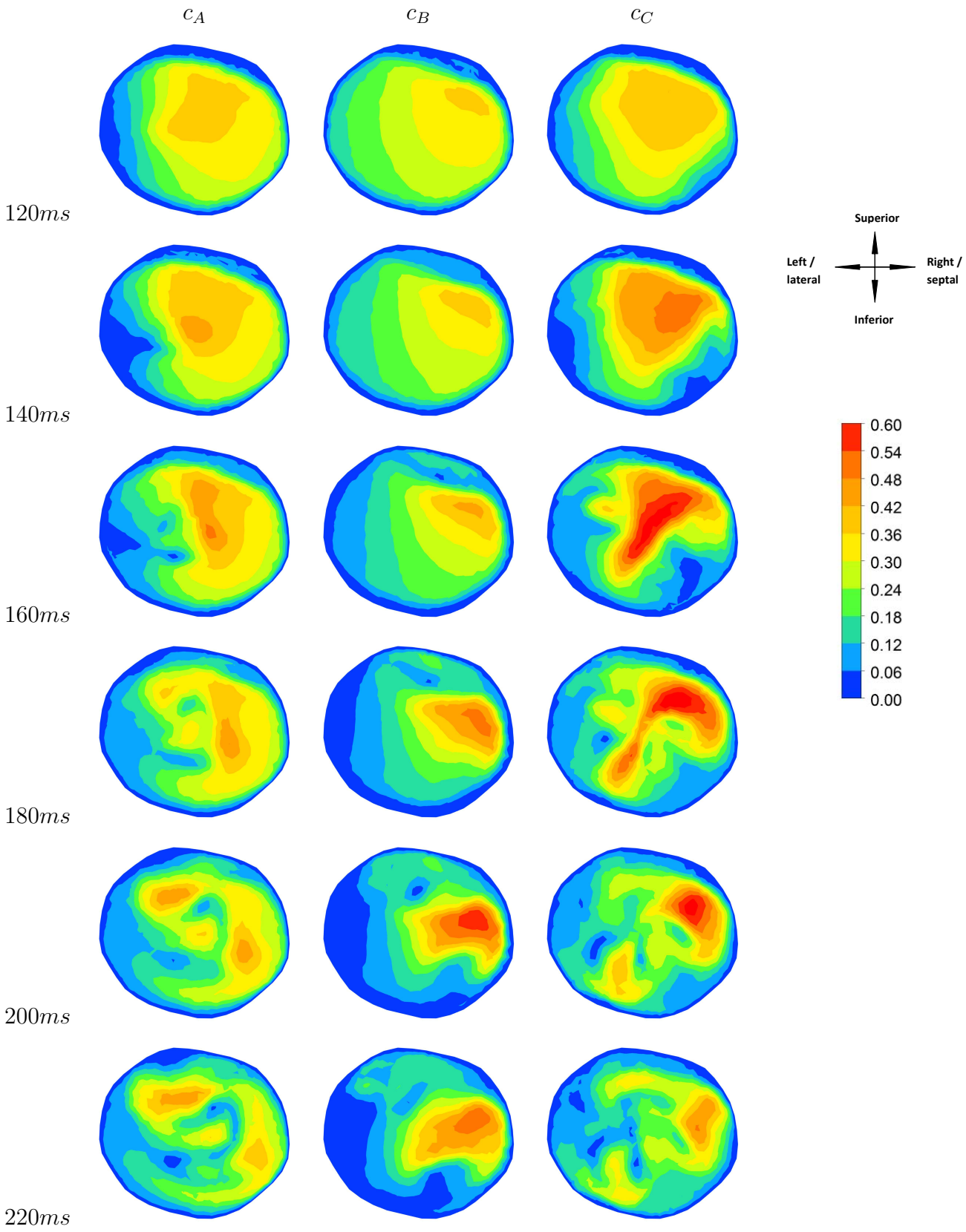

Figure 8.9: Velocity contours at the mitral opening, seen from an atrial view, at 6 different times during diastole. The three columns are c_A, c_B and c_C, respectively.

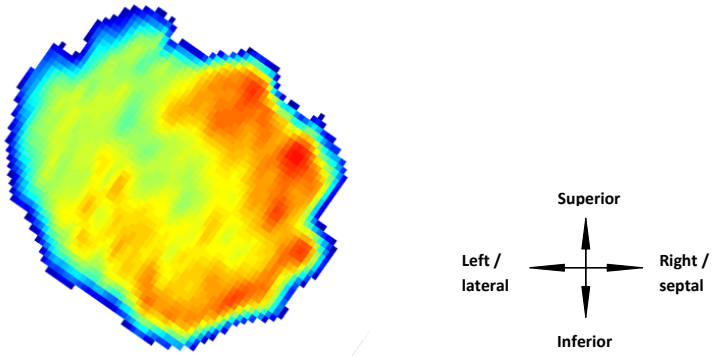

Figure 8.10: The transmitral velocity distribution as measured with MRI at peak E-velocity and the orientation of the mitral plane as seen from an atrial view. The maximum velocity is $0.6m/s$.

of the incoming impulses which in turn decide how the jets interact with each other. Qualitatively, the simulated flow field in c_A shows good agreement with reported observations [42, 55, 110].

Kilner *et al.* [55], suggested that an eccentric alignment of the PVs predispose to asymmetry of the intra-atrial flow, redirecting inflow towards, rather than away from, the valve. The asymmetry might also avoid instabilities by allowing entering, recirculating and outflowing streams to pass without collision. In the anatomically based model c_A, the jets cross without noticeable collisions. In c_B, where the PVs are entering at the same level, the inflowing jets collide, and thereby force parts of the flow into a recirculating motion towards the upper part of the LA, away from the MV. In addition, the asymmetric located veins in c_A seem to produce a more uniformly distributed mitral flow profile with lower maximal velocity than both c_B and c_C.

To compensate for the stationary atrium used in our simulations, additional mass due to atrial contraction was evenly distributed among the four venous inlets. Different amounts of additional mass were tested to observe the impact on the resulting flow field. We observed that with increasing additional mass, the magnitude of the velocity increased, whereas the atrial and mitral flow pattern remained the same. This indicates that as long as the added mass flow is equally distributed among the veins, the relative impulse magnitude of each jet is maintained and thus, the way the jets interact will not change. The magnitude of the mass flow obtained from the anatomical acquisition data were lower than the mass flow measured from the MRI phase mapping scans. This discrepancy can be attributed to inaccuracies in the MRI recordings and in our segmentation. Also the differences in heart rate between the acquisitions of the anatomical data and the acquisitions of the velocity data might cause a difference between the measured mass flow rates.

8.4.2 Mitral velocity distribution

The interaction between the four incoming jets and the asymmetric atrial geometry results in a skewed velocity profile at the mitral orifice. Our simulations show that the PV locations have significant impact on the mitral velocity pattern. The best qualitative agreement between the measured and simulated velocity distribution was found in c_A. Both profiles resembled a horseshoe, with an opening towards the lateral side. In c_B and c_C, the velocities were higher and concentrated to smaller areas. The interpatient variability in PV number and branching patterns are large [17, 54, 67] and the mitral

velocity distribution should therefore be considered as a subject specific property.

Numerical simulations of LV flow are highly sensitive to the imposed boundary conditions during diastolic filling [27, 63, 98]. Generic, simplified atrial geometries will cause circulation above the mitral plane and hence a nonuniform mitral profile, but the skewness will most likely not be physiological. Together, the irregular shape of the LA and the interpatient variability in PV anatomy make it questionable whether general morphological simplifications can be applied in simulations of intra-atrial flow. The velocity distribution across the mitral plane depends, in a complex way, on several factors. In addition to the PVs' size, shape and branching pattern and the relative flow distribution between them, the atrial flow field will also depend upon the geometry and nature of the atrium, the shape of the mitral orifice, the viscosity of the blood, the degree of suction from the LV, etc. Further studies are needed in order to address the impact of the most important factors on the resulting MV velocity profile.

For bileaflet mechanical heart valves (BMHV), where each leaflet is allowed to rotate independently due to interaction with the blood flow, a skewed mitral profile may lead to different opening patterns for the two leaflets. A physiological velocity distribution across the mitral opening will therefore be essential to capture this phenomenon.

8.4.3 Limitations

A static LA with added mass flow at the venous inlets will cause stronger jets and more intense vortices than a moving LA without added mass flow. In a static LA, the blood entering the MV will mainly come from the PVs and not from the blood that was stored in the LA. Hence, the maximal transmitral velocity will be higher and occur later, compared to the more physiological case with a contracting LA. The simulated velocities in c_A are lower than the velocities measured with MRI, we therefore assume that our added mass flow is lower than in-vivo. The mass flow rate measured from MRI phase mapping scans are, for that reason, probably more correct than the mass flow rate obtained from our segmentation data.

Both the mass flow rate and the velocity pattern at the MV have to be physiological for physiological simulations of the LV flow field. This can only be achieved by including a moving atrium. If the LA is static, a physiologically correct transmitral mass flow rate will result in too high velocities at the MV, whereas a correct mitral velocity magnitude will require a mass flow rate which is too low. We are currently improving our atrial model to account for a moving atrial geometry.

A compliant annuls will influence the velocity distribution during start diastole when the area of the annulus increases. However, according to our measurements the area of the annulus is almost constant after peak E-wave and hence will not notable influence the mitral velocity profile.

8.4.4 Conclusions

In this study, we have presented three 3D CFD simulations focusing on the intra-atrial flow and the resulting mitral plane velocity profile during LV diastole. The anatomically based 3D geometries of the LA and the PVs were obtained from MRI recordings of a young healthy adult. The entry locations of the PVs were different in the three models.

Four jets enter the asymmetric atrium, and the resulting flow field is therefore complex. Our results clearly illustrate that the locations of the PVs have a significant impact on the intra-atrial flow field and the velocity distribution at the mitral plane. The asymmetric locations of the PVs might

prevent instabilities in the flow field. We observed that in the model with anatomically based PV positions, the venous jets flow towards the mitral plane without noticeable collision. This model also produces a more uniformly distributed flow profile at the mitral plane with a lower maximal velocity than both the other models where the PVs are located at the same height. The mitral velocity profile in the anatomically representative model, showed qualitatively good agreement with the MRI flow measurements.

Due to the large interpatient variability in PV anatomy, the mitral velocity profile should be considered as a subject-specific property. Therefore, a representative geometry of both the LA and the PVs, is essential for physiological simulations of LV filling and MV dynamics. Our findings may influence future CFD studies regarding transmitral and intraventricular flow.

Acknowledgment

The authors would like to express their gratitude to MD, PhD Brage Amundsen, Dept. of Circulation and Medical Imaging, NTNU, for performing the MRI recordings at St.Olavs University Hospital, Trondheim, Norway, and to Prof.em. Tor Ytrehus at the Fluids Engineering Group, NTNU, for all the fruitful discussions.

Chapter 9

3D moving boundary conditions for heart CFD simulations - from echocardiographic recordings to discretized surfaces

3D moving boundary conditions for heart CFD simulations - from echocardiographic recordings to discretized surfaces

S. K. Dahl, E. Fagerholt, G. Kiss, V. Prot, B. Amundsen, L. R. Hellevik and B. Skallerud

MekIT'11: Sixth National Conference on Computational Mechanics, Trondheim, 23-24 May 2011, Tapir Akademisk Forlag 2011, ISBN 978-82-519-2798-7: p. 33-46.

9.1 Introduction

Cardiovascular disease is the most common cause of death in the western world and thus, it is of great interest in heart research to better understand this organ's structure and function and to improve diagnosis and therapy methods. The heart is a complex system whose function depends on many levels, from cells to tissue, on electrical activation, metabolism, structural dynamics, blood dynamics etc. Alternation on one level will affect the other levels and hence change the pumping action of the heart. Thus, the intraventricular fluid pattern may reflect the function of the organ. Up to date, various studies have led to an increased understanding of myocardial mechanisms, whereas little is known about blood dynamics inside the heart. A computational fluid dynamics (CFD) simulation of the pumping ventricle can help us to understand the complex flow phenomenon.

The left ventricle (LV) in the heart undergoes large and complex deformations during one cardiac cycle. The deformation is characterized by circumferential and longitudinal shortening as well as torsion about the LV central axis. The motion of blood inside the ventricle, cannot be known without knowledge of the boundary motion. Different approaches have been suggested in order to create a 3D model of the LV. All studies have various shortcomings and none of the 3D models are yet applicable on a clinical base. The numerical models of the LV can roughly be divided into two types. This is fluid structure interaction (FSI) models which take into account the interaction between the fluid flow and the surrounding tissue, and prescribed geometry models, which uses the movement of the inner ventricular wall as a boundary condition in a CFD simulation. Both models cannot be considered as alternatives to each other but approaches in their own right [98].

To analyze intraventricular flow and to develop patient-specific simulation models in order to perform "virtual surgery", prescribed geometry models are today better suited. Computational fluid dynamics allows us to obtain realistic flow fields in complex geometries by solving the non-linear equations of mass and momentum conservation in a discretized form. Coupling CFD with noninvasive methods of visualizing the heart, enables the opportunity to reconstruct subject-specific simulation models. Integration of CFD and medical imaging is not novel. Different imaging disciplines, like computed tomography (CT), magnetic resonance imaging (MRI) and echocardiography, have in the recent years been supported by simulations.

However, in most studies which include a prescribed LV wall movement, MRI has been used to extract the transient geometry. MRI has a clear advantage with respect to image quality, but the cardiac valves are often less distinguishable due to the high signal from blood. MRI is not as commonly available as other modalities in the clinic, due to its relatively high cost and longer acquisition time. 3D echocardiography, on the other hand, has undergone large improvements the last few years, and both image quality and temporal resolution are now at a level that makes it possible to extract high quality 3D geometries and movement. The particular strength of echocardiography, is its ability to record moving structures in real-time and is, among medical doctors, the most applied method for diagnosing the heart. There exists an extensive amount of patient specific 2D echocardiographic data. Now, 3D echocardiography is gaining popularity as a routine clinical tool and this is one of our arguments for choosing this modality as the basis for moving boundaries in patient-specific CFD models.

Previously, a 2D patient-specific model of the left heart has been developed [27]. The LV wall geometry and motion were extracted from 2D echocardiographic recordings and successfully implemented in a 2D CFD simulation. A 2D simulation can give qualitative information about the flow field, but to obtain quantitative data, 3D simulations are necessary.

In this paper, we present a newly developed method for the creation of subject-specific LV boundary conditions for 3D CFD simulations from echocardiographic recordings. The geometry includes an advanced transient finite element mitral valve model, pre-analysed in Abaqus [84, 85]. The algorithms provide a framework for the coupling of different data sets which together makes up the LV and its apparatus. We have focused on echocardiographic data, however, the method is modality-independent and can be combined with both MRI and echocardiography.

As computer performance increases and the computational efficiency of the models improve, clinical applications might become feasible. The future goal is that the models can be used for identification of clinical parameters, which in turn, could be important for diagnosing cardiovascular pathologies.

9.2 Method

9.2.1 3D echocardiography and segmentation of the LV

Real-time three-dimensional (3D) echocardiography (RT3DE) (also known as four-dimensional (4D) echocardiography) with consecutive segmentation of the endocardial LV wall are the preliminary steps in building our subject-specific CFD model.

The 3D echocardiography LV volume of a 30 years old female volunteer was acquired using a Vivid E9 scanner using a 3V matrix probe with a center frequency 2.4 MHz (GE Healthcare Vingmed, Horten, Norway). The volume was acquired during apnea over 4 heart cycles, from the apical window, in harmonic mode, one QRS triggered sub-volume acquired per heart cycle. The frame rate was 27 per cycle.

For our study the endocardial border was generated using the AutoLVQ tool [46], EchoPAC workstation (version BT 11), GE Vingmed Ultrasound, Hortem, Norway. AutoLVQ represents the LV boundary as a deformable model and relies on 3D energy minimization for evolving it. A combination of internal, external and temporal forces ensure shape continuity, while adapting the model to a particular 3D echo recording. The endocardial contour process was initialized by manual positioning of the apex and the mitral valve attachment points in a long-axis view (e.g. four chamber), both at end-diastole (ED) and end-systole (ES). After manual selection, the endocardial border is automatically generated throughout the cardiac cycle. The proposed contour was then evaluated in both short- and long-axis cut-planes of the 3D volume. If deemed necessary the border can be further refined by adding additional attractor points that pull the model towards the endocardium. In this case, the border was adjusted by placing a limited number of attractors. The papillary muscles and major trabeculae were included in the LV cavity both in diastole and systole. The resulting triangular meshes were exported and later reused in the construction of the CFD model.

9.2.2 3D finite element model of the mitral valve

The geometry and time dependent shape of the valve leaflets are not easily extractable from echocardiographic recordings, manual tracing is, today, the only alternative. Therefore, we chose to represent the MV by a finite element model (FEM) pre-simulated in Abaqus [84, 85]. Only the systolic phase of the cardiac cycle was computed in this transient finite element (FE) simulation. The simulation

resulted in 176 time frames in systole. The prescribed leaflets' movement were subsequently implemented in the CFD model.

The geometry of the FE MV model is described in [84, 85]. The shape of the annulus was measured at early systole from 3D echocardiographic recordings of the heart of an anaesthetized pig. The annulus was idealized as a non-planar ellipse. The size of the mitral annulus in the volunteer was approximately of the same size as in the FE MV model, hence the model did not have to be scaled to fit the LV base.

An incompressible transversely isotropic hyperelastic material described in [85] was used to model both leaflets. The annulus was assumed to be fixed, with translations constrained but not the rotations. In order to capture coaptation (i.e., apposition of the posterior and anterior leaflets) a contact condition was prescribed on the atrium surface of the leaflets. The blood pressure measured in the left ventricle of the pig during systole was applied on the ventricular surface of the leaflets as load history. All simulations were quasi-static.

9.2.3 Geometrical reconstruction

The segmented endocardial LV wall derived from RT3DE consisted of closed three dimensional surface meshes for 27 different time steps. Together they describe the inner ventricular wall movement. The FE MV model and also an outflow tract have to be incorporated in the original segmented LV grid topology for all frames. This requires some manual work, however, effort was made to limit the amount of manual interaction.The algorithms were constructed in such a way that user intervention was necessary only in the first frame, i.e. start systole. The different steps are described below.

9.2.4 Mitral valve position optimisation

In the first frame, start systole, the MV model was positioned manually to fit the LV model. After this first initial positioning of the MV model, a region of the LV model was cut, i.e. cells were removed from the LV model, to make room for the MV model. Effort was made to make sure that the removed surface region of the LV model was large enough to fit the MV model in all frames of the cardiac cycle. When cutting the original grid topology the cells at the border may lead to sharp edges. To overcome this problem, a smoothing algorithm based on the principle of moving average was written. The boundary nodes were moved according to the algorithm, creating a smooth boundary of the cut region. Figure 9.1 illustrates the LV edge before and after smoothing.

Then, a connect model was generated manually, combining the MV and LV model. The connect model was created by making triangular cells that combine the outer line of the MV model (annulus) with the outer line of the removed region of the LV model, resulting in a closed surface of the combined LV-MV model. No extra nodes were generated in this process. Fig. 9.2 a) illustrates the LV model with its manually generated connect model, shown as white cells. Fig. 9.2 b) and c) shows the combined LV-MV model.

In order to get the best possible positioning of the MV model in each LV frame, a least square optimization routine was implemented. This was carried out by optimizing the six parameters of the translation and the rotation of the LV model, minimizing the area of the triangular cells in the connect model. This optimization was then carried out for the remaining frames in the whole cycle, providing a set of optimized translation and rotation parameters for the LV model in each frame. The

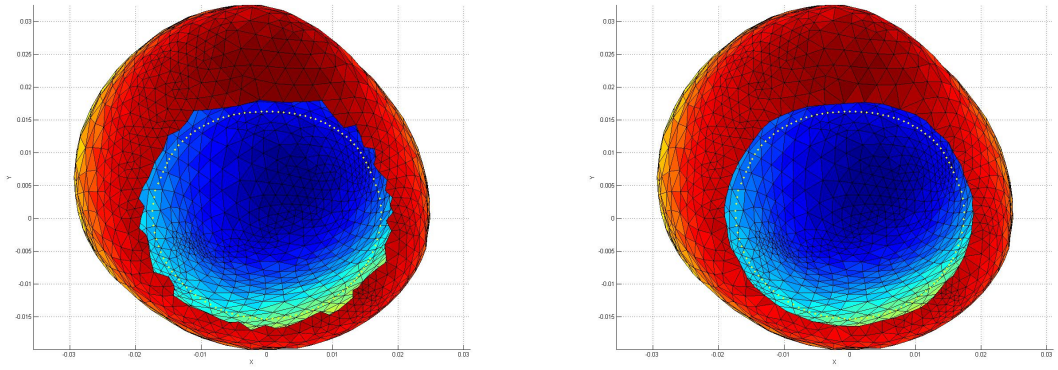

(a) before smoothing (b) after smoothing

Figure 9.1: The LV edge before and after smoothing. The dotted line is the contour of the MV annulus

optimization was highly necessary to obtain a correct position of the MV at the LV base. Fig. 9.3 illustrates the combined model at end systole, before and after optimization.

9.2.5 Construction of the left ventricular outflow tract (LVOT) and the ascending aorta (Aao)

The ascending aorta is the first section of the aorta, commencing at the upper part of the base of the left ventricle, beginning at the aortic annulus / left ventricular outflow tract (LVOT). In the parasternal long axis view, the aortic annulus is between the outflow tract anterior and posterior endocardiums immediately below the attachments of the anterior and posterior aortic valve leaflets as can be seen in figure 9.4.

To assess the different parameters needed to reconstruct the LVOT and the very beginning of the ascending aorta, a software which enable the possibility of manually tracing echocardiographic recordings was constructed. The measurements, described below, were done in 2D mode in the parasternal long axis view as shown in figure 9.4.

The first step is to cut the LV model and remove redundant cells to make room for the outflow tract. Like for the MV, this was done in the first frame of systole. Starting from the highest point of the anterior mitral annulus in the combined model, a cutting plane was constructed. To define the plane's tilting angle, we used the obtuse angle between the aortic and mitral annulus, measured in the echocardiographic recordings. All grid cells above this plane was removed from the model, creating an approximately circular opening at the LV base. The cells at the edge were then smoothed using the algorithm described in the previous section. The model with the smoothed edge is illustrated in Fig. 9.5. The vector defining the cutting plane is also plotted in the figure.

Second, the LVOT from the smoothed edge up to the aortic annulus and the very beginning of the Aao have to be reconstructed. The aorto-mitral-curtain, which is the wall from the highest point of the anterior mitral annulus up to the aortic annulus, will act as a leading edge in the construction of new elements. This edge was traced in the parasternal long axis view for all frames and the mean value was used in the modeling. The aorto-mitral-curtain is drawn with a green line in Fig. 9.4 and is

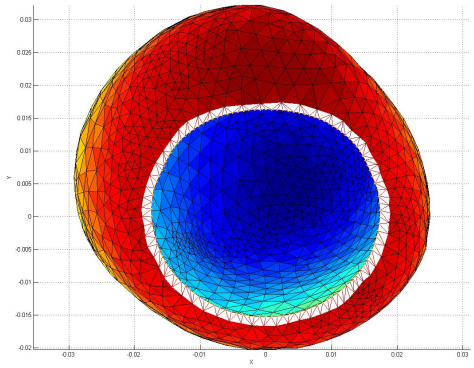

(a) LV with connect model in white

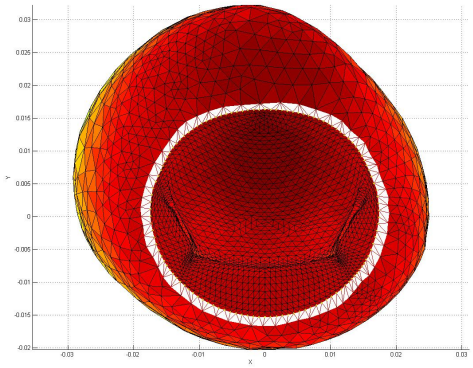

(b) combined LV-MV model

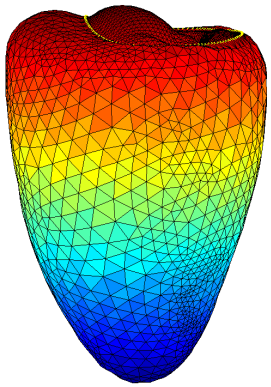

(c) combined model, side view

Figure 9.2: The manually positioned MV on the LV base in the start frame, i.e start systole. a) illustrates the LV model with its manually generated connect model in white and the dotted MV annulus. b) and c) shows the combined LV-MV model from the top and the side, respectively

illustrated with a dotted blue line in Fig. 9.5. A prolongation of the aorto-mitral-curtain was used to create the very beginning of the ascending aorta. The aortic root with its sinuses of Valsalva, which is the first part of the Aao, was simplified to a tube because the area of interest will, in our study, be the flow at the level of the aortic annulus, not the flow pattern further out in the aorta.

9.2.6 Prescribed LV movement

The time-varying 3D endocardial surface mesh of the left ventricle is used as a boundary condition in our CFD simulation. However, the original surface mesh obtained from the echocardiographic data is quite coarse consisting of 1946 nodes and 3888 triangular cells. Because the accuracy of CFD results relies heavily on the grid resolution, a refined surface mesh is required to be able to capture the global flow pattern inside the LV with a reasonable accuracy.

A refined mesh will result in new intermediate nodes in the start geometry, which are not a part of the original mesh extracted from the echocardiographic recordings. This means, their nodal positions

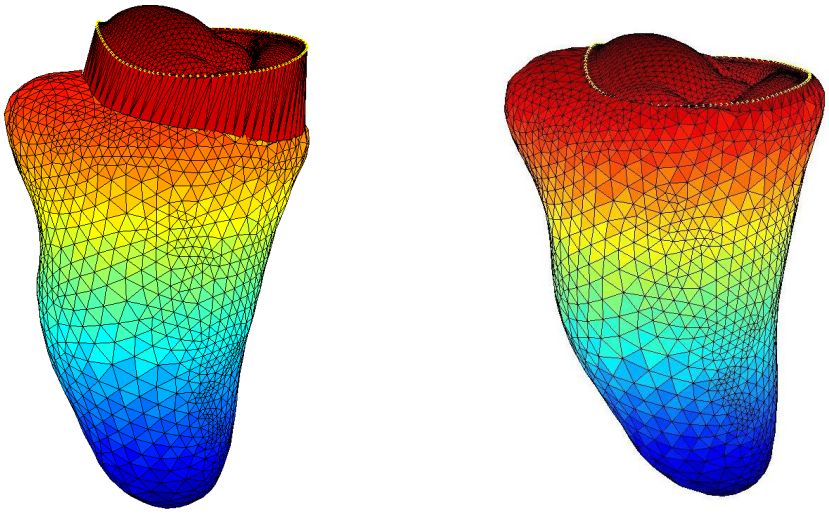

(a) before optimization (b) after optimization

Figure 9.3: The position of the MV in frame 10, i.e. end systole, before and after optimization of MV position and rotation

are unknown for the subsequent time frames. Therefore, the nodal translations of the refined mesh have to be interpolated from the original mesh throughout the cycle. Fig. 9.7, shows a close up of the LV surface mesh in the start geometry. The green cells are the original grid, whereas the yellow cells are a result of the grid refinement.

In order to compute the prescribed movement of the refined mesh, every mesh node has to be related to the original grid. It is sufficient to find this relation for a single frame, since the cell numbering of the original grid stays the same throughout the whole cycle. So, first, the node's appurtenant triangular cell in the original grid has to be found. Second, the node's new position has to be calculated by interpolation of the cell's vertices; A, B and C, for every time frame.

Generally, a triangle is defined by its three vertices, A, B and C. Three points define a plane, a triangle is therefore a 2D element, ΔABC. A 2D triangle can exist in either the 2D or the 3D space. In our case, the triangle is a cell from the original grid which exists in the 3D space. We want to know whether an arbitrary point, P, which here is a surface node, belongs to the triangle, ΔABC, or not. This was achieved by the use of barycentric coordinates. The barycentric coordinates of a point P with respect to the vertices A, B and C of the triangle, ΔABC, can be written as a weighted sum of the tree vertices:

$$P = \lambda_1 A + \lambda_2 B + \lambda_3 C \tag{9.1}$$

where λ_1, λ_2 and λ_3 are the weighting functions subjected to the constraint:

$$\lambda_1 + \lambda_2 + \lambda_3 = 1 \tag{9.2}$$

Using vector formulation, Eq. 9.1 can be rewritten:

$$\mathbf{x}_P = \lambda_1 \mathbf{x}_A + \lambda_2 \mathbf{x}_B + \lambda_3 \mathbf{x}_C \tag{9.3}$$

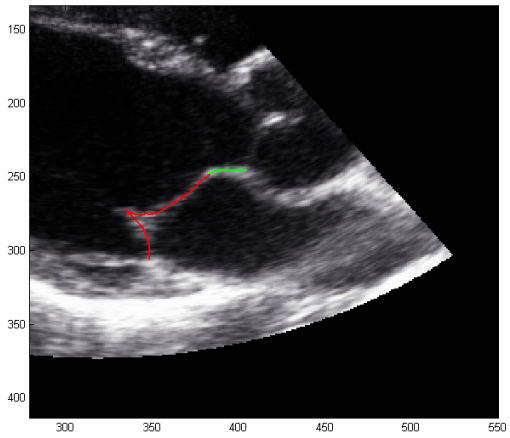

Figure 9.4: The parasternal long axis view in which the mitral valve and the incline of the endocardial wall between the mitral and aortic annulus have been traced. This is illustrated by a red and green line, respectively.

There are many ways of actually computing the barycentric coordinates λ_i for P with respect to the triangle ΔABC. Because of the large number of nodes and time frames, it is desired to have a computational effective technique to reduce processing time. Three different methods were tested in order to find the one which was less computationally expensive.

The first two methods were based on the principle of normalised subareas. Let P be a point inside the triangle as shown in Fig. 9.8. It divides the triangle into three sub-triangles. The normalised areas of the sub-triangles, A_1, A_2 and A_3, are then used to compute the barycentric coordinates, λ_i, of P.

Any point within the triangle can then be described by:

$$\mathbf{x}_P = \left(\frac{A_1}{A}\right)\mathbf{x}_A + \left(\frac{A_2}{A}\right)\mathbf{x}_B + \left(\frac{A_3}{A}\right)\mathbf{x}_C \tag{9.4}$$

To test whether the given point, P, is inside a cell or not, two different techniques were analyzed. The first method checked if the cross products of the legs of the subtriangles, as illustrated in Fig. 9.8, pointed in the same direction. If they did, the point was inside. The other method utilised the residual of the equation:

$$res = A - A_1 - A_2 - A_3 \tag{9.5}$$

The cell having the minimal residual was the correct cell.

The two above mentioned techniques are conceptually straightforward, but somewhat expensive computation-wise. Due to the high numbers of nodes and cells in the model, a third method which eliminates one of the barycentric coordinates were tested to see if this made the calculations less computationally expensive.

Using Eq. 9.2, we can define λ_1 in terms of λ_2 and λ_3:

$$\lambda_1 = 1 - \lambda_2 - \lambda_3 \tag{9.6}$$

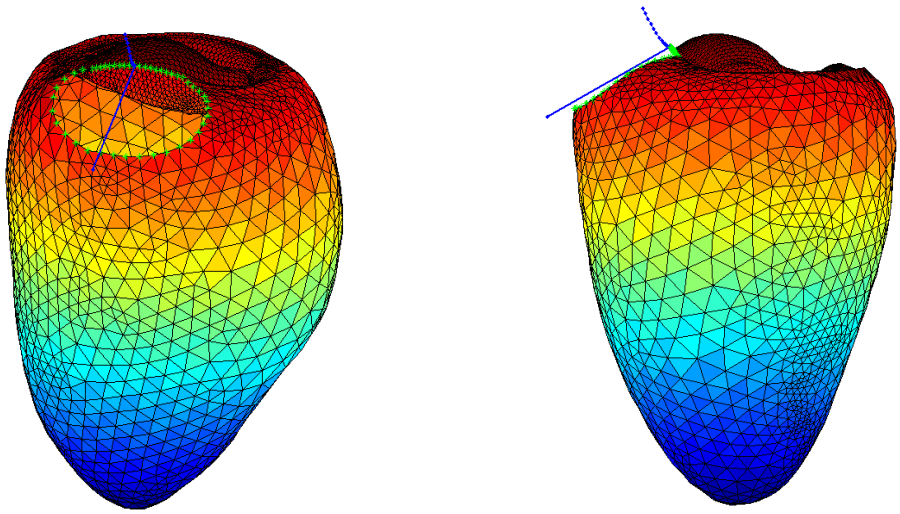

(a) front view (b) side view

Figure 9.5: The LV model with the smoothed edge (green dots). The blue line is the vector used to obtain the cutting plane. The tracing of the aorto-mitral-curtain used in the construction of the LVOT is illustrated with blue dots. Both (a) and (b) are from start systole.

Substituting Eq. 9.6 into Eq. 9.1 we obtain:

$$\mathbf{x}_P = (1 - \lambda_2 - \lambda_3)\mathbf{x}_A + \lambda_2\mathbf{x}_B + \lambda_3\mathbf{x}_C \tag{9.7}$$

Rearranging and denoting λ_2 and λ_3 as u and v, respectively, then:

$$\mathbf{x}_P = \mathbf{x}_A + u(\mathbf{x}_B - \mathbf{x}_A) + v(\mathbf{x}_C - \mathbf{x}_A) \tag{9.8}$$

Given u and v, point P can easily be calculated with Eq. 9.8. In our case we have to go in the reverse direction and calculate u and v from a given point P. So, we have two unknowns, which means we need two equations to solve for them. Starting with Eq. 9.8, subtracting $\mathbf{x}_A$ from both sides, we get:

$$\mathbf{x}_P - \mathbf{x}_A = u(\mathbf{x}_B - \mathbf{x}_A) + v(\mathbf{x}_C - \mathbf{x}_A) \tag{9.9}$$

If we introduce the vectors: $\mathbf{p} = \mathbf{x}_P - \mathbf{x}_A$, $\mathbf{b} = \mathbf{x}_B - \mathbf{x}_A$ and $\mathbf{c} = \mathbf{x}_C - \mathbf{x}_A$ we can write Eq. 9.9 in a more convenient form:

$$\mathbf{p} = u\mathbf{b} + v\mathbf{c} \tag{9.10}$$

The principle of this method is that a triangle can be described by two vectors, say $\mathbf{b}$ and $\mathbf{c}$. So, if we start at vertex A, we can use the barycentric weightings, u and v, to weight our distance vectors and hence describe every point in the triangle, as illustrated in Fig. 9.9. It is noted that because the vectors $\mathbf{b}$ and $\mathbf{c}$ define a plane, the vector $\mathbf{p}$ will be located in the same plane.

By multiplying both sides of Eq. 9.10 with $\mathbf{b}$ and $\mathbf{c}$, respectively, we obtain the following system of equations:

$$\begin{aligned} \mathbf{p} \cdot \mathbf{b} &= u\mathbf{b}^2 + v\mathbf{c} \cdot \mathbf{b} \\ \mathbf{p} \cdot \mathbf{c} &= u\mathbf{b} \cdot \mathbf{c} + v\mathbf{c}^2 \end{aligned} \tag{9.11}$$

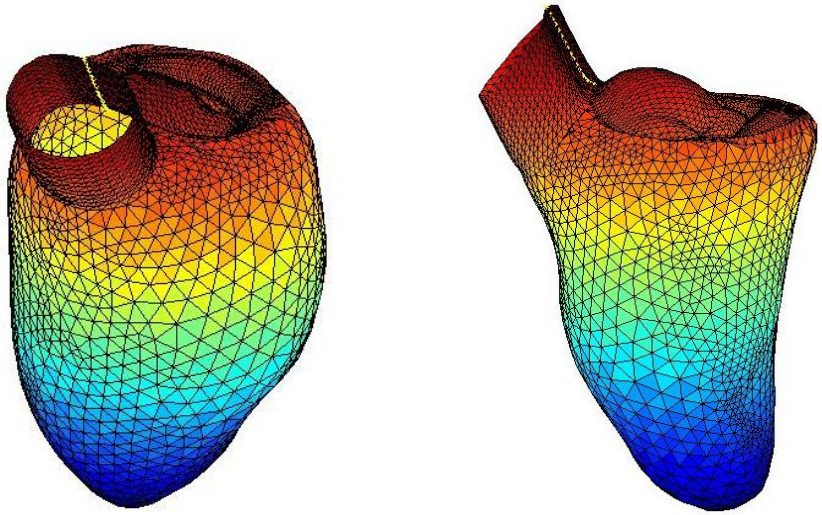

(a) start systole (b) end systole

Figure 9.6: The complete model at start (a) and end (b) of systole

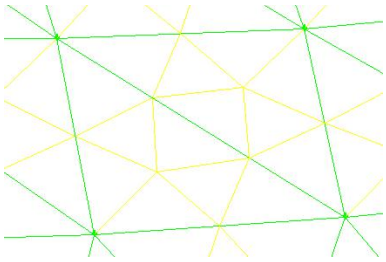

Figure 9.7: LV surface mesh in start geometry. The green cells are the original grid extracted from the echocardiographic recordings, whereas the yellow cells are a result of the grid refinement for the CFD simulation

In matrix form:

$$\begin{bmatrix} \mathbf{p}\cdot\mathbf{b} \\ \mathbf{p}\cdot\mathbf{c} \end{bmatrix} = \begin{bmatrix} \mathbf{b^2} & \mathbf{b}\cdot\mathbf{c} \\ \mathbf{b}\cdot\mathbf{c} & \mathbf{c^2} \end{bmatrix} \begin{bmatrix} u \\ v \end{bmatrix} \tag{9.12}$$

Solving for u and v gives:

$$\begin{aligned} \begin{bmatrix} u \\ v \end{bmatrix} &= \begin{bmatrix} \mathbf{b^2} & \mathbf{b}\cdot\mathbf{c} \\ \mathbf{b}\cdot\mathbf{c} & \mathbf{c^2} \end{bmatrix}^{-1} \begin{bmatrix} \mathbf{p}\cdot\mathbf{b} \\ \mathbf{p}\cdot\mathbf{c} \end{bmatrix} \\ &= \frac{1}{\mathbf{b^2}\cdot\mathbf{c^2}-(\mathbf{b}\cdot\mathbf{c})^2} \begin{bmatrix} \mathbf{c^2} & -\mathbf{b}\cdot\mathbf{c} \\ -\mathbf{b}\cdot\mathbf{c} & \mathbf{b^2} \end{bmatrix} \begin{bmatrix} \mathbf{p}\cdot\mathbf{b} \\ \mathbf{p}\cdot\mathbf{c} \end{bmatrix} \end{aligned} \tag{9.13}$$

When u and v are defined we can use them to decide whether point, P, belongs to this particular cell or not. The three inequalities which decides whether P is located inside the triangle, are summarized

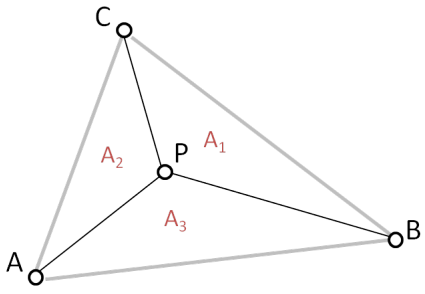

Figure 9.8: The barycentric coordinates of a point P with respect to a triangle can be defined in terms of ratios of triangle areas

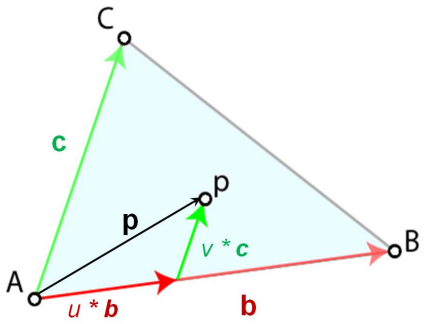

Figure 9.9: The triangle ΔABC with the point P located inside. Starting in vertex A, we can use the barycentric weightings, u and v, to weight our distance vectors, $\mathbf{b}$ and $\mathbf{c}$, to describe point P inside the triangle.

below:

$$\begin{aligned} u &>= 0 \\ v &>= 0 \\ u + v &<= 1 \end{aligned} \tag{9.14}$$

These inequalities are only valid for points P that are situated on the plane defined by ΔABC. Since ΔABC is an arbitrary 2D triangle in the 3D space and P is also an arbitrary point, we need an additional criteria to know whether P is on the plane of the triangle ΔABC or not:

$$f = norm(\mathbf{p} - u \cdot \mathbf{b} - v \cdot \mathbf{c}) \tag{9.15}$$

where f has to fulfill the criterion: $f < 1e^{-5}$

The triangle inclusion test was repeated until all nodes in the refined mesh had found their appurtenant cell and belonging weighting factors in the original grid. For every node, the respective cell number was stored together with u and v. This information was enough to interpolate every nodes' position in all of the following time frames. This third method executed about ten times faster then the two methods based on subareas and was therefore chosen for this study.

9.2.7 Creation of intermediate computational meshes

The segmentation consisted of 27 time frames throughout one cycle. However, further computational meshes were required at intermediate time steps between the initial meshes. The frame to frame variation in shape, dimension and orientation of the LV depends upon its deformity as well as on the frame rate achieved during the recordings. Due to the high temporal resolution, we assume that the moving LV in adjacent frames does not vary significantly during a cycle. Hence, new intermediate meshes was created at every CFD time step by linear interpolation between the segmented LV frames.

The FE MV simulation resulted in 20 times more time frames than the echocardiographic recordings. It was not desirable to reduce the number of simulated FE MV surface meshes to the number of segmented LV surface meshes, because valuable details of the rapid moving leaflets could then be lost. The intermediate computational meshes of the MV and LV were therefore calculated separately by linear interpolation within each object's original surface meshes.

9.3 Results

To illustrate the correlation between the model and the echocardiographic recordings, the model is realigned with the original echocardiographic data. The LV is placed back at the same position as when it was segmented in AutoLVQ. The alignment is showed in Fig. 9.10. (a) and (b) are from start and end systole, respectively, where the red line is the original AutoLvq and the yellow line is our model. (c) and (d) illustrates the cut plane from two different views in start systole, the selected plane approximately intersects the middle of the outflow tract. Here, we only demonstrated the similarity during systole because the FE MV model is, at present, not available for the diastole. However, the combined model with the annulus and LVOT exists for the entire cardiac cycle.

The endo contours generated using AutoLVQ, nicely follows the inner wall of the LV throughout the cycle. The papillary muscles and major trabeculae were included in the cavity and can be seen at the inside of the generated endo contours in Fig. 9.10, particularly at the posterior side of the LV cavity.

A reasonable match is obtained between the modeled LVOT and the endocard throughout systole, however a small deviation from the aorto-mitral-curtain can be seen. This is because the aorto-mitral-curtain was traced in every time frame, while a curvature representing the average of all frames was utilised in the model. This can be improved by using the complete transient tracing of this wall.

The shape of the modeled MV is altered compared to the subject's healthy MV. This is because the purpose of our first 3D study is to investigate how various leaflets' shape affect the systolic flow behavior. Different types of billowing leaflets will therefore be included in the model. This will be explained further in the discussion.

The size of the FE mitral annulus is slightly too large for the subject's ventricle in start systole, while the size is approximately correct in end systole. This deviation is expected since the annulus in the FE model is fixed whereas the real annular area slightly changes during systole. However, a compliant annulus will be included in future models. Some misalignment is also present at the basal posterior side of the ventricle at the anchoring of the mitral annulus in end systole, Fig. 9.10 b).

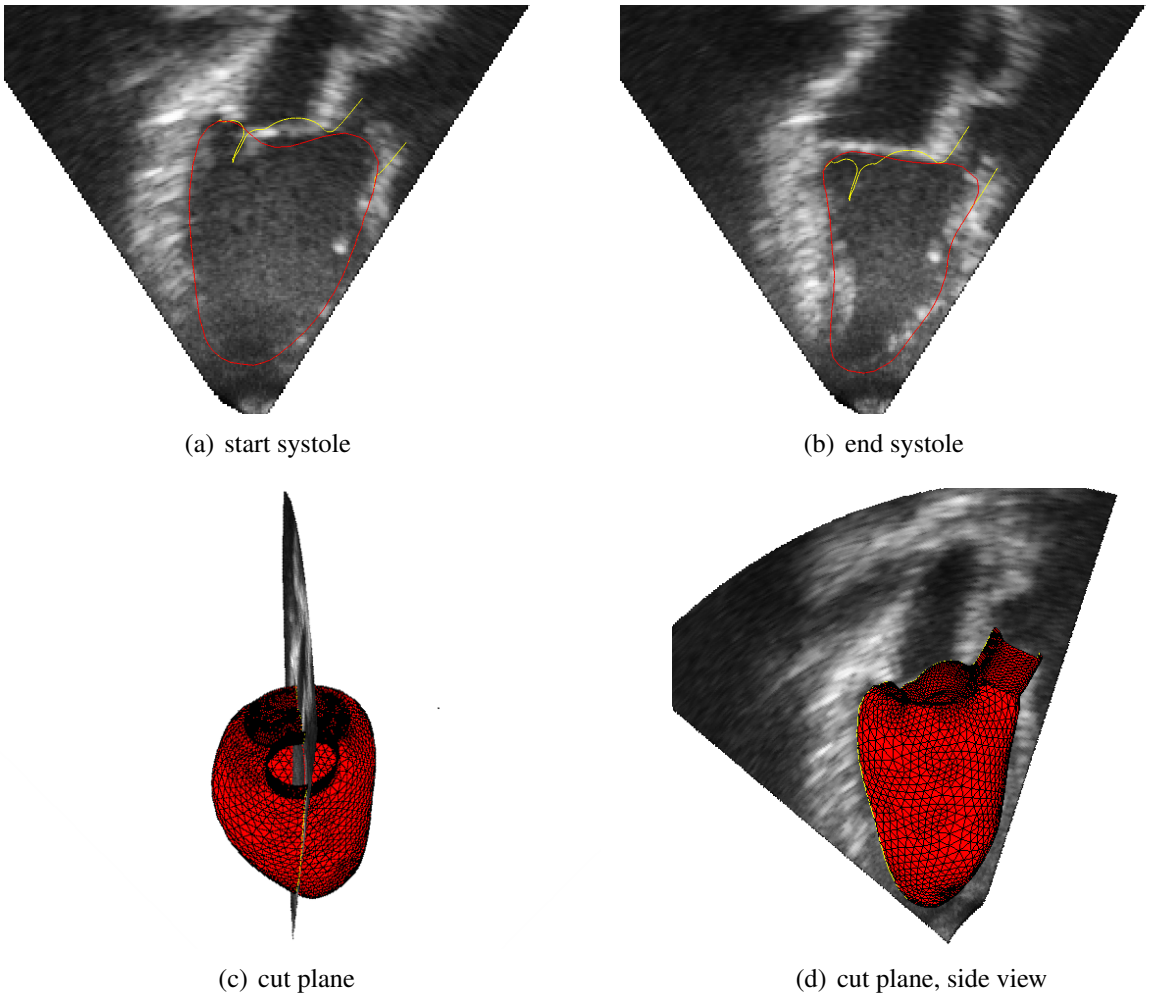

(a) start systole (b) end systole

(c) cut plane (d) cut plane, side view

Figure 9.10: The 3D model is realigned with the original echocardiographic data. (a) and (b) are start and end systole, respectively, where the red line is the original AutoLVQ and the yellow line is our model. (c) and (d) illustrates the selected plane where the 3D model was cut, (d) is rotated 90 degrees compared to (c).

9.4 Discussion

In this paper, we present a technique for the creation of 3D moving boundary conditions, from RT3DE to CFD simulations. Due to the strong dependency of flow characteristics on the LV geometry and motion, the accuracy of the 3D-geometry is a key factor in numerical simulations of the intraventricular flow. The semi-automated tool (4D Auto LVQ) for volume measurements in RT3DE gives rapid and reproducible measurements of LV volumes [46] and has a great potential as the basis for patient specific CFD models. RT3DE is gaining popularity as a routine clinical tool, which means that there will be easy accessible patient data in this format in the future. Good correlations for LV volumes and ejection fractions between RT3DE and MRI have been reported [72], although it is well known that there is a systematic bias between RT3DE and MRI volume measurements where echocardiography generates smaller volumes when compared to MRI. Moreover it has been shown that RT3DE is more

accurate than 2D echocardiography for measuring LV parameters [51].

When comparing the current study with the ones relying on MRI for anatomic model generation, one has to keep in mind the fundamental differences between these acquisition modalities. RT3DE has the advantage of being a real-time 3D modality, the entire dataset being acquired in 3 up to 6 heart cycles, with instantaneous full-volume imaging currently under development [1]. One important advantage of echocardiography is the clear visualization of the cardiac valves, which are often less distinguishable in MRI due to the high signal from blood. However, echocardiography yields larger inter-subject variation in image quality and the size of the LV also affects the image acquisition. At present, the average temporal resolution in 3D echocardiography is in the range of 25-50 frames per second (fps) in an average size LV, however recordings with resolution up to 60 fps have been reported. In the case of MRI, the balanced steady-state free precession sequence is most commonly used for LV imaging. A series of 2D short- and long- axis image planes are acquired (15s/image plane) with ECG gating. The sequence gives excellent blood-myocardium contrast, with a temporal resolution of 25-50 fps, and a spatial resolution of approximately 1-1.5 mm in plane and a slice thickness of about 6-8 mm. Due to long acquisition times MRI data can be corrupted by failure to hold breath, which will result in image artifacts. Furthermore inter-slice alignment errors are typically caused by different diaphragm positions in each breath hold.

To make a subject-specific 3D CFD model of the pumping LV which also includes a MV model and an outflow tract, some user interventions are required. The presented approach is semi-automatic, i.e. some manual work are required in the start frame, while the rest of the frames are automatic adjusted based on given parameters. The 4D Auto LVQ segmentation moves the tracking points perpendicular to the endocardial surface so the LV area and the cells increase or decrease according to the LV volume. However, if a cell is defined at ED and the actual myocardium moves tangentially to the surface, i.e. rotation, twisting, the segmentation algorithm ignores that motion. As a result at ES, the same cell does not represent the same part of the myocardium. In our model, the MV and the LVOT were positioned at the LV base by removing the same cells in all frames. The base typically rotates no more then 4-5 degrees [92], so it is a reasonable approximation to assume that the myocard follows the cells in this part of the LV.

There does not exist any trivial procedure of extracting the geometry and time dependent shape of the valve leaflets from echocardiographic recordings. Manual tracing is, today, the only alternative and is highly time consuming. In this study, the MV was represented by a 3D FE model, where the annulus had been measured at early systole in 3D echocardiographic images of the heart of an anaesthetized pig. The size and shape of the annulus in pigs are somewhat the same as in humans. The annulus in the subject's recordings was approximately the same as in the 3D FE model, hence, it was not necessary to scale the FE MV model to the recorded LV model. The purpose of including a FE MV model is the simplicity of altering the valve in various ways, i.e. cutting different chordaes, vary the degree of muscle activation [103] etc, to see how this affect the fluid flow. Also, the degree of leaflet billowing can be subsequently adjusted in the prescribed CFD model. The FE valve presented in this paper, is altered compared to a healthy valve. Therefore, the shape of the valve in Fig. 9.10 does not follow the healthy subject's valve.

A preliminary CFD simulation of the 3D model is provided in Appendix A. As a first step for validation of the CFD model, the predicted blood flow in the LVOT were compared with in-vivo MRI flow measurements. The MRI measurements were obtained in the same heart and at the same day as the RT3DE recordings.

9.4.1 Limitations

The papillary muscles are included in the cavity during the tracing. The effect of the papillary muscles on the fluid, will therefore be excluded in the simulation. However, their significant influence on the deformation of the LV during systole, when they contract and possibly contributes to the longitudinal shortening of the LV, are included because of the prescribed deformation.

The LV torsion about the LV central axis, is not included in this first model. However, a segmentation algorithm which follows material points and hence accounts for the LV torsion, are under development and will be included in future models.

9.5 Conclusions

A technique for the creation of subject-specific 3D moving boundary conditions, from RT3DE to CFD simulations, has been presented herein. One benefit of the presented approach, is the simplicity of using replaceable parts. The software is capable of incorporating different models of either the MV, the LVOT or the LV, with a limited amount of user intervention. One of the great advantages with CFD models is the opportunity it gives to easily alter the models and further check how the flow responds to the applied changes. This means that subject-specific heart models have the potential to support professionals in clinical decision-making by performing ”virtual surgery”. By doing this, new insight to the influence of surgical intervention on the blood flow, can be obtained. However, before a model can be used for clinical purposes, thoroughly validation is necessary.

Appendix A

Impact of the mitral leaflets' curvature on flow dynamics during left ventricular contraction: An initial study

The 2D study in this chapter is based on Dahl and Skallerud (2010). **Effect of mitral valve shape on flow dynamics during left ventricular contraction**, *6th World Congress on Biomechanics; Singapore, 1-6 August 2010.*

A.1 Background of the study

The mitral valve (MV), also called the bicuspid valve, separates the left atrium (LA) and the left ventricle (LV). The valve consists of two leaflets with significantly different geometries, this is the anterior and the posterior leaflet. The leaflets are anchored to the mitral annulus and attached to the inner wall of the LV via a series of strings called chordae tendineae. The valve assures unidirectional blood flow between the two chambers. When the atrial pressure exceeds the ventricular pressure during diastole, the soft leaflets comply and fold into the ventricle, allowing blood to pass freely. When the ventricle starts to contract, the leaflets close immediately, preventing blood from flowing into the LA.

A normal, healthy mitral valve billow slightly into the left atrium during ventricular contraction [12]. There are two major components contributing to the leaflets' curvature. The first, and most obvious, is various degrees of leaflet billowing, the second, and more subtle, is the annular saddle shape [95]. The slightly billowing leaflets and the annular nonplanarity act together to optimize leaflet curvature and thereby reduce the mechanical stress in the mitral leaflets [5, 95]. But, are there any hemodynamic benefits of having only a slightly curved valve? As far as the authors know, there are no studies concerning the hemodynamic consequences of various leaflet curvatures during ventricular contraction.

Changes in leaflet curvature might occur due to MV pathology or surgical interventions. However, one of the most common heart valve abnormalities is that one or both valve leaflets are bulging more than normal into the atrium during systole. Such abnormalities are often lumped together in the term *billowing mitral leaflets* or *BML*. For BML, edge coaptation is functionally normal. BML is frequently diagnosed in healthy people, and is, for the most part, harmless. If the BML progresses, failure of edge apposition may supervene and mitral regurgitation occurs, the condition is then called mitral valve prolapse (MVP). Echocardiography is the most useful method of diagnosing the mitral valve. Echocardiography identifies and assesses the extent of billowing, but there are no specific echocardiographic criteria that can differentiate normal from pathological billowing [12]. We want to investigate whether there are any hemodynamic effects of different types of BML which might induce long-terms effects or can trigger pathological change. For example, an altered hemodynamic pattern can cause adverse wall shear stresses (WSS) and further remodeling of the valves and/or vessel wall.

Heart valves are active structures that respond to altered load patterns by remodeling [44]. Although remodeling may be initiated as adaptations to altered loads, the resulting valve tissues may not be able to provide normal long-term function. Because valve tissue has this ability to remodel, the relationship between the valve geometry, the tissues microstructure, material properties and loading environment is interdependent.

In a majority of the papers regarding hemodynamics in the LV, MRI has been used to extract the transient geometry. MRI has a clear advantage with respect to image quality, but the cardiac valves are often less distinguishable due to the high signal from blood. One particular strength of echocardiography, on the other hand, is the clear visualization of the cardiac valves. But, due to their rapid movement, the time-dependent shape of the leaflets is not easily extractable. There does not exist any automatic tool for valve segmentation, thus, manual tracking is the only alternative available today. Due to its ability to identify valve structures, echocardiography was chosen as imaging modality in this study.

A better understanding of the valve's impact on the flow pattern can provide practical insight that may facilitate the diagnosis and treatment of pathological or abnormal mitral leaflets. The aim of this

study is to investigate the influence of different valve curvatures on the systolic flow field. In this appendix some preliminary results are provided. We have taken a two-step approach, with a 2D study first in order to investigate on simple models what types of influence that might occur (see A.2). Also, it is easier to interpret 2D results and learn from these before we carry out the second step, i.e. 3D analyses. The first objective in our 3D analyses was to perform a 3D computational fluid dynamics (CFD) simulation which could provide results within the physiological range. Results from this first 3D simulation and the subsequent validation are provided in section A.3.

The preliminary 2D and 3D studies have indicated some important new results that should be further investigated. This is discussed in the further work section (see A.5) at the end of this appendix.

A.2 2D study

Two 2D models were analyzed, the models were distinct when it came to the curvature and motion of their mitral leaflets. The results indicate that the flow pattern in the vicinity of the leaflets and particularly in the aortic outflow tract is affected by the valve curvature. The first model, m_I, represents a normal, healthy valve, while the second one, m_{II}, imitates a valve with a billowing and irregular curvature.

A.2.1 Models and method

To obtain subject-specific boundary conditions, 2D echocardiographic recordings of a young healthy adult were performed. The recordings were performed in the long-axis view because this plane represents both the mitral and aortic valve (AoV) in addition to the LV. Fig. A.1(a) illustrates the different transducer orientations used for recordings in the long-axis view. The time-dependent geometry of the LV was rendered in the apical long-axis view by the speckle tracking option of EchoPAC PC (version 6.0.0, GE Vingmed Ultrasound, Norway).

The prescribed movement of the normal, healthy leaflets in m_I were reconstructed from the same subject as the LV wall. To obtain a clear view of the MV, the parasternal long-axis view was utilized for these measurements, see Fig. A.1 (a). The speckle tracking algorithm is not able to follow the rapidly moving leaflets, therefore, an in-house software was written for this purpose. The transient 2D valve profile could now be extracted from the echocardiographic recordings. Fig. A.1 (b), shows a recorded image in which the MV has been traced (red line). As seen in Fig. A.1 (b), the normal, healthy mitral leaflets appear almost flat during peak systole. The MV was traced from the onset of Aov opening to AoV closure.

The irregular shaped leaflets in m_{II} were reconstructed from an advanced 3D finite element (FE) model of the MV. A transient simulation of the FE model in Abaqus, provided us with the time-dependent history of the valve during systole [84, 85]. This is the same 3D FE MV model as implemented in the 3D LV model presented in Dahl *et al.* [26] (see chapter 9).

In Fig. A.2(a), m_I and m_{II} are plotted on top of each other at peak systole to illustrate the difference in valve curvature. Both the anterior and the posterior leaflet are bulging more in m_{II} than in m_I. The coaptation zone is also tilted towards the posterior side in m_{II}. In Fig. A.2(b), the geometry of m_I at the onset of AoV opening and at AoV closure are plotted in the same figure to illustrate the movement of both the LV wall and the mitral leaflets during this period.

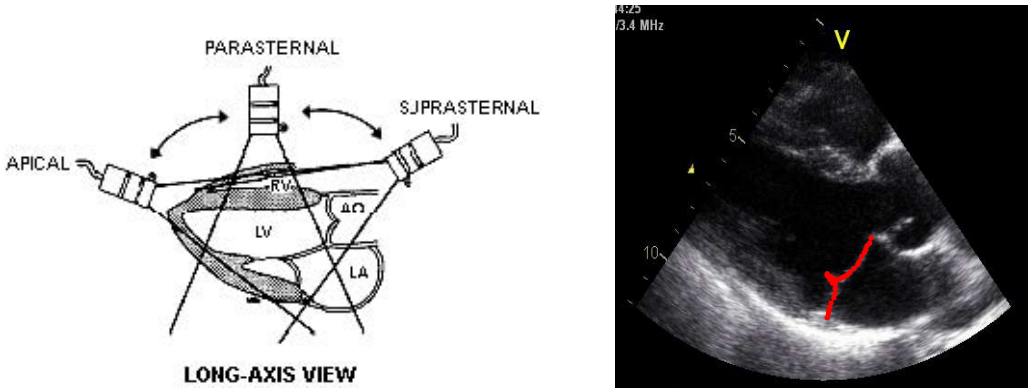

(a) (b)

Figure A.1: The three transducer orientations used to record the long-axis view is illustrated in (a). The apical view was used for the LV wall geometry, whereas the parasternal view was utilized for the MV as seen in (b). Tracking of the mitral valve at peak systole is shown with a red line in (b). The normal, healthy mitral leaflets appear almost flat during peak systole.

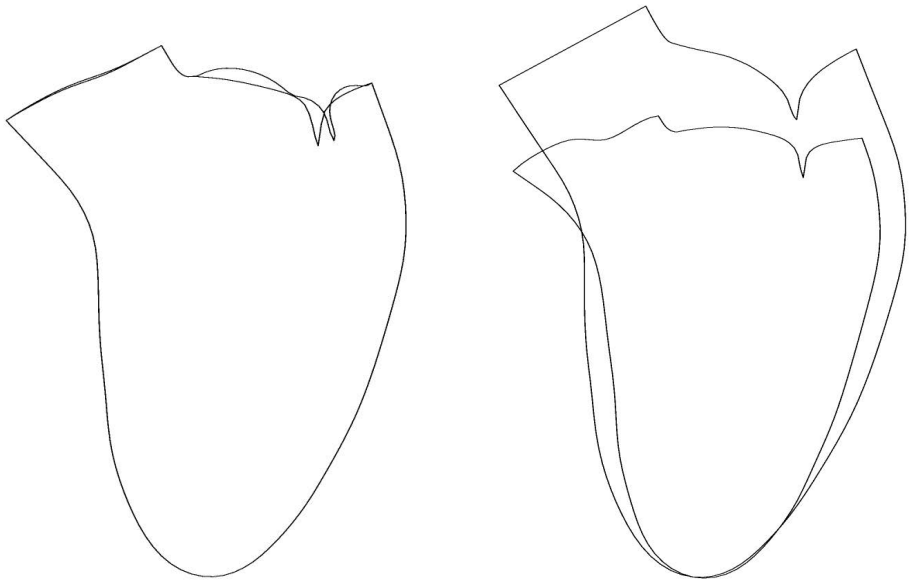

(a) (b)

Figure A.2: In (a), the two models are plotted on top of each other at peak systole to illustrate the difference in valve curvature. Both the anterior and the posterior leaflet in m_{II} are bulging more than in m_I. The coaptation zone is also tilted towards the posterior side in m_{II}. In (b), the geometry of m_I at AoV opening and at AoV closure are plotted in the same figure to illustrate the systolic movement in this period.

In our simulations, the prescribed wall motions will drive the flow. The numerical simulations were performed with the finite-volume CFD software Fluent 6.3.26 (Ansys Inc.). The arbitrary Lagrangian-Eulerian (ALE) formulation was used to express the Navier-Stokes equations on the moving grid. Due to the large deformations of the fluid domain, remeshing was also necessary. Laminar

flow was assumed and the blood was modeled as an incompressible, Newtonian, homogenous fluid, with a density of ρ = 1050 kg/m^3 and a viscosity of $3.5 \cdot 10^{-3}$ kg/ms. A no-slip condition was applied at the walls. The 2D simulations start from the onset of AoV opening and end at AoV closure, i.e. the isovolumetric contraction in start-systole is not included in our simulations. The total length of this period was measured in the echocardiographic recordings to be 272ms.

A.2.2 Results and discussion

Fig. A.3 shows the velocity vectors at peak systole, 60ms after AoV opening, for m_I and m_{II}. Due to the 2D limitation, the velocity scale is out of the physiological range and therefore not included. Only qualitative information can be extracted from the simulated 2D results.

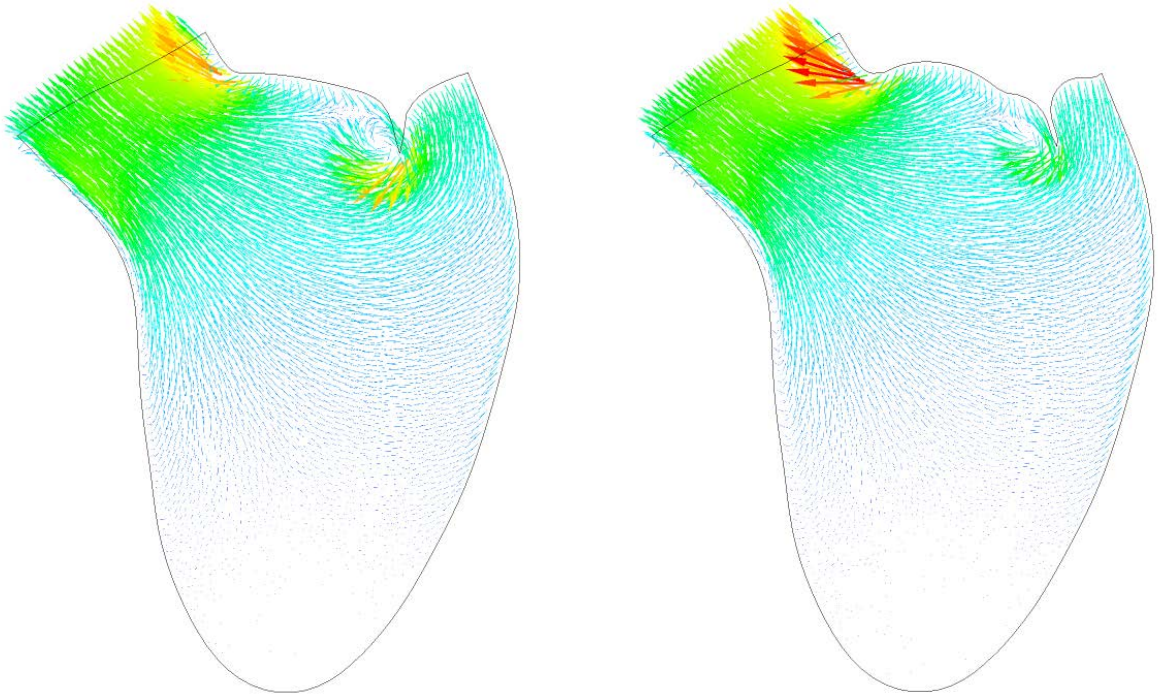

(a) m_I (b) m_{II}

Figure A.3: Velocity vectors at peak systole for m_I and m_{II}, respectively. The velocity as the blood flows around the mitral annulus-aorta junction is higher in m_{II} than in m_I. A vortex has started to develop at the leaflets' tip in both models. The velocity scale is out of the physiological range due to the 2D limitation and therefore not included.

When a fluid flows through a narrower cross-section, the fluid velocity must increase to maintain the mass flow rate. As the blood flows into the left ventricular outflow tract (LVOT), the cross-sectional area decreases considerably and hence, the velocity increases (Fig. A.3). The transition from the LV to the LVOT is smoother at the septal side than at the mitral side for both models. At the mitral side, the blood has to flow around the mitral annulus-aorta (Ma-Ao) junction before it enters the LVOT and hence, higher velocities will occur in this area for both m_I and m_{II}. The velocities are also higher in m_{II} than in m_I because of a higher degree of anterior leaflet billowing in m_{II}.

As the blood rounds the Ma-Ao junction, the velocity vectors are pointing more towards the central axis of the LVOT than along the wall. This will disturb the blood ejected from the rest of the ventricle and perhaps make the ejection less efficient. This effect is more prominent in m_{II} because the billowing anterior leaflet forces the blood to round a sharper corner in m_{II} than in m_I. Hence, the degree of anterior leaflet billowing might affect the efficiency of ventricular ejection.

As seen in Fig. A.3, a vortex has started to develop at the tip of the leaflets' coaptation zone in both models. This is probably due to the sharp edge pointing into the fluid domain. If the tip of the leaflets' coaptation zone will have the same effect in a 3D simulation has to be investigated further.

Our preliminary 2D results suggest that the degree of anterior leaflet billowing affects the velocity pattern in the outflow tract during ventricular contraction. According to our observations, a slightly billowing anterior leaflet creates a more efficient ejection with lower peak velocities than is the case for a more billowing anterior leaflet. The results presented here are two-dimensional whereas the real human heart flow is a characteristic three-dimensional vortical flow. The investigated 2D models cannot simulate the real fluid dynamics during ventricular contraction. Nevertheless, the model interpretations regarding the impact of the anterior leaflet on the aortic flow profile is interesting and should be investigated further.

A.3 3D study

The first objective in our 3D study was to perform a CFD simulation of the 3D model presented in Dahl *et al.* [26] (see chapter 9). Second, to do an initial validation of the preliminary results to see whether the simulated velocities were within the physiological range. The final aim is to use the 3D model to complete the proposed study of the impact of the leaflets' curvature on the systolic flow pattern. This is not included in this thesis, but discussed in the further work section (see section A.5).

A.3.1 The 3D model

For this study we wanted to use the previously developed subject-specific 3D model of the LV presented in Dahl *et al.* [26] (see chapter 9). In this 3D model, the time-dependent ventricular geometry was rendered from real-time 3D echocardiography (RT3DE) by using the semi-automated tool (4D AutoLVQ) on an EchoPAC software workstation (version BT 11, GE Vingmed Ultrasound, Norway). The segmentation provided a closed 3D triangular surface mesh for every time frame throughout the cardiac cycle. Due to the difficulties of tracking the time-dependent shape of the MV from RT3DE, an advanced 3D FE MV model [84, 85] was used to obtain the basic 3D characteristics of the MV geometry. The FE MV model was then incorporated in the original segmented LV grid topology.

Fig. A.4(a) and (b), shows the geometry of the combined 3D model at start- and end-systole, respectively. The triangular LV surface mesh is the original mesh from the segmentation data. Fig. A.4 (c) shows the 3D model when it is realigned with the original echocardiographic data. A reasonable agreement between the modeled geometry and the RT3DE data was obtained.

A.3.2 Modification of the FE MV model

Before a CFD simulation can be performed, a good quality volume mesh of the 3D model has to be generated. However, due to sharp edges and small gaps in the complex FE MV geometry, it was

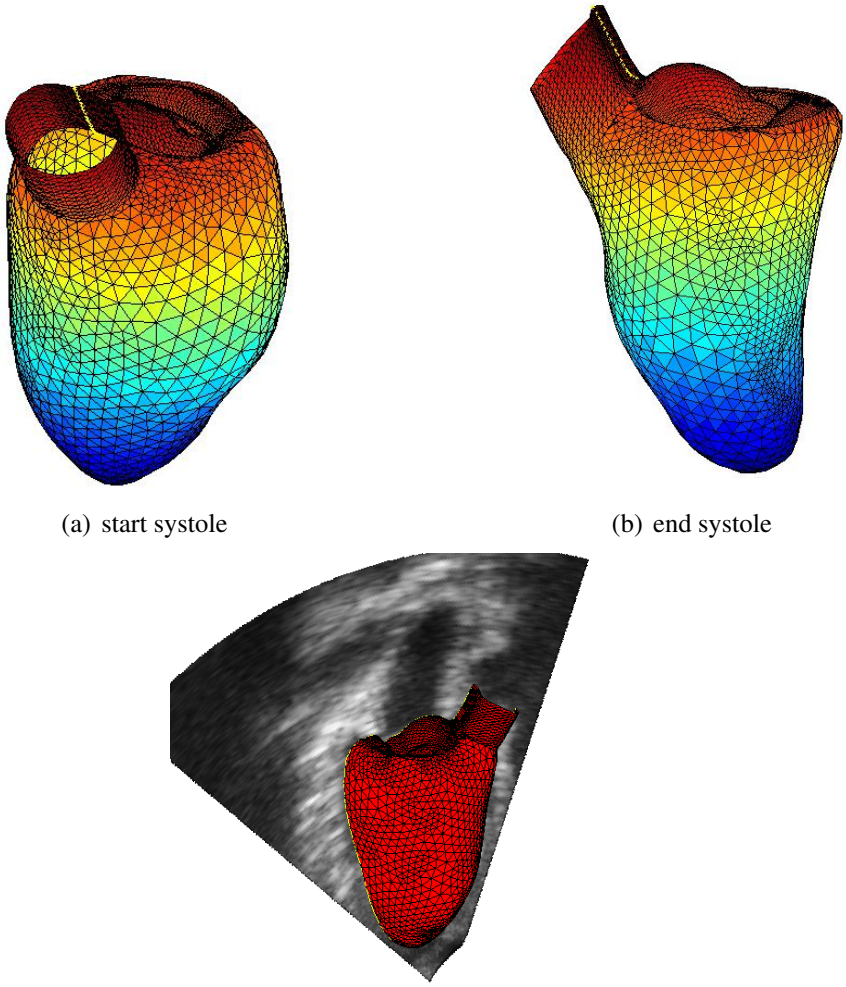

(a) start systole

(b) end systole

(c) The model realigned with the echocardiographic data at start systole

Figure A.4: The LV model at start (a) and end (b) of systole, whereas (c) shows the 3D model realigned with the original echocardiographic data.

not possible to obtain a proper volume mesh of the model shown in Fig. A.4. In addition, the MV geometry was difficult to modify to different curvatures as it appeared in the FE simulations.

The solution was to remodel the FE MV geometry by using topographic mapping. A topographic map is a detailed and accurate 2D representation of a 3D geometry, where each of the 2D points contains vertical information. By using topographic mapping, a continuous and smoother MV geometry can be obtained, while the main topology of the valve is conserved. The projection plane used for the topographic map of the FE MV model was chosen to give a best possible capturing of the 3D geometry. The map was generated using 40000 points and then smoothed. Fig. A.5 shows the topographic map of the FE MV model before and after smoothing. The vertical information is illustrated by colors.

To create the new discretized 3D model of the MV, a set of nodes was evenly distributed at the map's surface as illustrated in Fig. A.6(b). The underlying 2D function, which contains the vertical

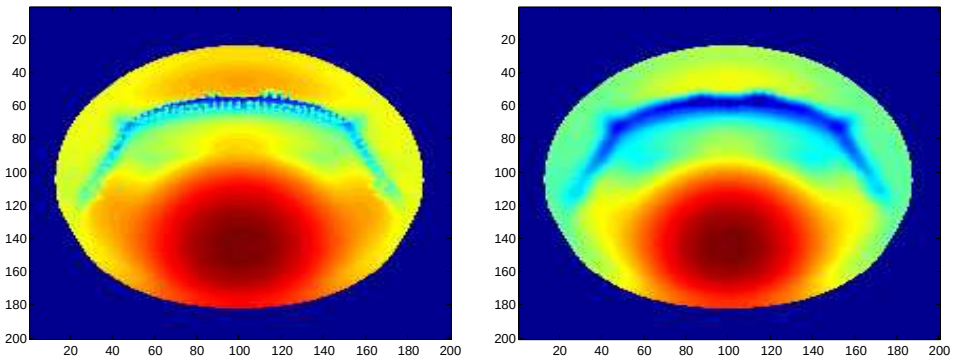

(a) Before smoothing (b) After smoothing

Figure A.5: (a) and (b) illustrate the topographic map of the FE MV model before and after smoothing, respectively. The vertical information is illustrated by colors.

information in the map, was interpolated to find the Z-value for each of the new nodes. The elements were then created by using Delaunay triangulation. Fig. A.6(a) shows the MV model as it appear in the FE simulations, Fig. A.6(b) illustrates the topographic map with the new set of nodes and Fig. A.6(c) shows a cross-sectional profile of the new modified MV model. As seen in Fig. A.6(c), the valve profile is now smooth without sharp edges and gaps.

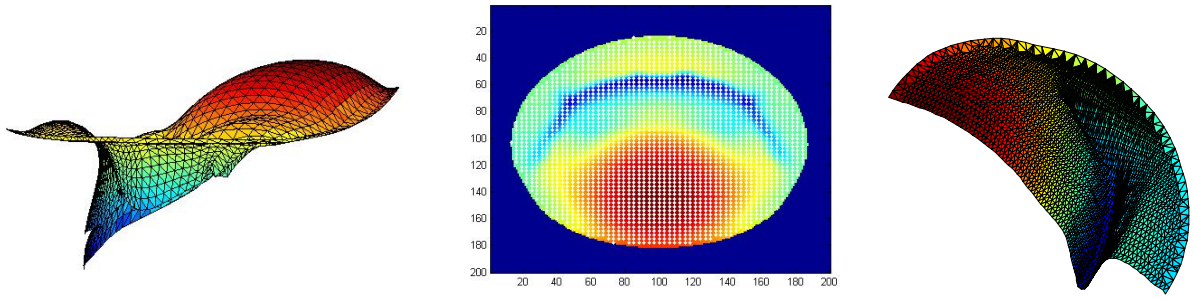

(a) FE MV model (b) The new nodes plotted in the topographic map (c) New modified MV

Figure A.6: (a) shows the MV model as it appear in the FE simulations, (b) illustrates the topographic map with the new set of nodes and (c) shows a cross-sectional profile of the new MV model.

The modified MV model was positioned at the LV base with the technique described in [26] (see chapter 9). The new 3D model is shown in Fig. A.7 (a) and (b) at two different times during systole. Fig. A.7 (c) shows the model from an atrial view where the mitral ”smiley” is clearly visible.

A volume mesh with an acceptable mesh quality was now possible to obtain. A total number of 139167 tetrahedral cells were used in this first preliminary CFD simulation. However, it is assumed that a finer mesh is needed to achieve mesh convergence. A mesh convergence test was not performed in this initial study, but a convergence test is required before further studies are performed.

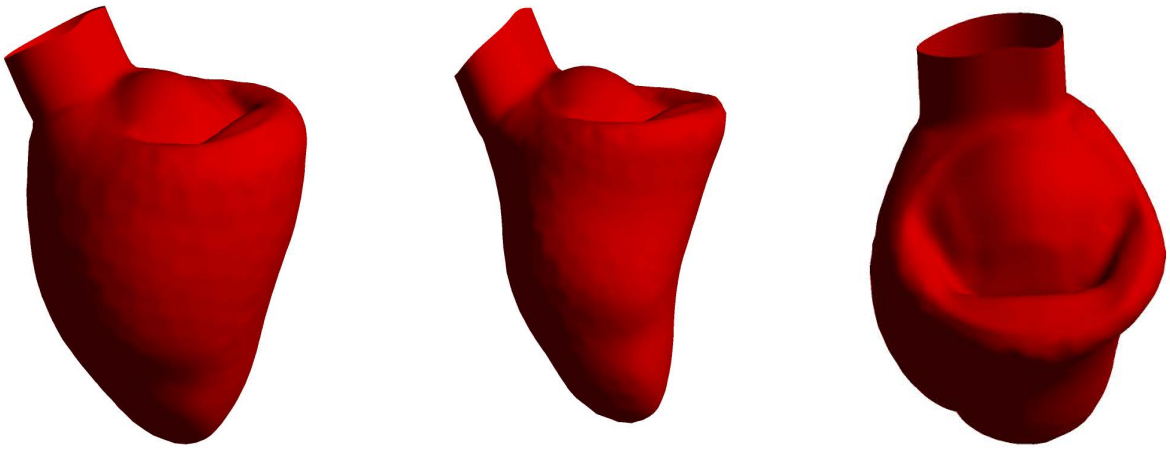

(a) Start systole (t=0ms) (b) 200ms from AoV opening (c) The mitral "smiley" at 200ms

Figure A.7: The figures illustrate the complete model of the LV with the new MV geometry. Figure (a) is from start systole, whereas (b) is from 200ms into the simulation, i.e. from AoV opening. Figure (c) shows the model from an atrial view, where the mitral "smiley" is clearly visible.

A.3.3 Numerical model

The flow simulations were performed using the commercial finite volume package Ansys Fluent 13.0 (Ansys Inc.). The CFD solver was extended with dedicated user defined functions (UDFs) in order to include the systolic movement of the LV, the LVOT and the MV in the simulations. The prescribed wall motions will drive the flow.

The ALE formulation was used to express the Navier-Stokes equations on the moving grid. To update the entire volume mesh, both spring-based smoothing and local remeshing were necessary. Local remeshing was required because the boundary displacements in our model were large compared to the local cell sizes in the applied mesh. Without remeshing, this might deteriorate the cell quality and lead to convergence problems during the simulation. By applying local cell remeshing, the cells that violate the skewness or size criteria will be remeshed when going to the next time step. An additional option available in Ansys Fluent 13.0, called sizing function, enables the fluid solver to also mark cells for remeshing based on a given size distribution. In our model, the size function was necessary to avoid negative cell volumes and hence an invalid mesh.

The simulation starts from the onset of AoV opening and ends at AoV closure in end-systole, i.e. the isovolumetric contraction in start-systole is not included in this simulation. The length of the systolic period, from AoV opening to Aov closure, was 285ms and given from the RT3DE recordings. Laminar flow was assumed. The blood was modeled as an incompressible, Newtonian, homogenous fluid, with a density of ρ = 1050 kg/m^3 and a viscosity of $3.5 \cdot 10^{-3}$ kg/ms, which are reasonably good approximations for blood flow in large cavities [61]. A no-slip condition was imposed at the walls.

A.3.4 Preliminary results and discussion

Fig. A.8 illustrates the velocity field in a long axis view at two different times during systole. The first column illustrates the velocity field by velocity contours, the second column illustrates the corresponding velocity field by vectors. Fig. A.8 (a) and (b) are from peak systole; 75 ms after AoV opening. Fig. A.8 (c) and (d) are from the last part of systole; 200 ms after AoV opening.

At peak systole, the maximum velocity at the outlet is 1.19 m/s, however, the highest velocity in the domain is 1.25 m/s and occurs as the blood rounds the Ma-Ao junction (Fig. A.8 (a) and (b)). The mass flow rate decreases towards the end of systole. At 200 ms is the maximum velocity at the outlet and at the Ma-Ao junction reduced to 0.68 m/s and 0.69 m/s, respectively (Fig. A.8 (c) and (d)).

As observed in Fig. A.8 (a) and (c), a region of high velocity moves from the mitral side in the beginning of the LVOT and towards the anterior-septal side further downstream of the LVOT. The skewness of the velocity field in the LVOT is most prominent at peak systole. However, the skewness persists towards the end of systole.

Fig. A.9 shows the velocity distribution in the outflow tract at three different cross-sections during peak systole. In Fig. A.9 (a-c), the ventricular septum is towards the bottom and the mitral valve towards the up. Fig. A.9 (d) shows the locations of the three planes, where plane 1 is the plane closest to the LV. The velocity profile in Fig. A.9 (a) is significantly skewed with the highest velocity occuring at the mitral side. In the profiles further downstream are the maximum velocity lower and the velocities more evenly distributed, however, the velocity profiles are still skewed (Fig. A.9 (b) and (c)). In Fig. A.9 (b), the region with the highest velocity is almost covering the mitral half of the opening. In Fig. A.9 (c), this region has moved to the anterior-septal side where it also covers a larger part of the opening. The grid resolution in the LVOT should be refined in future simulations. The flow profiles shown in Fig. A.9 might be affected by such adjustments.

In our 3D model, the anterior leaflet is bulging more than in a normal valve (see Fig. A.1 (b)). The degree of anterior leaflet billowing is therefore more like the one modeled in m_{II} than in m_I (Fig.A.3). According to our 2D simulations the velocity as the blood rounds the Ma-Ao junction becomes higher with a more billowing anterior leaflet. We therefore assume that if the anterior leaflet had been flatter at peak systole, the velocities had been lower around the Ma-Ao junction and the flow in the LVOT had been less skewed.

The blood ejected out of the LV is deflected as it enters the outflow tract. At the septal side, the blood flow follows the wall quite nicely, but this is not the case at the mitral side. As the blood rounds the Ma-Ao junction, the velocity vectors are pointing more towards the central axis of the LVOT than along the wall. The blood flowing from the area beneath the anterior leaflet and into the LVOT will interfere with the blood ejected from the rest of the ventricle. According to our 2D results, this will be less pronounced if the anterior leaflet is bulging only slightly into the atrium. Hence, the results might indicate that the degree of anterior lealet billowing affects the efficiency of ventricular ejection.

There are several factors that might also influence the jet ejected out of the LV like the ventricular-aortic root angle, LV function, aortic function etc. Further studies are needed in order to address the impact of the most important factors on the aortic flow pattern.

In both of the 2D models, a vortex started to develop at the tip of the leaflets' coaptation zone. This was not observed in the 3D case.

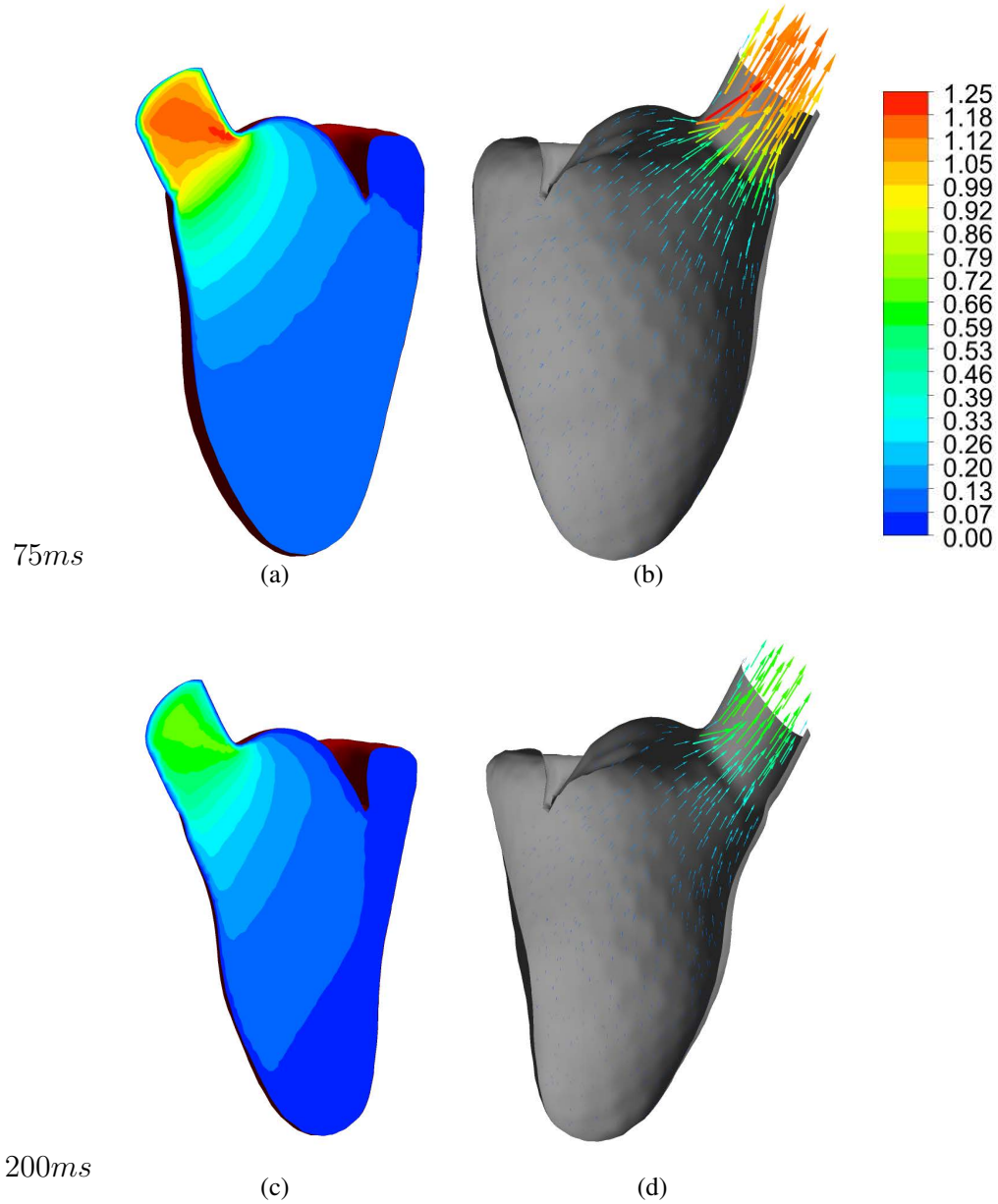

Figure A.8: Fig. A.8 illustrates the velocity field in a long axis view at two different times during systole. The first column illustrates the velocity field by velocity contours, the second column illustrates the corresponding velocity field by vectors. (a) and (b) are at peak systole; 75 ms after AoV opening. (c) and (d) are from the last part of systole; 200 ms after AoV opening. The velocity is given in m/s.

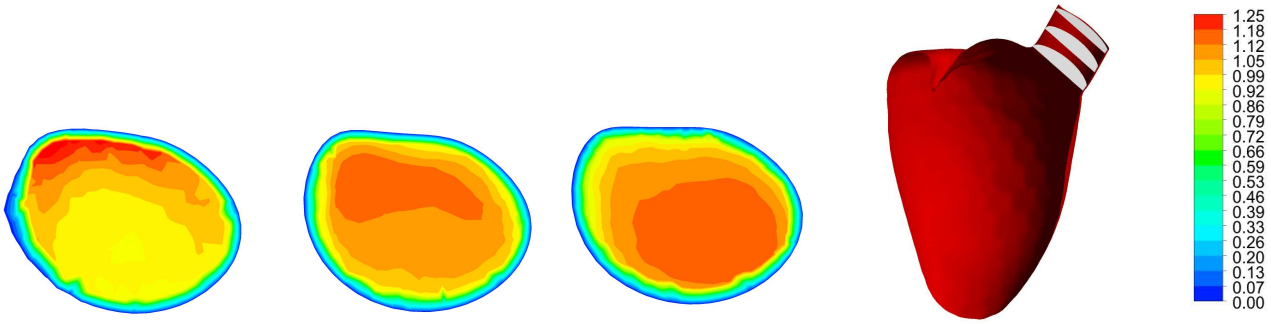

(a) plane 1 (b) plane 2 (c) plane 3 (d)

Figure A.9: The velocity contours at peak systole, 75 ms after AoV opening, at three different cross-sections in the LVOT. Figure (d) illustrates the locations of the three planes, where plane 1 is the plane closest to the LV. The velocity is given in m/s.

A.3.5 In-vivo validation

To control whether the CFD model provides results within the physiological range, some validation is necessary. An initial validation of the simulated velocities was performed by comparing the results with flow measurements obtained from MR phase mapping scans.

The MRI acquisitions were taken at the same day and in the same subject as the RT3DE acquisitions used for the 3D model. In the MR data, peak systole occurred 99 ms after AoV opening and the maximum velocity out of the aortic valve was measured to 1.14 m/s. In the simulation, peak systole occurred 75 ms after AoV opening with a maximum velocity of 1.19 m/s at the outlet. Hence, the simulation gave 4% higher velocities at the aortic outlet than measured in the MR data.

The maximum velocities at peak systole, cannot be directly compared between the simulation and the MR data. There are several reasons for this. One is the difference in heart rate (HR) between the MRI and RT3DE acquisitions. For the MR flow measurements, a HR of 41 was obtained. In the echocardiographic recordings, the HR was 62. Changes in HR are associated with complex autoregulatory responses (sympathetic/parasympathetic impulses), leading to changes in stroke volume (SV) [118, page 231]. Thus, one cannot expect the SV obtained with MR at HR = 41 to be directly comparable to SV obtained with RT3DE at HR = 62. Consequently, the maximal velocities obtained with MR and RT3DE cannot be expected to be equal either. The time when peak systole occurs will also differ when the HR are not the same. In the MRI recordings, the time from AoV opening to AoV closure was approximately 400ms and peak systole occurred after 99 ms. In the echocardiographic recordings,the AoV was open for 285 ms, whereas peak systole occurred at 75 ms after AoV opening. However, the ratio of the time when peak systole occurred to the total time the AoV was open, was approximately the same. The ratio was 0.26 and 0.25 for the simulation and MR data, respectively.

In addition to the heart rate, the flow pattern might also change from one heart beat to another. The blood flow pattern at the time the velocity measurements were done is therefore not necessarily identical with the flow pattern in the recordings used for LV volume segmentation. This might also cause an offset between the measurements and the simulation results.

One important factor to consider is that two different imaging modalities have been used. There is a systematic bias between RT3DE and MR volume measurements where echocardiography generates

smaller volumes when compared to MR [72]. This has to be taken into account when simulation results are interpreted. However, the total mass flow ejected out of the LV during systole depends on the difference between EDV and ESV. Even if the LV volume measured from RT3DE is smaller than the volume obtained from MR at the same HR, the SV might lie in the same range as long as the negative bias in EDV and ESV are approximately the same.

The MV used in this first CFD simulation is the same MV as shown in Fig. A.6(c) and does not have the valve curvature as in the recorded heart. According to our 2D results, the valve curvature affects the velocity pattern in the LVOT. Consequently, the in-vivo flow measurements and the simulation results cannot be expected to be identical either.

Nevertheless, the comparison with the in-vivo flow measurements indicates that our results are within the physiological range.

A.3.6 Limitations

To do a transient simulation of a 3D model with large deformations is not trivial. Several parameters have to be adjusted to avoid negative cells or a bad mesh quality. The solution shown here is not the final optimized solution. Mesh and time convergence tests have to be performed and also an optimization of the remeshing and size function parameters is required to achieve the best possible mesh. The solution of the flow field might be affected of these adjustments.

The 3D model does not include LV torsion about the ventricular central axis. LV torsion may be an important component of normal LV systolic function and should be included to investigate its impact on the flow.

Only the systolic period is simulated. The diastolic period should be included to obtain a more physiological flow field at start-systole.

There was a difference in HR between the MR and RT3DE acquisitions, effort should be put into obtaining the same HR in both acquisitions in order to improve the strength of the validation. Because both acquisitions should be done at the same day to reduce possible sources of error, both the MR and the RT3DE acquisitions should be done over again and hence, a new LV model must be created. One benefit of the developed technique for creating 3D models from RT3DE is the simplicity of incorporating different models of the LV, the LVOT or the MV, with a limited amount of user intervention.

A.4 Concluding remarks

Based on our preliminary results, we suggest that the flow pattern around the Ma-Ao junction and further into the aortic outflow tract is influenced by the degree of anterior leaflet billowing. According to our observations, a normal, slightly billowing anterior leaflet creates a more efficient ejection with lower peak velocities than is the case for a more billowing anterior leaflet. If this is the case, it would be possible that changes in the aortic blood flow pattern might be related to the occurrence of diseases or abnormalities in the mitral valve. However, further investigations are needed to prove this.

A.5 Further work

With the developed framework there is possible to perform many different studies focusing on one parameter at the time.

The initial results from the 2D and 3D study indicates that the degree of anterior leaflet billowing affects the velocity pattern in the aorta during ventricular contraction. This is a new finding which should be investigated further. The 3D MV model will then be modified to different degrees of anterior leaflet billowing. CFD simulations will then be performed for each valve configuration. Echocardiographic recordings of various abnormal BML recorded at Rikshospitalet will be used to determine the degree of bulging. The previously developed software for tracking structures in 2D ultrasound images will be used to obtain the valve profile from the recorded images. Through cooperation with clinical personnel, it might be possible to develop some echocardiographic criteria that would allow differentiating normal from pathological billowing leaflets. The project can also be extended to include prolapse and flail which causes mitral regurgitation. The next project might be to investigate the effects of a billowing posterior leaflet.

Irregularly curved leaflets can occur due to valve pathologies or surgical intervention. E.g. one method used to repair pathologically billowing leaflets, is to attach additional cords to the leaflets' ventricular surfaces to decrease the degree of billowing. This might introduce new irregularities to the valve curvature. A follow-up study might be to examine the pressure and wall shear stress distributions at the ventricular surfaces of such leaflets before and after surgery. Will the new valve profile cause an altered hemodynamic load pattern? And is it likely that the altered hemodynamic load pattern will cause remodeling of the leaflets? Although remodeling may be initiated as adaptations to altered loads, the resulting valve tissues may not be able to provide normal long-term function.

Bibliography

[1] 2009. Echo in a Heartbeat. *customer magazine Medical Solutions*. www.siemens.com/healthcare-magazine.

[2] 2011 (December). *Intro to the Heart*. http://antranik.org/intro-to-the-heart/.

[3] Annerel, Sebastiaan, Degroote, Joris, Claessens, Tom, Dahl, Sigrid Kaarstad, Skallerud, Bjørn, Hellevik, Leif Rune, van Ransbeeck, Peter, Segers, Patrick, Verdonck, Pascal, & Vierendeels, Jan. 2011. A fast Strong Coupling Algorithm for the Partitioned Fluid-Structure Interaction Simulation of BMHVs. *Computer Methods in Biomechanics and Biomedical Engineering*.

[4] Appleton, Christopher P., Hatle, Liv K., & Popp, Richard L. 1988. Relation of transmitral flow velocity patterns to left ventricular diastolic function: New insights from a combined hemodynamic and Doppler echocardiographic study. *Journal of the American College of Cardiology*, **12**(2), 426 – 440.

[5] Arts, Theo, Meerbaum, Samuel, Reneman, Robert, & Corday, Eliot. 1983. Stresses in the closed mitral valve: A model study. *Journal of Biomechanics*, **16**(7), 539 – 547.

[6] Astorino, Matteo, Gerbeau, Jean-Frédéric, Pantz, Olivier, & Traore, Karim-Frédéric. 2009. Fluid-structure interaction and multi-body contact: Application to aortic valves. *Computer Methods in Applied Mechanics and Engineering*, **198**(45-46), 3603 – 3612.

[7] Azizul, Z.H., & Selvanathan, N. 2007. 2D Arbitrary Lagrangian-Eulerian (ALE) Model of Blood Flow in the Left Ventricle (LV) of the Heart. *Pages 554–557 of: IFMBE Proceedings 15*. Springer-Verlag Berlin Heidelberg.

[8] Baccani, B., Domenichini, F., Pedrizzetti, G., & Tonti, G. 2002a. Fluid dynamics of the left ventricular filling in dilated cardiomyopathy. *Journal of Biomechanics*, **35**, 665–671.

[9] Baccani, B., Domenichini, F., & Pedrizzetti, G. 2002b. Vortex dynamics in a left ventricle during filling. *European Journal of Mechanics B/Fluids*, **21**, 527–543.

[10] Balocco, Simone, Basse, Olivier, Azencot, Jacques, Tortoli, Piero, & Cachard, Christian. 2008. 3D dynamic model of healthy and pathologic arteries for ultrasound technique evaluation. *Medical Physics*, **35**(12), 5440–50.

[11] Bang, Jin Seok, Yoo, Song Min, & Kim, Chang Nyung. 2006. Characteristics of Pulsatile Blood Flow Through the Curved Bileaflet Mechanical Heart Valve Installed in Two Different Types of Blood Vessels: Velocity and Pressure of Blood Flow. *ASAIO Journal*, **52**(3), 234–242.

[12] Barlow, J. B. 1987. *Perspectives on the mitral valve*. F. A. Davis Company.

[13] Bellhouse, B.J. 1972. Fluid mechanics of a model mitral valve and left ventricle. *Cardiovascular Research 1972*, **6**, 199–210.

[14] Blume, Gustavo G., Mcleod, Christopher J., Barnes, Marion E., Seward, James B., Pellikka, Patricia A., Bastiansen, Paul M., & Tsang, Teresa S.M. 2011. Left atrial function: physiology, assessment, and clinical implications. *European Journal of Echocardiography*, **12**(6), 421–430.

[15] Borazjani, Iman, Ge, Liang, & Sotiropoulos, Fotis. 2008. Curvilinear immersed boundary method for simulating fluid structure interaction with complex 3D rigid bodies. *Journal of Computational Physics*, **227**(16), 7587–7620.

[16] Bot, H., Verburg, J., Delemarre, B.J., & Strackee, J. 1990. Determinants of the occurrence of vortex rings in the left ventricle during diastole. *Journal of biomechanics*, **23**(6), 607–615.

[17] Calkins, Hugh, Ho, Siew Y., Cabrera, José Angel, Bella, Paolo Della, Farré, Jeronimo, Kautzner, Josep, & Tchou, Patrick. 2008. *Anatomy of the Left Atrium and Pulmonary Veins*. Oxford, UK: Blackwell Publishing Ltd. Chap. 1.

[18] Carmody, C. J., Burriesci, G., Howard, I.C., & Patterson, E.A. 2006. An approach to the simulation of fluid-structure interaction in the aortic valve. *Journal of Biomechanics*, **39**(1), 158–169.

[19] Carpentier, A., Adams, D.H., & Filsoufi, F. 2010. *Carpentier's Reconstructive Valve Surgery: From Valve Analysis to Valve Reconstruction*. Saunders / Elsevier.

[20] Cheng, Rui, Lai, Yong G., & Chandran, Krishnan B. 2004. Three-Dimensional Fluid-Structure Interaction Simulation of Bileaflet Mechanical Heart Valve Flow Dynamics. *Annals of Biomedical Engineering*, **32**(11), 1471–1483.

[21] Cheng, Yongguang, Oertel, Herbert, & Schenkel, Torsten. 2005. Fluid-Structure Coupled CFD Simulation of the Left Ventricular Flow During Filling Phase. *Annals of Biomedical Engineering*, **33**(5), 567–576.

[22] Choi, Choeng Ryul, & Kim, Chang Nyung. 2003. Pulsatile Blood Flows Through a Bileaflet Mechanical Heart Valve with Different Approach Methods of Numerical Analysis; Pulsatile Flows with Fixed Leaflets and Interacted with Moving Leaflets. *KSME International Journal*, **17**(7), 1073–1082.

[23] Choi, Choeng Ryul, & Kim, Chang Nyung. 2009. Numerical Analysis on the Hemodynamics and Leaflet Dynamics in a Bileaflet Mechanical Heart Valve Using a Fluid-Structure Interaction Method. *American Society of Artificial Internal Organs*, **55**(20-21 October), 428–437. DOI: 10.1097/MAT.0b013e3181b58f98.

[24] Christiansen, Jonathan P., Karamitsos, Theodoros D., & Myerson, Saul G. 2011. Assessment of Valvular Heart Disease by Cardiovascular Magnetic Resonance Imaging: A Review. *Heart, Lung and Circulation*, **20**(2), 73 – 82.

[25] Crosby, Jonas. 2009. *Ultrasound-based quantification of myocardial deformation and rotation*. Ph.D. thesis, Norwegian University of Science and Technology.

[26] Dahl, S. K., Fagerholt, E., Kiss, G., Prot, V., Amundsen, B., Hellevik, L. R., & Skallerud, B. 2011. 3D moving boundary conditions for heart CFD simulations - from echocardiographic recordings to discretized surfaces. *Pages 33–46 of: MekIT'11: Sixth National Conference on Computational Mechanics*. Tapir Akademisk Forlag.

[27] Dahl, Sigrid Kaarstad, Vierendeels, Jan, Degroote, Joris, Annerel, Sebastiaan, Hellevik, Leif Rune, & Skallerud, Bjørn. 2012. FSI simulation of asymmetric mitral valve dynamics during diastolic filling. *Computer Methods in Biomechanics and Biomedical Engineering*, **15**(2), 121–130.

[28] de Hart, J., Peters, G. W. M., Schreurs, P. J. G., & Baaijens, F. P. T. 2003. A three-dimensional computational analysis of fluid-structure interaction in the aortic valve. *Journal of Biomechanics*, **36**(1), 103–112.

[29] Degroote, Joris. 2010. *Development of Algorithms for the Partitioned Simulation of Strongly Coupled Fluid-Structure Interaction Problems*. Ph.D. thesis, Ghent University.

[30] Degroote, Joris, Bruggeman, Peter, Haelterman, Robby, & Vierendeels, Jan. 2008. Stability of a coupling technique for partitioned solvers in FSI applications. *Computers & Structures*, **86**(23-24), 2224 – 2234.

[31] Doenst, Torsten, Spiegel, Kathrin, Reik, Michael, Markl, Michael, Hennig, Jürgen, Nitzsche, Stefan, Beyersdorf, Friedhelm, & Oertel, Herbert. 2009. Fluid-Dynamic Modeling of the Human Left Ventricle: Methodology and Application to Surgical Ventricular Reconstruction. *Ann Thorac Surg*, **87**, 1187–1195.

[32] Domenichini, F., & Pedrizzetti, G. 2011. Intraventricular vortex flow changes in the infarcted left ventricle: numerical results in an idealised 3D shape. *Computer Methods in Biomechanics and Biomedical Engineering*, **14**(1), 91–101.

[33] Domenichini, F., Querzoli, G., Cenedese, A., & Pedrizzetti, G. 2007. Combined experimental and numerical analysis of the flow structure into the left ventricle. *Journal of Biomechanics*, **40**, 1988–1994.

[34] Donea, J., Giuliani, S., & Halleux, J.P. 1982. An arbitrary lagrangian-eulerian finite element method for transient dynamic fluid-structure interactions. *Computer Methods in Applied Mechanics and Engineering*, **33**(1-3), 689 – 723.

[35] Dumont, K., Stijnen, J.M.A, Vierendeels, J., van de Vosse, F.N., & Verdonck, P.R. 2004. Validation of a Fluid-Structure Interaction Model of a Heart Valve using the Dynamic Mesh Method in Fluent. *Computer methods in Biomechanics and Biomedical Engineering*, **7**(3), 139–146.

[36] Dumont, K., Vierendeels, J., Segers, P., Van Nooten, G., & Verdonck, P. R. 2005. Predicting ATS Open Pivot (TM) heart valve performance with computational fluid dynamics. *Journal of heart valve disease*, **14**(3), 393–399.

[37] Dumont, Kris, Vierendeels, Jan, Kaminsky, Rado, van Nooten, Guido, Verdonck, Pascal, & Bluestein, Danny. 2007. Comparison of the Hemodynamic and Thrombogenic Performance of Two Bileaflet Mechanical Heart Valves Using a CFD/FSI Model. *Journal of Biomechanical Engineering*, **129**(August), 558–565.

[38] Einstein, Daniel R., Kunzelman, Karyn S., Reinhall, Per G., & Nicosia, Mark A. 2005. Nonlinear fluid-coupled computational model of the mitral valve. *Journal of Heart Valve Disease*, **14**, 376–385.

[39] Espino, Daniel M., Watkins, Michael A., Shepherd, Duncan E.T, Hukins, David W.L., & Buchan, Keith G. 2006. Simulation of Blood Flow through the Mitral Valve of the Heart: A Fluid Structure Interaction Model. *In: Proceedings of the COMSOL Users Conference*.

[40] Forsythe, Neil, & Mueller, Jens-Dominik. 2008. Validation of a fluid-structure interaction model for a bileaflet mechanical heart valve. *International Journal of Computational Fluid Dynamics*, **22**(9), 541–553.

[41] Fung, Y. C. 1993. *Biomechanics: mechanical properties of living tissues*. Second edn. Springer.

[42] Fyrenius, A., Wigström, L., Ebbers, T., Karlsson, M., Engvall, J., & Bolger, A.F. 2001. Three dimensional flow in the human left atrium. *British medical journal*, **86**(4), 448–455.

[43] Glowinski, R., Pan, T.-W., & Periaux, J. 1994. A fictitious domain method for Dirichlet problem and applications. *Computer Methods in Applied Mechanics and Engineering*, **111**, 283–303.

[44] Grande-Allen, K.J. 2004 (sept.). Fibrotic vs. Myxomatous Remodeling of Mitral Valves. *Pages 3737 – 3740 of: Engineering in Medicine and Biology Society, 2004. IEMBS '04. 26th Annual International Conference of the IEEE*, vol. 2.

[45] Guivier, Carine, Deplano, Valerie, & Pibarot, Philippe. 2007. New insight into the assessment of the prosthetic valve performance in the presence of subaortic stenosis theough a fluid-structure interaction model. *Journal of Biomechanics*, **40**, 2283–2290.

[46] Hansegård, Jøger, Urheim, Stig, Lunde, Ketil, Malm, Siri, & Rabben, Stein Inge. 2009. Semi-automated quantification of left ventricular volumes and ejection fraction by real-time three-dimensional echocardiography. *Cardiovascular Ultrasound*, **7**(18).

[47] Hatze, Herbert. 1974. The meaning of the term biomechanics. *Journal of Biomechanics*, **7**, 189–190.

[48] Heiberg, Einar, Sjogren, Jane, Ugander, Martin, Carlsson, Marcus, Engblom, Henrik, & Arheden, Hakan. 2010. Design and validation of Segment - freely available software for cardiovascular image analysis. *BMC Medical Imaging*, **10**(1), 1.

[49] Hellevik, LR, Astorino, M, Moireau, P, Prot, V, Skallerud, B, Gerbeau, JF, & D, Chapelle. 2010. FSI Simulation of the Mitral Valve with Contact and Active Anisotropic Material Models. *Page 266 of: 6th World Congress of Biomechanics*.

[50] Hu, Yingying, Shi, Liang, Parameswaran, Siva, Smirnov, Sergey, & He, Zhaoming. 2010. Left Ventricular Vortex Under Mitral Valve Edge-to-Edge Repair. *Cardiovascular Engineering and Technology*, **1**(4), 235–243.

[51] Jenkins, C., Chan, J., Hanekom, L., & T.H., Marwick. 2006. Accuracy and feasibility of online 3-dimensional echocardiography for measurement of left ventricular parameters. *J Am Soc Echocardiogr*, **19**(9), 1119–28.

[52] Jimenez, J.H., Soerensen, D.D., He, Z., He, S., & Yoganathan, A.P. 2003. Effects of a saddle shaped annulus on mitral valve function and chordal force distribution: an in vitro study. *Ann Biomed Eng.*, **31**(10), 1171–1181.

[53] Kaplan, Starr R., Bashein, Gerard, Sheehan, Florence H., Legget, Malcolm E., Munt, Brad, Li, Xiang-Ning, Sivarajan, Murali, Bolson, Edward L., Zeppa, Merrilinn, Archa, M., & Martin, Roy W. 2000. Three-dimensional echocardiographic assessment of annular shape changes in the normal and regurgitant mitral valve. *American Heart Journal*, **139**(3), 378 – 387.

[54] Kato, Ritsushi, Lickfett, Lars, Meininger, Glenn, Dickfeld, Timm, Wu, Richard, Juang, George, Angkeow, Piamsook, LaCorte, Jennifer, Bluemke, David, Berger, Ronald, Halperin, Henry R., & Calkins, Hugh. 2003. Pulmonary Vein Anatomy in Patients Undergoing Catheter Ablation of Atrial Fibrillation. *Circulation*, **107**(15), 2004–2010.

[55] Kilner, Philip J., Yang, Guang-Zhong, Wilkes, A. John, Mohiaddin, Raad H., Firmin, David N., & Yacoub, Magdi H. 2000. Asymmetric redirection of flow through the heart. *Nature*, **404**(13 april), 759–764.

[56] Kilner, Philip J., Gatehouse, Peter D., & Firmin, David N. 2007. Flow Measurement by Magnetic Resonance: A Unique Asset Worth Optimising. *Journal of Cardiovascular Magnetic Resonance*, **9**(4), 723–728.

[57] Kim, W.Y, Bisgaard, T., Nielson, S.L., Poulsen, J.K., Pedersen, E.M., Hasenkam, J.M., & Yoganathan, A.P. 1994. Two-dimensional mitral flow velocity profiles in pig models using epicardial Doppler echocardiography. *Journal of the American College of Cardiology*, **24**(2), 532–545.

[58] Kitajima, Hiroumi, & Yoganathan, Ajit P. 2005. *Blood flow - The Basics of the Discipline*. Blackwell Publishing. Chap. 3, pages 38–54.

[59] Klabunde, Richard E. 2005. *Cardiovascular Physiology Concepts*. Lippincott Williams & Wilkins.

[60] Krittian, Sebastian, Schenkel, Torsten, Janoske, Uwe, & Oertel, Herbert. 2010. Partitioned Fluid-Solid Coupling for Cardiovascular Blood Flow: Validation Study of Pressure-Driven Fluid-Domain Deformation. *Annals of Biomedical Engineering,*, **38**(8), 2676–2689.

[61] Ku, David N. 1997. Blood flow in arteries. *Annual Review of Fluid Mechanics*, **29**, 399–434.

[62] Lam, J. H. C, Ranganathan, N., Wigle, E.D., & Silver, M.D. 1970. Morphology of the human mitral valve: I. Chordae tendineae: A new classification. *Circulation*, **41**, 449–458.

[63] Long, Q., Merrifield, R., Yang, G.Z, Kilner, P. J., Firmin, D. N., , & Xu, X. Y. 2003. The Influence of Inflow Boundary Conditions on Intra Left Ventricle Flow Predictions. *Journal of Biomechanical Engineering, ASME*, **125**, 922–927.

[64] Long, Q., Merrifield, R., Xu, X. Y., Kilner, P. J., Firmin, D. N., & Yang, G.Z. 2007. Subject-specific computational simulation of left ventricular flow based on magnetic resonance imaging. *Journal of Engineering in Medicine*, **222**, 475–485.

[65] Loon, Raoul van. 2005. *A 3D method for modelling the fluid-structure interaction of heart valves*. Ph.D. thesis, Eindhoven University of Technology.

[66] Lotz, Joachim, Meier, Christian, Leppert, Andreas, & Galanski, Michael. 2002. Cardiovascular Flow Measurement with Phase-Contrast MR Imaging: Basic Facts and Implementation. *RadioGraphics*, **22**(3), 651–671.

[67] Mansour, M., Holmvang, G., Sosnovik, D., Migrino, R., Abbara, S., Ruskin, J., & Keane, D. 2004. Assessment of Pulmonary Vein Anatomic Variability by Magnetic Resonance Imaging: Implications for Catheter Ablation Techniques for Atrial Fibrillation. *Journal of Cardiovascular Electrophysiology*, **15**(4), 387–393.

[68] McQueen, D. M., & Peskin, C. S. 2000. A three-dimensional computer model of the human heart for studying cardiac fluid dynamics. *ACM SIGGRAPH Computer Graphics*, **34**(Feb), 56–60.

[69] Merrifield, R., Long, Q., Xu, X. Y., Kilner, P. J., Firmin, D. N., & Yang, G. Z. 2004. *Combined CFD/MRI Anaylysis of left ventricular flow*. Berlin: Springer-Verlag.

[70] Mihalef, Viorel, Metaxas, Dimitris, Sussman, Mark, Hurmusiadis, Vassilios, & Axel, Leon. 2009. Atrioventricular Blood Flow Simulation Based on Patient-Specific Data. *Pages 386–395 of: Functional Imaging and modeling of the heart*. Springer-Verlag Berlin Heidelberg.

[71] Mihalef, Viorel, Ionasec, Razvan, Wang, Yang, Zheng, Yefeng, Georgescu, Bogdan, & Comaniciu, Dorin. 2010 (april). Patient-specific modeling of left heart anatomy, dynamics and hemodynamics from high resolution 4D CT. *Pages 504 –507 of: Biomedical Imaging: From Nano to Macro, 2010 IEEE International Symposium on*.

[72] Mor-Avi, Victor, Jenkins, Carly, Kuhl, Harald P, Nesser, Hans-Joachim, Marwick, Thomas, Franke, Andreas, Ebner, Christian, Freed, Benjamin H., Steringer-Mascherbauer, Regina, Pollard, Heidi, Weinert, Lynn, Niel, Johannes, Sugeng, Lissa, & Lang, Robert M. 2008. Real-Time 3-Dimensional Echocardiographic Quantification of Left Ventricular Volumes. *JACC cardiovascular Imaging*, **1**(4), 413–423.

[73] Morsi, Yos S., Yang, William W., Wong, Cynthia S., & Das, Subrat. 2007. Transient fluid-structure coupling for simulation of a trileaflet heart valve using weak coupling. *Journal of artificial organs*, **10**(2), 96–103.

[74] Nakamura, Masanori, Wada, Shiego, & Yamaguchi, Takami. 2006. Influence of the opening mode of the mitral valve orifice on intraventricular hemodynamics. *Annals of Biomedical Engineering*, **34**(6), 927–935.

[75] Nobili, M., Passoni, A., & Redaelli, A. 2007. Two fluid-structure approaches for 3D simulation of St. Jude Medical bileaflet valve opening. *Journal of Applied Biomaterials & Biomechanics*, **5**(1), 49–59.

[76] Nobili, Matteo, Morbiducci, Umberto, Ponzini, Raffaele, Del Gaudio, Costantino, Balducci, Antonio, Grigioni, Mauro, Montevecchi, Franco Maria, & Redaelli, Alberto. 2008. Numerical simulation of the dynamics of a bileaflet prosthetic heart valve using fluid-structure interaction approach. *Journal of Biomechanics*, **41**, 2539–2550.

[77] Pedrizzetti, G., & Domenichini, F. 2006. Flow-driven opening of a valvular leaflet. *Journal of Fluid Mechanics*, **569**, 321–330.

[78] Peskin, C. S. 1972. Flow Patterns Around Heart Valves: A Numerical Method. *Journal of computational physics*, **10**(Feb), 252–271.

[79] Peskin, C. S., & McQueen, D. M. 1989. A three-dimensional computational method for blood flow in the heart. 1. Immersed elastic fibers in a viscous incompressible fluid. *Journal of Computational Physics*, **81**(April), 372–405.

[80] Peskin, C. S., & McQueen, D. M. 1996. Fluid dynamics of the heart and its valves. *Chap. 14, pages 309–337 of:* Othmer, H.G., Adler, F.R., Lewis, M.A., & J.C, Dallon (eds), *Case Studies in Mathematical Modeling: Ecology, Physiology, and Cell Biology*. Prentice-Hall.

[81] Pierrakos, Olga, & Vlachos, Pavlos P. 2006. The effect of vortex formation on left ventricular filling and mitral valve efficiency. *Journal of Biomechanical Engineering*, **128**(August), 527–539.

[82] Pinnock, Colin A., Lin, Ted, & Smith, Tim. 2002. *Fundamentals of anaesthesia*. Cambridge University Press.

[83] Popel, Aleksander S., & Johnson, Paul C. 2005. Microcirculation and hemorheology. *Annual Review of Fluid Mechanics*, **37**(1), 43–69.

[84] Prot, V, & Skallerud, B. 2009. Nonlinear solid finite element analysis of mitral valves with heterogeneous leaflet layers. *Computational Mechanics*, **42**(3), 353–368.

[85] Prot, V, Skallerud, B, & Holzapfel, G. 2007. Transversely isotropic membrane shells with application to mitral valve mechanics. Constitutive modelling and finite element implementation. *Int J Numerical Methods in Engineering*, **71**, 987–1008.

[86] Rein, Kjell Arne. 2011. Personal communication.

[87] Reul, H., Talkuder, N., & Muller, E. W. 1981. Fluid mechanics of the natural mitral valve. *Journal of Biomechanics*, **14**(5), 361–372.

[88] Rodevand, Olav, Bjornerheim, Reidar, Edvardsen, Thor, Smiseth, Otto A., & Ihlen, Halfdan. 1999. Diastolic Flow Pattern in the Normal Left Ventricle. *Journal of the American Society of Echocardiography*, **12**(6), 500–507.

[89] Rollick, Charles, Pittman, Marjorie, Filly, Kitty, Fitzgerald, Peter J., & Popp, Richard L. 1982. Mitral and aortic valve orifice area in normal subjects and in patients with congestive cardiomyopathy: Determination by two dimensional echocardiography. *The American Journal of Cardiology*, **49**(5), 1191 – 1196.

[90] Rooke, Thom W., & Sparks Jr., Harvey V. 2003. *The Cardiac Pump*. Lippincott Williams & Wilkins. Chap. 14, pages 237–251.

[91] Rosenfeld, M., Avrahami, I., & Einav, S. 1999. The time-dependent flow across a model of a mitral tilting disk valve and the left ventricle. *ASME-PUBLICATIONS-BED*, **42**, 563–564.

[92] Rssel, Iris K., Gtte, Marco J.W., Bronzwaer, Jean G., Knaapen, Paul, Paulus, Walter J., & van Rossum, Albert C. 2009. Left Ventricular Torsion: An Expanding Role in the Analysis of Myocardial Dysfunction. *JACC cardiovascular Imaging*, **2**(5), 648–655.

[93] Saber, Nikoo R., Gosman, A.D, Wood, Nigel B., Kilner, Philip J., Charrier, Clare L., & Firmin, David N. 2001. Computational Flow Modeling of the Left Ventricle Based on In Vivo MRI Data: Initial Experience. *Annals of Biomedical Engineering,*, **29**, 275–283.

[94] Saber, Nikoo R., Wood, Nigel B., Gosman, A.D, Merrifield, Robert D., Yang, Guang-Zhong, Charrier, Clare L., Gatehouse, Peter D., & Firmin, David N. 2003. Progress Towards Patient-Specific Computational Flow Modeling of the Left Heart via Combination of Magnetic Resonance Imaging with Computational Fluid Dynamics. *Annals of Biomedical Engineering,*, **31**, 42–52.

[95] Salgo, Ivan S., Gorman, Joseph H., Gorman, Robert C., Jackson, Benjamin M., Bowen, Frank W., Plappert, Theodore, St John Sutton, Martin G., & Edmunds, L. Henry. 2002. Effect of Annular Shape on Leaflet Curvature in Reducing Mitral Leaflet Stress. *Circulation*, **106**(6), 711–717.

[96] Samstad, Stein O, Torp, Hans G, Linker, David T, Rossvoll, Ole, Skjaerpe, Terje, Johansen, Erling, Kristoffersen, Kjell, Angelsen, Bjoern A J, & Hatle, Liv. 1989. Cross sectional early mitral flow velocity profiles from colour Doppler. *Br Heart J*, **62**, 177–184.

[97] Sanfilippo, Anthony J., Harrigan, Pamela, Popovic, Aleksandar D., Weyman, Arthur E., & Levine, Robert A. 1992. Papillary muscle traction in mitral valve prolapse: Quantitation by two-dimensional echocardiography. *Journal of the American College of Cardiology*, **19**(3), 564 – 571.

[98] Schenkel, Torsten, Malve, Mauro, Reik, Michael, Markl, Michael, Jung, Bernd, & Oertel, Herbert. 2009. MRI-based CFD Analysis of Flow in a Human Left Ventricle: Methodology and Application to a healthy Heart. *Annals of Biomedical Engineering*, **37**(3), 503–515.

[99] Schmidt, Boris, Ernst, Sabine, Ouyang, Feifan, Chun, K.R. Julian, Broemel, Thomas, Bansch, Dietmar, Kuck, Karl-Heinz, & Antz, Matthias. 2006. External and Endoluminal Analysis of Left Atrial Anatomy and the Pulmonary Veins in Three-Dimensional Reconstructions of Magnetic Resonance Angiography: The Full Insight from Inside. *Journal of Cardiovascular Electrophysiology*, **17**(9), 957–964.

[100] Shibata, M., Yambe, T., Kanke, Y., & Hayase, T. 2009. Atrial Vortex Measurement by Magnetic Resonance Imaging. *Pages 2254–2257 of:* Lim, Chwee Teck, Goh, James C. H., & Magjarevic, Ratko (eds), *13th International Conference on Biomedical Engineering*. IFMBE Proceedings, vol. 23. Springer Berlin Heidelberg.

[101] Shortland, A.P, Black, R.A, Jarvis, J.C., Henry, F.S, Iudicello, F., Collins, M.W., & Salmonst, S. 1996. Formation and travel of vortices in model ventricles: Application to the design of skeletal muscle ventricles. *Journal of Biomechanics*, **29**(4), 503–511.

[102] Shung, K. P., Sigelmann, R. A., & Schmer, G. 1975. Ultrasonic Measurement of Blood Coagulation Time. *IEEE Transactions on Biomedical Engineering*, **BME-22**(4), 334 –337.

[103] Skallerud, B, Prot, V, & Nordrum, I.S. 2011. Modeling active muscle contraction in mitral valve leaflets during systole: a first approach. *Biomechanics and modeling in mechanobiology*, **10**, 11–26.

[104] Spiegel, K., Schiller, W., Schmid, T., Welz, A., Liepsch, D., & Oertel, H. 2007 (20-22 August). Numerical simulation of the left ventricle and atrium as reference for pathological hearts. *Pages 78–83 of: Proceedings of the fifth IASTED International Conference on biomechanics*.

[105] Stijnen, J. M. A., de Hart, J., Bovendeerd, P. H. M., & van de Vosse, F. N. 2004. Evaluation of a fictitious domain method for predicting dynamic response of mechanical heart valves. *Journal of Fluids and Structures*, **19**, 835–850.

[106] Stijnen, J. M. A, Bogaerds, A. C. B, de Hart, J, Bovendeerd, P. H. M., de Mol, B. A. J. M., & van de Vosse, F. N. 2009. Computational analysis of ventricular valve-valve interaction: Influence of flow conditions. *International journal of Computational Fluid Dynamics*, **23**(8), 609–622.

[107] Swillens, Abigail, Løvstakken, Lasse, Kips, Jan, Torp, Hans, & Segers, Patrick. 2009. Ultrasound simulation of complex flow velocity fields based on computational fluid dynamics. *IEEE Trans Ultrason Ferroelectr Freq Control*, **56**(3), 546–56.

[108] Swillens, Abigail, Degroote, Joris, Vierendeels, Jan, Løvstakken, Lasse, & Segers, Patrick. 2010. A simulation environment for validating ultrasonic blood flow and vessel wall imaging based on fluid-structure interaction simulations: ultrasonic assessment of arterial distension and wall shear rate. *Medical Physics*, **37**(8), 4318–30.

[109] Tanne, D., Bertrand, E., Pibarot, P., & Rieu, R. 2008. Asymmetric flows in an anatomical-shaped left atrium by 2C-3D+T PIV measurements. *Computer Methods in Biomechanics and Biomedical Engineering*, 209–211.

[110] Tanne, David, Bertrand, Eric, Kadem, Lyes, Pibarot, Philippe, & Rieu, Régis. 2010. Assessment of left heart and pulmonary circulation flow dynamics by a new pulsed mock circulatory system. *Experiments in Fluids*, **48**, 837–850.

[111] Theakston, F. 2008. *World Health Statistics*. WHO Press.

[112] Tsakiris, A. G., Padiyar, R., Gordon, D. A., & Irving, L. 1977. Left atrial size and geometry in the intact dog. *Am J Physiol*, **232**, H167–H172.

[113] van Loon, Raoul, Anderson, Patrick D., Baaijens, Frank P. T., & van de Vosse, Frans N. 2005. A three-dimensional fluid-structure interaction method for heart valve modelling. *C.R. Mecanique*, **333**, 856–866.

[114] van Loon, Raoul, Anderson, Patrick D., & van de Vosse, Frans N. 2006. A fluid-structure interaction method with solid-rigid contact for heart valve dynamics. *Journal of Computational Physics*, **217**, 806–823.

[115] Vierendeels, Jan, Riemslagh, K., Dick, Erik, & Verdonck, Pascal. 2000. Computer Simulation of Intraventricular Flow and Pressure Gradients During Diastole. *Journal of Biomechanical Engineering*, **122**(December), 667–674.

[116] Vierendeels, Jan, Dumont, Kris, Dick, Erik, & Verdonck, Pascal. 2005. Analysis and Stabilization of Fluid-Structure Interaction Algorithm for Rigid-Body Motion. *AIAA journal*, **43**(12), 2549–2557.

[117] Watton, P. N., Luo, X. Y., Yin, M., Bernacca, G. M., & Wheatley, D. J. 2008. Effect of ventricle motion on the dynamic behaviour of chorded mitral valves. *Journal of Fluids and Structures*, **24**, 58–74.

[118] West, John B. 1990. *Best and Taylor's Physiological Basis of Medical Practice*. twelfth edn. Baltimore: Williams & Wilkins.

[119] Wittkampf, Fred H.M., van Oosterhout, Matthijs F., Loh, Peter, Derksen, Richard, Vonken, Evert-jan, Slootweg, Piet J., & Ho, Siew Yen. 2005. Where to draw the mitral isthmus line in catheter ablation of atrial fibrillation: histological analysis. *European Heart Journal*, **26**(7), 689–695.

[120] Zhang, Lucy T., & Gay, Mickal. 2008. Characterizing left atrial appendage functions in sinus rhythm and atrial fibrillation using computational models. *Journal of Biomechanics*, **41**(11), 2515 – 2523.